AN EXPERIMENTAL INVESTIGATION OF HEATING MECHANISMS, MODE TRANSITION AND INSTABILITIES IN A RADIO FREQUENCY INDUCTIVELY COUPLED PLASMA

A thesis for the degree of

PHILOSOPHIAE DOCTOR

Presented to

DUBLIN CITY UNIVERSITY

By

BRENDAN J. CROWLEY BSc. H.Dip.Ed

School of Physical Sciences

DUBLIN CITY UNIVERSITY

Research Supervisor Dr David Vender

External Examiner Dr Nicholas St.J. Braithwaite

Internal Examiner Prof Eugene T Kennedy

June 2000

Declaration

I hereby certify that this material which I now submit for assessment on the programme of study leading to the award of Philosophiae Doctor is entirely my own work and has not been taken from the works of others save and to the extent that such work has been cited and acknowledged within the text of this work

Brendan Crowley 6^{th} June 2000

Acknowledgements

The work presented in this thesis was carried out at the Plasma Research Laboratory (PRL) in the School of Physical Science at DCU I am grateful everyone associated with PRL and the Physics department who facilitated and assisted my work over the past four years I make special mention of some of the people to whom I owe particularly gratitude First of all my thanks goes to my research supervisor Dr David Vender for his support and guidance over the past four years, to Dr Gilles Cunge with whom I co-worked on much of this project and to Sam Fahy for her continuous help to the very end of this endeavor I would also like to thank the other academic staff at PRL Dr Mike Hopkins and Dr Miles Turner for their help throughout the project Thanks also to the technical and support staff at the school of physics, in particular to Alan Hughes, Des Lavelle, Declan Ledwith, and Al Devine whose technical skills I have relied on through out my time at DCU I thank my examiners Dr Nicholas Braithwaite and Prof Eugene Kennedy for their useful comments and suggestions regarding the thesis

The four years that I have spent as a student at DCU has for me been a good and happy experience This is in no small measure due to the friendship and support that I received from my fellow students at PRL, Deirdre, George, Neil, Deborah and Roberto as well as all the other post-grads and staff at DCU

I thank my friends and family for their support down through the years Particularly my parents, Mary and the late Edmond Crowley who made many sacrifices to educate their family

Finally I would like to pay tribute to my wife Claire, whose constant encouragement, support and faith in me, made this achievement possible

To

Claire and Matthew

Abstract

Radio frequency (RF) inductively coupled plasma (ICP) have been known and studied for over a century In recent years, due to the vast array of potential applications of plasma technology, research in the area has become more prolific This thesis presents the results of a detailed experimental investigation that uses electrical diagnostics (Langmuir and magnetic field (B) probes etc) on a particular type of inductively coupled plasma source (re-entrant cavity) The investigation focuses on three aspects of the ICP Firstly the heating mechanisms that sustain the plasma are characterized It is found that the RF electric field and current density distributions determined from B probe measurements indicate a strong anomalous skin effect This is exemplified by non-monotonic decay of the electromagnetic fields, phase reversal and bifurcation, as well as negative power absorption regions These features are interpreted in terms of spatial dispersion of the conductivity due to the electron thermal motion at low pressure Secondly the E-H mode transition is comprehensively investigated using various steady state and time resolved diagnostics, the results show that hysteresis with respect to the transition current is accounted for by variation in the plasma production efficiency due to changes in the electron energy distribution function (EEDF) and the presence of metastable atoms Finally, a specific type of instability observed in low pressure ICPs is investigated experimentally and the results are found to agree on many points with a proposed model describing the instability

Contents

List of Figures

Chapter 1

Introduction to RF plasmas

Inductively coupled discharges have been known and studied for over a century [1], however in the last two decades there has been much renewed research interest in their operation in the low pressure, radio frequency (13 56 MHz) regime This research has been largely driven by the requirements of the microprocessor fabrication industry [2, 3] Microprocessor manufacture is typically carried out by successive processes of deposition and etching of layers of material on a silicon wafer, many of these process steps are carried out in a plasma environment The etching process, used to etch small features on the surface of the wafer generally requires a beam of ions impinging normally on the wafer surface The industry requirement for smaller feature sizes and faster microchips at cheaper prices means these ion beams have to etch ever more precisely over larger wafer areas and all at higher speeds These requirements are not always met by the traditional capacitivley coupled plasma etching machines Sophisticated antenna and chamber designs [4] are employed In order to meet the industry's need for

large area uniform plasmas, but in order to etch more features per unit area, such as sub-micron trenches, the etching process must be more anisotropic than heretofore Deep features with low aspect ratios and negligible undercutting such as the ones shown in figure 1 1(a) and figure 1 1(b) are made by bombarding the exposed section of the material with an ion flux which is highly anisotropic, such a flux is only possible if the ions are accelerated through the plasma sheath without undergoing scattering collisions with neutrals along the way This means that the operating pressure in the chamber must be low ($\approx 10\,\mathrm{mTorr}$)

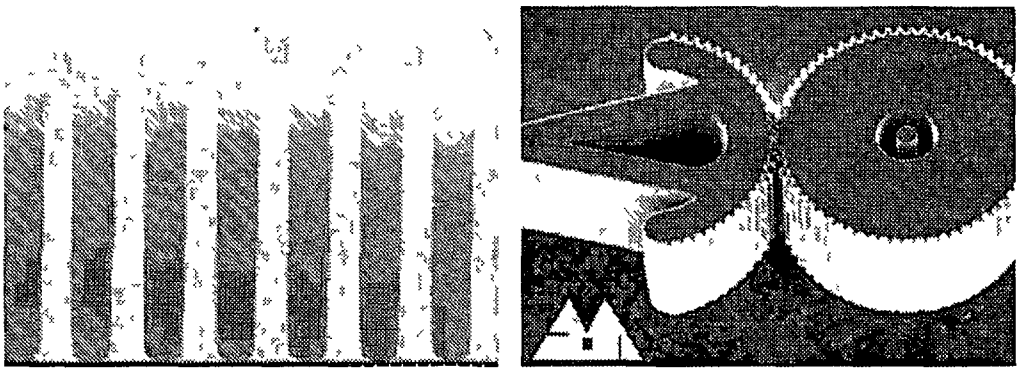

Figure 1 1 *Micrometer sized features resulting from plasma processes (a) high aspect ratio anisotropic etch (b) Example of micro-machine*

Radio frequency ICPs are well suited to plasma processing applications for a number of reasons [5],

1 There are *no* metal electrodes in the discharge, this reduces the contamination of reactive gases which can occur as a result of sputtering of material from metal electrodes

2 Electrons are heated preferentially by radio frequency waves This allows the establishment of a non-equilibrium plasma with a high electron temperature and low ion and neutral gas temperature

3 Non-capacitive coupling leads to low dc plasma voltages across all plasma sheaths hence the ion acceleration energy to any workpiece is low, furthermore a workpiece can be independently biased by a separate RF power source, which allows for independent control of the energy of the ions bombarding the workpiece

4 Radio frequency ICPs are capable of producing high density plasmas ($10^{11} - 10^{12}$ cm^{-3}) at low pressures (< 10 mTorr) and moderate input powers ($50 - 1000$ W)

1.1 ICP Source Designs

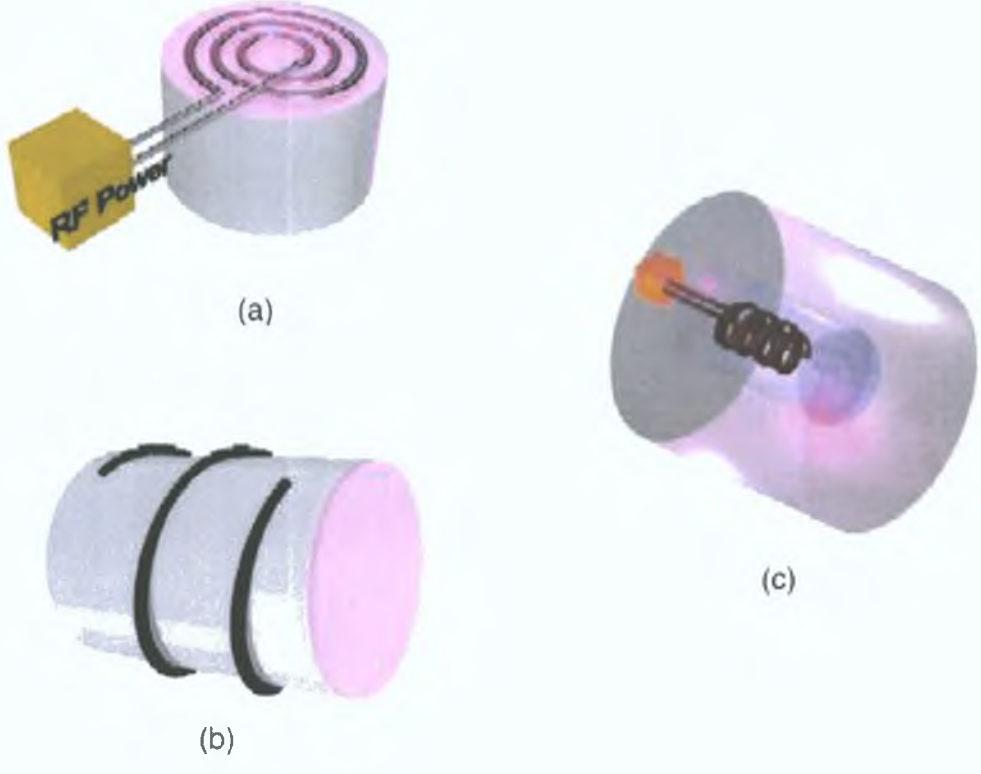

Figure 1.2: *Schematic diagrams of different types of ICP sources. (a) Large area ICP reactor. (b) External helical coil ICP reactor. (c) Re-entrant cavity ICP reactor. Typical diameters for these sources are 20-40 cm*

Experimental and commercial ICP sources have been studied and tested in a variety of geometric configurations. Processing chambers of the type shown in figure 1.2 (a), which have been the subject of many experimental and modelling investigations [6, 3, 7, 8, 9, 10] tend to have the widest use in industry. Different aspect ratios and antenna shapes are employed in order to optimise plasma uni-

formity over a large area [11] The RF antenna is a generally a planar spiral coil although it is often wound non-uniformly in order to enhance the radial uniformity of the plasma [12] Planar coil ICPs allow independently biased substrates to be positioned close to the dielectric window for processing Undesirable capacitive coupling in the discharge can be almost eliminated by placing a Faraday shield between the coil and the window An alternative design shown in figure 1 2 (b) utilises a helical coil which is wound around the plasma chamber

The particular geometry studied in this thesis shown in figure 1 2 (c) is that of a re-entrant cavity design, in which an extended helical coil is is placed in a dielectric envelope inside the plasma chamber, this particular geometry is under consideration for lighting sources [13, 14] as well as ion sources for fusion experiments [15, 16]

1.2 Motivation

It is in the context of the preceding discussion that the work presented in this thesis was embarked upon The endeavour was motivated by a desire to complement and extend the rapidly growing body of experimental, theoretical and computational modelling work which has been carried out over recent years on the subject of the radio frequency inductively coupled plasma In particular the aim was to do experiments that would reinforce modelling results on two aspects of the operation of the ICP namely the E to H mode transition and collisionless power absorption in low-pressure plasmas With regard to the E to H mode transition, it was envisaged that the experiments would elucidate on the experimental work

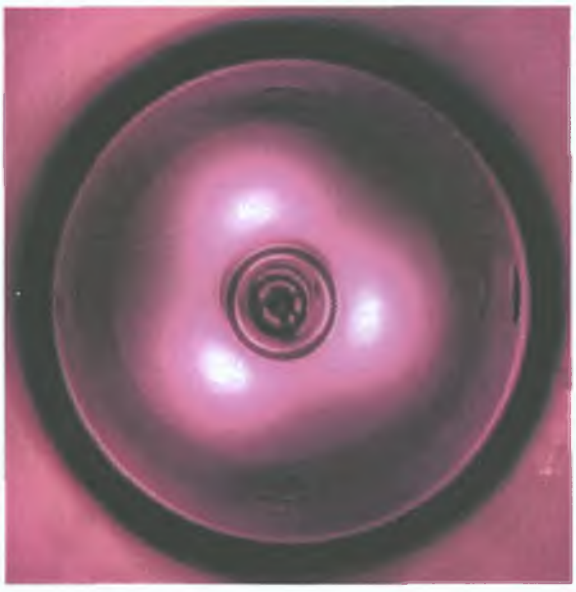

Figure 1.3: *Photograph of instability in the system*

previously published by Kortshagen et al [17], Suzuki et al [18] and El-Fayoumi and Jones [19, 20] as well as support the theoretical and modelling results of Turner and Lieberman [21]. With regard to the investigation of collisionless power absorption, there has been a considerable amount of work on the anomalous skin effect and collisionless power absorption in ICPs in the last 10 years, especially with theoretical and modelling approaches [10, 22, 23, 24, 25, 26, 27, 28, 29] . Liebermann and Godyak [14] and Kolobov and Economou [24] give a complete historical review of these papers. However experimental evidence of a quantitative nature is confined to a limited number of works, most notably Godyak et al [9, 30]. The results presented in chapter 3 of this thesis essentially corroborate the results of Godyak et al but are performed in a completely different geometry.

A further challenging problem which emerged in the initial stages of the in-

vestigation was that of gross instabilities of the kind shown in figure 1 3 the investigation of these structures was considered to be instructive since recent reports of such phenomena in RF plasmas were rare [31, 32, 33]

1.3 Outline of the thesis

The remainder of chapter 1 consists of a brief introduction to basic plasma physics In chapter 2 the experimental setup, chamber design, instrumentation and plasma diagnostics which were used to obtain the results for this thesis are described in detail Chapter 3 contains the results of the investigation of power coupling mechanisms, chapter 4 deals with the E to H mode transition in the system Chapter 5 details the results of the investigation into the instabilities mentioned above Finally, chapter 6 consists of a conclusion and some suggestions for further work

1.4 Introduction to plasma physics

Plasma physics had its origins in the last century with the study of electrical discharges through gases, however in recent years the topic has undergone somewhat of a renaissance due to the myriad new applications of plasmas in such diverse areas as materials processing, semi-conductor manufacturing, aeronautical engineering, space science, lighting, and last but not least the much sought after prospect of thermo-nuclear power generation It is the development of these applications that have put plasma technology and its associated disciplines at the centre of a multi-billion dollar industry

1.5 Plasmas in Nature

It is estimated that over 99% of the visible universe is in a plasma state, this estimate seems reasonable considering the fact that the interiors and atmospheres of stars, nebulae and interstellar gases are in a plasma state Indeed, before one even leaves this planet one must pass through Earth's upper atmosphere much of which is in a plasma state The reason why we live in one of the very few corners of the universe which is not in a plasma state can be understood by considering the Saha equation [34] which gives the degree of ionisation to be expected in a gas at thermal equilibrium

$$\frac{n_i}{n_n} \approx 2\,4 \times 10^{15} \frac{T^{\frac{3}{2}}}{n_i} \exp\left(\frac{-U_i}{kT}\right) \qquad (1\,1)$$

Where n_i and n_n (cm^{-3}) are the ion and neutral particle densities T (in degrees Kelvin) is the gas temperature k is Boltzmann's constant and U_i is the ionisation energy of the gas in units of ergs (1eV=1 6×10^{-12} erg) When the Saha equation is applied to nitrogen at room temperature and atmospheric pressure the ratio of ions to neutrals predicted is of the order of $n_i/n_n \approx 10^{-122}$ While the Saha equation predicts this ridiculously low ionisation degree for air under normal terrestrial temperatures and pressures it nevertheless predicts some degree of ionisation which leads to the question of the definition of a plasma

1.6 Definition of a Plasma

A plasma is a quasineutral collection of ions, electrons and neutral atoms or molecules which exhibit collective behaviour

The condition of quasineutrality requires that within the volume of the plasma there must be equal numbers of positively and negatively charged particles The defining condition of collective behaviour is a plasma phenomenon which like most of the major plasma phenomenon has its origins in the fact that charged particles can interact with each other by long-range electric and magnetic forces The electric field due to a point charge decreases as the inverse square of the distance from the charge whereas, for a constant charge particle density, the number of charges that it influences increases as the cube of the distance Thus the motion of every charged particle in the collection is influenced by every other charged particle This is quite unlike the processes involved in the motion of an ordinary gas where molecules or atoms move independently of one another and only interact during collisions

A quantitative definition of a plasma based on the phenomenon of *Debye shielding* relies on the relationship between the size of the plasma and the key plasma parameters of plasma density n_i and plasma temperature T The plasma temperature refers to the characteristic temperature of a gas in thermal equilibrium with a Maxwellian energy distribution Laboratory plasmas are generally not in thermal equilibrium but rather exist in a steady state where each species in the plasma is in a seperate partial thermal equilibrium, and each has its own characteristic temperature, in such a case the important temperature for the purpose of the plasma definition is the temperature of the hottest species, usually electron temperature T_e

1.6.1 Debye Shielding

Since plasmas are quasmeutral and almost free of electric fields then $n_i \approx n_e$ everywhere within the volume of the plasma However, if a charged conductor is placed in the plasma it will attract oppositely charged particles and repel like charged particles Thus in a short time span an envelope of oppositely charged particles will have surrounded the charged conductor shielding the rest of the plasma from the electric field associated with the charged conductor This phenomenon is referred to as Debye shielding It is obvious that within this shielding region, the plasma is not quasineutral and the characteristic length of this break from quasineutrality is the defining characteristic called the *Debye length* The envelope of oppositely charged particles is called a *sheath* and its size is of the order of a few Debye lengths The Debye length is calculated from the solution to Poisson's equation,

$$\nabla^2\phi = -\frac{e}{\epsilon_0}(n_i - n_e), \tag{1 2}$$

In one dimension Poisson's equation can be written as,

$$\frac{d^2\phi}{dx^2} = -\frac{e}{\epsilon_0}(n_i - n_e), \tag{1 3}$$

The inertia of the ions is large compare to the electrons hence it can be assumed that the ions do not move significantly and that the restoration of quasineutrality is achieved via electron motion The density far away from a charged conductor is n_∞ which can be set equal to n_i in equation 1 3 The electron distribution function in the presence of a potential ϕ can be expressed as,

$$f(u) = A\exp[-(\frac{1}{2}mu^2 + e\phi)/kT_e], \tag{1 4}$$

integration of $f(u)$ over u with $n_e(\phi \rightarrow 0) = n_\infty$ yields,

$$n_e = n_\infty \exp(e\phi/kT_e), \tag{1 5}$$

substituting for n_e and n_i in equation 1 3 gives,

$$\frac{d^2\phi}{dx^2} = -en_\infty \left(\left[\exp\left(\frac{e\phi}{kT_e}\right) \right] - 1 \right) \tag{1 6}$$

This equation can be simplified using a Taylor series to give,

$$\frac{d^2\phi}{dx^2} = \frac{e^2 n_\infty}{\epsilon_0 kT_e}\phi \tag{1 7}$$

where n_∞ is the density far away from the charged conductor at potential ϕ_0 and ϕ is the potential at a distance x from the conductor The solution to this equation can be written as,

$$\phi = \phi_0 \exp(-\frac{\mid x \mid}{\lambda_D}) \tag{1 8}$$

where the Debye length λ_D is defined as

$$\lambda_D = \left(\frac{\epsilon_0 kT_e}{e^2 n_e} \right)^{\frac{1}{2}} \tag{1 9}$$

where n_e is the plasma density Thus quasineutrality will exist in an ionised gas if the dimensions L of the system are large compare to the Debye length Also for Debye shielding to be statistically valid there must be a large number of particles N_D in a *Debye sphere* i e a sphere of radius λ_D

1.6.2 Plasma Frequency

In a plasma when the charges are not subject to external forces they are moving around with a distribution of thermal velocities When the plasma is perturbed in

some way the plasma reacts in order to preserve quasineutrality The time scale on which this reaction occurs is related to a quantity known as the plasma frequency ω_{pe} for the electron plasma frequency and ω_{pi} for the ion plasma frequency, both have the same form and are given by

$$\omega_{pe} = \left(\frac{ne^2}{\epsilon_0 m_e}\right)^{\frac{1}{2}} \tag{1 10}$$

and,

$$\omega_{pi} = \left(\frac{ne^2}{\epsilon_0 m_{ion}}\right)^{\frac{1}{2}} \tag{1 11}$$

where m is the electron or ion mass Since the electron mass is much smaller than the ion mass it is usual for the electron kinetics to dominate plasma response processes such as Debye shielding

The plasma frequency gives rise to one more criterion for an ionised gas to be classified as a plasma, namely that the plasma frequency has to be greater than the frequency of collisions between charged particles and neutrals otherwise the particle motion is controlled by hydrodynamic forces rather electromagnetic forces If ω is the frequency of a typical oscillation and τ is the mean time between collisions then $\omega\tau > 1$ is a necessary condition for a plasma to exist

In summary the three conditions a plasma must satisfy are

1 $\lambda_D \ll L$

2 $N_D \gg 1$

3 $\omega\tau > 1$

1.7 Types of Plasmas

While any system which meets the criteria laid out in section 1 6 can be regarded as being in a plasma state, the criteria allow for the existence of a great variety of properties and characteristics in different plasmas Plasmas can be naturally occurring or artificially produced in the laboratory, they can be produced at greater than atmospheric pressure or below atmospheric pressure, they can be hot or cold, they can be partially ionised or fully ionised To distinguish between plasmas it is necessary to measure or determine some basic plasma parameters that are attributes of all plasmas that allow us to compare and contrast plasmas of different origins both natural and artificial

1.7.1 Plasma Parameters

In this section some of the more basic plasma parameters are discussed with a view to categorising some of the many different kinds of plasmas

Plasma Number Density

The plasma number density n is a fundamental plasma parameter and is defined as the number of positive or negative charges per unit volume, throughout this thesis the plasma density is expressed in units of cm^{-3} In an electro-positive plasma $n_i = n_e = n$ The fractional ionisation of a plasma is a term related to the plasma density and refers to the ratio of charged particles density to the total particle density, and is given by,

$$x_{iz} = \frac{n_i}{n_g + n_i} \tag{1 12}$$

where n_g is the neutral gas density x_{iz} is equal to one for fully ionised plasmas and $x_{iz} \ll 1$ for the weakly ionised plasmas which are the subject of this thesis

Temperature

For ionisation of a particle to occur the particle must gain an amount of energy equal to its ionisation energy In a plasma this energy is usually gained from collisions with other particles The amount of energy required depends on the gas involved but is typically tens of electron volts (eV) The particles of any gas in thermal equilibrium have a range of energies The energy distribution function describes the number of particles in any given energy interval In the absence of any external forces, the particles of a gas will, due to elastic scattering collisions, relax to a Maxwellian distribution with a characteristic temperature T,

$$f(u) = n(\frac{m}{2\pi kT})^{\frac{3}{2}} \exp\left[\frac{-mu^2}{2kT}\right], \tag{1 13}$$

where $f(u)du$ is the number of particles per cm^{-3} with velocity between u and $u + du$ The temperature is related to the energy and speed of the particles by

$$E = \frac{1}{2}mv_{th}^2 = \frac{3}{2}kT \tag{1 14}$$

While in a normal gas in thermal equilibrium the energy distribution of the atoms or molecules can be characterised in terms of a Maxwellian distribution with a characteristic temperature, one interesting feature of plasmas is that each individual species of particle, ions, electrons and neutrals can have different temperatures This is because the energy transfer function for collisions between particles depends on the ratio of the masses of the particles in such a way that particles of similar mass share energy with each other very efficiently while particles of

different mass do not to share energy so efficiently In stable steady-state low-pressure plasmas i e where ion production is precisely balanced by ion loss, it is usually the case that the ions and the electrons are at very different temperatures with the electron temperature generally being greater than the ion temperature It is plasmas of this type that are under consideration in this thesis and the temperature of interest is the electron temperature T_e

Plasma and Floating Potential

In a plasma which is generated and confined in a grounded vessel the electrons being lighter and more energetic move more quickly to the walls of the vessel where they are lost Since the plasma must be quasineutral and field-free it adjusts itself to a positive potential with respect to the potential of the vessel walls in order to contain the more mobile species (i e electrons) and balance electron and ion fluxes to the walls, this potential is called the *plasma potential* (V_p) or *space potential* Along with the plasma potential there is an associated *floating potential* V_f (with respect to ground) this is the potential at which an isolated substrate in the plasma will draw no net current, since the floating potential is required to repel most of electrons coming from the plasma it must always be less than the plasma potential

1.7.2 Industrial Plasmas

Thermal Plasmas

Industrial process plasmas can generally be divided into two categories, thermal and non-thermal plasmas Thermal plasmas are plasmas in which the electrons are in thermal equilibrium with the ions in the gas They are characterised by $T_{ion} = T_e$ These plasmas have many applications in modern industry They are useful in the processing and refining of metals and particularly so when working with highly reactive metals and alloys as the melting process can be done in an inert atmosphere, processes such as cutting and welding of metals can be can be carried out to great precision using thermal plasmas Thermal plasmas also find applications in various surface treatments of materials such as laying down wear resistant, oxidation resistant, thermal barrier or bio-compatible coatings

Non-Thermal Plasmas

Non-thermal plasmas are plasmas in which the electrons and ions are not in thermal equilibrium and usually the electrons have a much higher temperature These plasmas generally have a low degree of ionisation and often have complex chemistry The fact that the electrons and ions have different temperatures with $kT_e \gg kT_i$ leads to the situation where chemically reactive radicals can be produced from relatively inert molecules and atoms in an environment where the bulk material is at a temperature which is only marginally above room temperature This 'hot' chemistry at relatively low temperatures is the key to many industrial applications which have revolutionised the electronics and computer

industries in the last few decades

Non-thermal processing plasmas operate at low gas pressures (up to a few hundred mTorr) and electron temperature of the order of 10^5K and ion temperatures of the order of a few 100 K Electron densities in these discharges range from $10^8 - 10^{12}$cm^{-3} Low temperature plasma processing technologies are based on etching and deposition of material These processes take place in confined plasma reactors in which feedstock gas is broken into ions, radicals and electrons which then physically and chemically react with the substrate material to be processed

1.7.3 Classification of Plasmas

A useful and convenient way to classify plasmas is to do so in terms of two fundamental parameters of all plasmas namely the plasma density and the electron temperature Figure 1 4 shows where different types of plasmas fit on a log-log plot of temperature v electron density [35] The rf inductively coupled plasmas which are the subject of this thesis have an electron temperature range of 1-5 eV and a density range of 10^9-10^{11} cm^{-3}

1.8 Plasma Applications

The application of plasma science to a great variety of industrial, technological and scientific endeavours over the past three decades has led the development of plasma technology as a multi-billion dollar industry Plasma technology has infiltrated the modern industrial world to such an extent that one can reason-

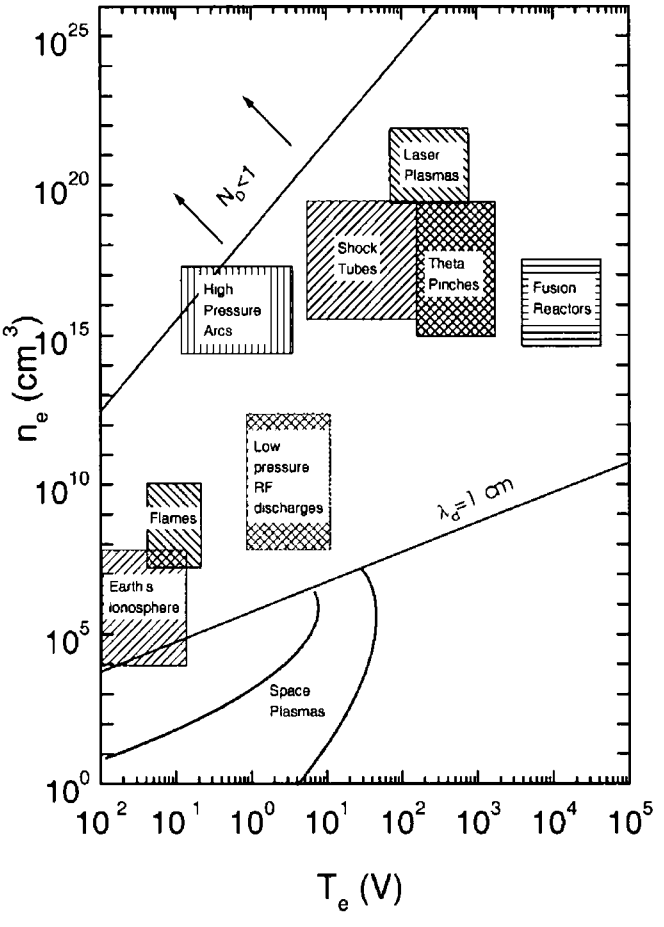

Figure 1 4 *Various types of plasmas on an n_e versus T_e plot* [35]

ably compare its impact on modern industry with the impact that the advent of the steam engine had on the industrial revolution of the 19^{th} century Plasma science underlies a vast amount of technological and scientific research from the development of new light sources to the development of new energy sources But nowhere has it impacted on more than the electronics and computer industry The need for faster, cheaper, smaller microchips has driven much of the present day research into low temperature plasmas

Plasmas are a fundamental tool in the manufacture of integrated circuits,

indeed by the time that a Pentium microprocessor reaches the motherboard of a modern PC it will have undergone up to 100 plasma based processing stages These stages include the implantation of dopant atoms into silicon, the selective removal of silicon film, the etching of the features on the chips, the deposition of new metal layers on the chip, the modification of the chips' surface and the removal of the photoresist used in the etching process

1.9 Fundamental Processes in Plasmas

In this section some fundamental processes which govern the behavior of the plasma are discussed These processes include collisions, diffusion and transport in plasmas

1.9.1 Collisions

There are two main types of collisions that occur in plasmas The first type, elastic collisions, are collisions in which the internal energies of the colliding particles do not change, the second type are inelastic collisions During inelastic collisions the internal energy of at least one particle involved in the collision changes Both types of collisions play critical roles in determining the over all character and behaviour of the plasma Elastic collisions play a key role in such attributes as the conductivity, mobility, diffusion, and form of the electron energy distribution function Inelastic collisions determine the electron and ion density, the electron temperature and the radiation output from the plasma

1.9.2 Elastic Collisions

In elastic collisions kinetic energy is transferred from one particle to the other These collisions can occur between all types of particle and at all energies Elementary arguments based on the principles of conservation of energy and momentum dictate that the maximum fractional energy transfer from one particle to another is of the order of $2m_1/m_2$ where m_1 is the mass of the less massive particle, therefore in a plasma containing electrons, ions and neutral atoms, the atoms and ions tend to share energy very efficiently, with themselves and each other since $m_{ion} \approx m_{atom}$, while the electrons tend not to share their kinetic energy with the atoms and neutrals since $m_{ion} \approx 75000\, m_e$ (for argon) It is for this reason that in low temperature ICPs the electrons which are preferentially heated by the RF electric fields are not in thermal equilibrium with the ions and neutrals This situation has many advantages in the field of processing plasmas since it is possible to utilise the chemistry of relatively hot electrons in a system where the ambient temperature is relatively cool

Elastic collisions between charged particles are known as Coulomb collisions They differ from collisions between neutral particles in that the electric field becomes important when the distance between two charged particles is less than the Debye length, λ_{De} Coulomb collisions tend to Maxwellianise the electron energy distribution function and they play a much more influential role as the degree of ionisation increases

1.9.3 Inelastic Collisions

Inelastic collisions can occur if the energy transferred from one particle to another is sufficient to change the internal energy of one of the colliding particles Inelastic collisions take several different forms depending on the amount of energy transferred during the collision and the state of the internal energy in the colliding particles In keeping with the principle of conservation of energy inelastic collisions can be represented as follows,

$$\frac{1}{2}m_1v_1 + \frac{1}{2}m_2v_2 = \frac{1}{2}m_1u_1 + \frac{1}{2}m_2u_2 + \Delta E, \qquad (1\ 15)$$

where $v_{1,2}$ and $u_{1,2}$ are the initial and final velocities of the particles and ΔE is the net change in the particles internal energy as a result of the collision The change in energy ΔE can be positive as in the case of an excitation collision or it can be negative as in the case of a de-excitation collision While there is a great variety of different inelastic collisions, the most important in relation to electron-atom collisions are ionisation and excitation

1.9.4 Ionisation

Electron impact ionisation occurs when an energetic electron collides with an atom and an electron is liberated from the atom

$$Ar + e \rightarrow Ar^+ + 2e \qquad (1\ 16)$$

ionisation from the ground state can only occur if the energy of the fast electron is greater than the ionisation energy for the atom The ionisation energy of the atom varies from one atom to another and in argon is approximately 15 7 eV

Typical low-pressures argon inductively coupled plasmas have electron temperatures of 1-5 eV hence the ionisation from ground state is largely determined by the relatively small population of electrons in the high energy tail of the electron energy distribution function

1.9.5 Excitation and Relaxation

Excitation occurs when an energetic electron collides with an atom and the absorbs enough energy to promote an electron to a higher energy level The atom is then left in an excited state and the electron moves off with reduced kinetic energy Most excited atoms can quickly de-excite to a lower energy state or to the ground state by electric dipole radiation This reaction can be represented as,

$$e + Ar \rightarrow Ar^* + e \rightarrow Ar + e + \hbar\omega \qquad (1\ 17)$$

where Ar* denotes the excited atom $\hbar\omega$ is the energy of the photon released in the process The photon released, which can be in the visible or UV part of the electromagnetic spectrum, is the main contributor to the light output from the plasma The timescale for electric dipole radiation is of the order of 10^{-9} s whereas the characteristic time between collisions in a typical low pressure ICP is about two orders of magnitude longer hence most excited atoms tend to de-excite without undergoing further collisions which could lead to ionisation However certain excited states do not satisfy the quantum mechanical selection criteria required for electric dipole radiation and must decay in some other fashion *e g* electric quadrupole radiation or magnetic dipole radiation, but these mechanisms have longer characteristic time-scales associated with them, consequently if these

time-scales are comparable with the inter-collisional timescales then such atoms may undergo further collisions leading to ionisation Atoms in excited states which are unable to undergo electric dipole radiation are called *metastable atoms* Metastable atoms can play an important role in the operation of low pressure ICPs due to their involvement in the process of two-step ionisation [36] In section 4 2 2 this role is discussed and investigated

1.9.6 Recombination

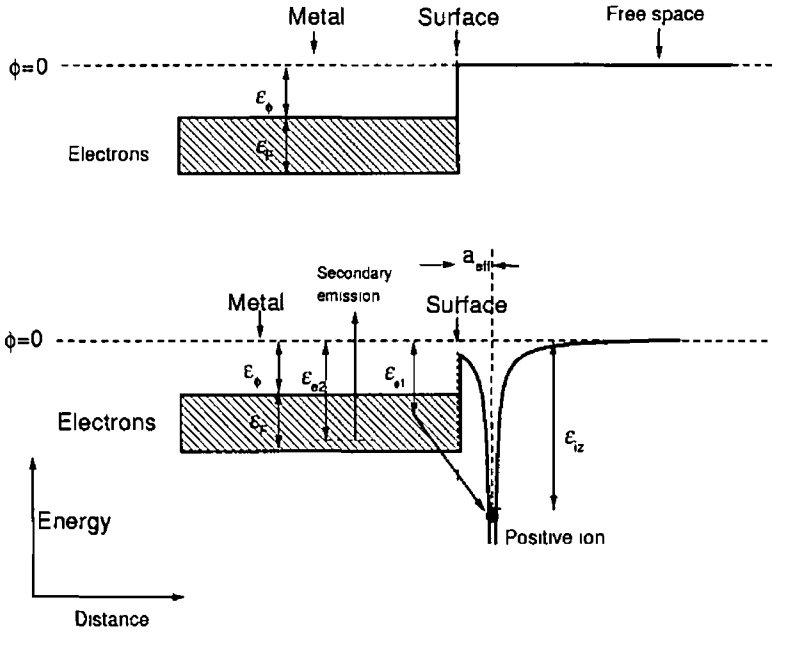

Figure 1 5 *Energy diagram for positive ion neutralisation and secondary emission at a metal surface (a) shows the Fermi energy, ε_F and work function, ε_ϕ (b) Shows neutralisation and emission* [5]

Consideration of the principles of conservation of energy and momentum mean that recombination due to an electron-ion collision ($e + A^+ \rightarrow A$) is impossible or

nearly impossible allowing for the Heisenberg uncertainty principle, therefore any recombination that takes place in a plasma must involve some other mechanism In general recombination in low temperature plasmas takes place in the presence of a third body This third body allows for the conditions in which the principles of conservation of energy and momentum can be satisfied simultaneously Three-body recombination can occur within the volume of a plasma with a rate constant $k \propto T_e^{-9/2} n_e$ but calculations show that the process is not important in low pressure ICPs with $T_e \geq 1$ and $n_e \leq 10^{13}$ [5] It follows that particle losses are dominated by surface reactions at the walls of the vessel containing the plasma The relevant reaction is

$$e + A^+ + S \rightarrow A + S \qquad (1\ 18)$$

where S is the surface wall atom The energy diagram for the process is illustrated in figure 1 5 When a positive ion approaches the surface to within an atomic radius (a_{eff}), a deep potential well is created which is separated from the surface by a narrow potential barrier An electron with energy ε_e can tunnel through the barrier to neutralise the ion This reaction can take place if the ion energy at the surface is greater than the work function of the surface material A simple classical estimate of the work function for a metal gives values of the order of $4 - 6$ V for most metals and since the ion energy at the surface is > 10 V for typical ICPs then practically all ions are neutralised at the surface In the interaction of an ion and an electron from the surface of the walls, the electron either attaches itself to the ion to make an excited state atom which may or may not be metastable Alternatively the electron can attach itself to the ground state of the atom and its excess energy can be absorbed by another electron from the

wall leading to the emission of a secondary electron, these secondary electrons can play an important part in the operation of low pressure [37] discharges

1.9.7 Other collision processes

Apart from the aforementioned processes there are many other inelastic collision processes taking place in plasmas, these include a great variety of inelastic molecular processes such as

$$e + AB \rightarrow A + B + e \qquad \text{Electron impact dissociation} \qquad (1\ 19)$$

$$e + AB \rightarrow A + B^+ + 2e \qquad \text{Dissociative ionisation} \qquad (1\ 20)$$

$$e + AB^+ \rightarrow A + B^* \qquad \text{Dissociative recombination} \qquad (1\ 21)$$

$$e + AB \rightarrow A + B^- \qquad \text{Dissociative electron attachment} \qquad (1\ 22)$$

$$e + AB \rightarrow A^+ + B^- + e \qquad \text{Polar dissociation} \qquad (1\ 23)$$

1.9.8 Cross Sections

The rate at which electron impact ionisation occurs in a plasma is governed by the number of neutral gas atoms, the electron velocity and the cross section for the process,

$$\nu_{iz} = n_g \sigma_{iz} v, \qquad (1\ 24)$$

where σ_{iz} is the cross section for ionisation and v is the velocity and n_g is the neutral gas density

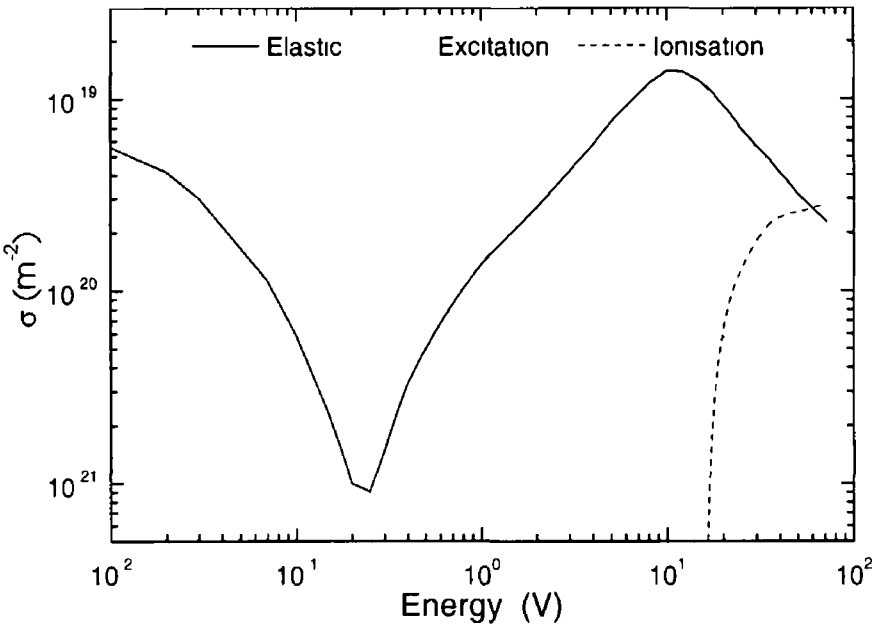

Figure 1 6 *Excitation, ionisation and elastic scattering cross sections for argon [38, 39]*

Figure 1 6 shows the elastic, ionisation and excitation cross sections for argon as a function of energy [38, 39] Since excitation and ionisation are threshold processes there cross sections are zero below the thresholds In the case of argon the ionisation threshold is 15 76 eV and the excitation threshold is 11 55 eV It is clear therefore that in a typical ICP with $T_e \approx 1 \sim 3$ eV the ionisation and excitation rates are extremely sensitive to the high energy tail as well as the form of the electron energy distribution function

1.10 Diffusion

The macroscopic force equation for a fluid of charged species in a steady-state isothermal plasma is given as [5],

$$qn\mathbf{E} - kT\nabla n - mn\nu_m\mathbf{u} = 0 \tag{1 25}$$

where the $qn\mathbf{E}$ term is due to the electric field, the $kT\nabla n$ is the pressure gradient term and $mn\nu_m\mathbf{u}$ is the frictional term which arises from collisions with the background species with a constant momentum transfer collision frequency ν_m and drift velocity $\mathbf{u}$ Equation 1 25 can be solved for $\mathbf{u}$ yielding,

$$\mathbf{u} = \frac{qE}{m\nu_m} - \frac{kT}{m\nu_m}\frac{\nabla n}{n} \tag{1 26}$$

which can be re-written as,

$$\Gamma = \pm\mu n\mathbf{E} - D\nabla n \tag{1 27}$$

where Γ is the flux and μ is the particle mobility coefficient given by,

$$\mu = \frac{|\,q\,|}{m\mu_m} \tag{1 28}$$

and D is the diffusion coefficient given by,

$$D = \frac{kT}{m\nu_m} \tag{1 29}$$

1.10.1 Free Diffusion

The diffusion and mobility constants are calculated separately for each species in the plasma and in the absence of electric fields the particle flux is related to the density gradient by Fick's law,

$$\Gamma = -D\nabla n \tag{1 30}$$

Equation 1 30 coupled with the continuity equation

$$\frac{\partial n}{\partial t} + \nabla (n\mathbf{u}) = S \tag{1 31}$$

where S is the ionisation source term, derive the free diffusion equation

$$\frac{\partial n}{\partial t} + \nabla(D\nabla n) = S \tag{1 32}$$

1.10.2 Ambipolar Diffusion

In a plasma the condition of quasi-neutrality must hold This implies that any flux of electrons out of a particular region must be precisely balanced by an identical flux of ions i e $\Gamma_e = \Gamma_i$ but since electrons are much lighter their mobility is much higher so they will initially leave a plasma region at a greater rate than the ions This causes a charge imbalance and an electric field which results in a departure from the free diffusion situation so that quasi-neutrality can be restored By equating the electron and ion flux the electric field is determined to be,

$$\mathbf{E} = \frac{D_i - D_e}{\mu_i + \mu_e}\frac{\nabla n}{n}, \tag{1 33}$$

where $D_{i,e}$ and $\mu_{i,e}$ are the free diffusion and mobility constants for electrons and ions Using the expression for $\mathbf{E}$ from equation 1 27 the ambipolar diffusion coefficient is derived as,

$$D_a = \frac{\mu_i D_e + \mu_e D_i}{\mu_i + \mu_e} \tag{1 34}$$

In a typical low pressure ICP such as the source under consideration in this thesis the plasma is weakly ionised and $T_e \gg T_i$ under these circumstances the following approximations can be made

1 $D_a \approx D_i \left(1 + \frac{T_e}{T_i}\right)$

2 $\Gamma_i \approx \mu_i n\mathbf{E}$

It should be noted that the above treatment of diffusion is valid only for plasmas without substantial static magnetic fields which greatly the motion of the electrons in the plasma In the case of plasmas with magnetic fields (very much larger than the induced rf magnetic field in typical ICPs), charged particles have different diffusion coefficients parallel to and perpendicular to the magnetic field lines This is of considerable importance when dealing with magnetically confined sources such as magnetrons and also in high temperature magnetically confined fusion plasmas [34]

Chapter 2

Experimental Setup & Plasma Diagnostics

In this chapter, the experimental setup, chamber design, Instrumentation and plasma diagnostics, which were used to obtain the results for this thesis, are described in detail

2.1 Experimental Setup

2 1 1 The Discharge Chamber

The schematic diagram of the discharge chamber is shown in figure 2 2 The chamber consists of a cylindrical stainless steel vacuum vessel of internal diameter 20 cm and length 80 cm mounted on a steel ground plate One end of the cylinder is sealed with a Pyrex class window 1 5 cm thick, the other end is sealed with a steel flange in the middle of which there is a 5 cm diameter port into which is

Figure 2.1: *Photograph of experimental system*

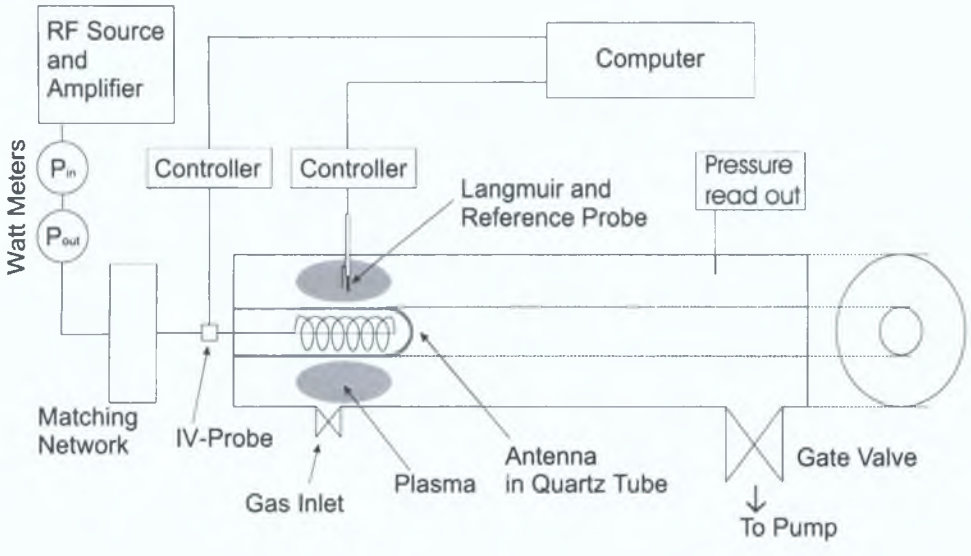

Figure 2.2: *Schematic diagram of the experimental system*

inserted a quartz tube 30 cm long with wall thickness 3 mm, which houses the antenna The walls of the chamber contain eight ports to allow access for the probes, pressure gauges and the spectrometer

The chamber is evacuated through a 10 cm pumping port by means of a 230 l/s turbo molecular pump backed by a rotary pump The pumps are capable of producing a base pressure of $< 10^{-6}$ Torr A gate valve is situated between the chamber and turbo pump The pressure is monitored by Baratron and Pirani gauges mounted at the antenna end of the chamber Gas from argon, helium and oxygen cylinders is fed through three Tylan MKS gas-flow controllers and through a manifold that is in turn connected to the chamber via a port under the antenna The flow controllers have a range of 0-100 sccm for argon and helium and a range of 0-10 sccm for oxygen The gas pressure in the chamber when the flow controllers are fully opened is $\approx$ 30 mTorr In order to achieve higher pressures (up to 3 Torr) the gate valve is partially closed

2.1 2 RF Power Supply

A Marconi 2022D function generator is used to provide a 13 56 MHz signal which is amplified by an ENI radio-frequency power amplifier which has a maximum power output of 1 5 kW The Marconi can be pulsed using an external pulse generator The RF power is fed to the antenna via an RFPP AM20 automatic matching network The matching network is mounted on rails which allow the smooth translation of the antenna in and out of the chamber along the axial direction The antenna shown in figure 2 3 is constructed from 4 mm diameter copper tubing, the coil is 10 cm long with 11 turns and a diameter of 4 cm and is

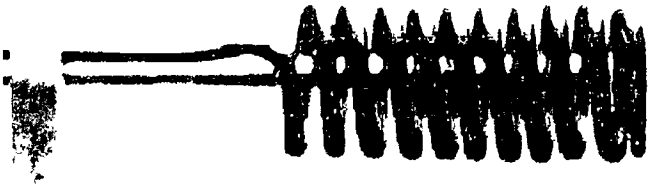

Figure 2 3 RF Antenna

connected in place of the inductor in the matching unit The antenna is positioned in the centre of the quartz tube such that the middle winding of the coil is positioned directly under the second access port The matching unit and antenna can be moved in the axial direction in order to position the antenna relative to the probes The quartz tube is used to prevent the antenna from coming into direct contact with the plasma and the antenna is kept at atmospheric pressure Since antenna resistance can change as it becomes heated during operation, it is necessary to reduce the effect by water cooling the antenna

To minimise radiated power loss, which can be significant at high frequency, all transmission lines are high quality double-shielded coaxial cable also RF connectors, terminators and cables are regularly checked This is also good practice for safe operation in a RF environment

2.2 Instrumentation

In this section the control and display instrumentation employed in the experiments are discussed They include the directional power meter, the RF matching unit, the pulse delay generator, the fast oscilloscope and the 50 cm spectrometer The precision and reliability of the instruments are considered and any modifications made are described

2.2 1 The Power Meter

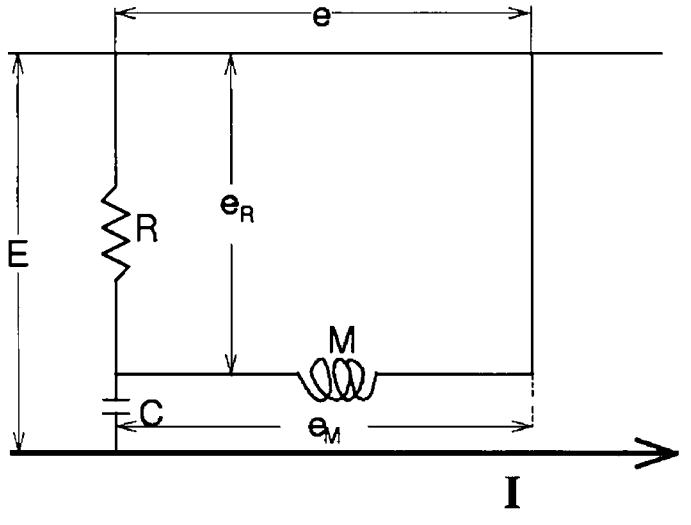

Figure 2 4 *Circut diagram for the Bird model 43 RF power meter*

Since RF power is used as a control parameter for many of the experiments in this thesis, the precise measurement of it is of critical importance In general RF power supplies used to generate plasmas have a characteristic output impedance of 50 Ω and maximum power will only be transferred to a purely resistive load

of 50 Ω In order to achieve maximum power transfer a matching network is thus added to the plasma load and is tuned to make the combination of plasma and matching unit equal to the characteristic output impedance of the power supply (*i e* 50 Ω) However if the load is not matched then a proportion of the input power is reflected back along the transmission line to the power supply The matching unit employed in these experiments is capable of automatically setting itself for maximum power transfer, but the time response of the matching unit to any significant change in the plasma impedance is at best a few seconds, for this reason the matching unit is set to manual during pulsed experiments This means that for most of the pulse the power is unmatched and a significant proportion of it is reflected, it is thus necessary to measure both the forward and reverse power in the transmission line To this end a directional power meter, Bird model 43 is used, it has a power range of 1 W to 3 kW and a frequency range of 0 45 MHz to 2300 MHz The meter contains a rotating plug-in sensing element which measures power in the direction in which it is pointed The basic sensing circuit of the element shown in figure 2 4 consists of a mutual inductance M between the loop and the centre conductor and the voltage divider C and R Referring to figure 2 4 E is the voltage between the outer and centre conductor and I is the current The output voltage to the meter is the sum of two samples

$$e_R = j\omega REC \text{ and } e_M = j\omega I(\pm M) \qquad (2\ 1)$$

The voltage across the loop is either positive or negative depending on the direction The value of the resistor R is set such that $R \ll X_C$ and the components

are chosen so that

$$CR = \frac{M}{Z_0} \tag{2.2}$$

where Z_0 is the characteristic impedance of the transmission line, which is generally 50 Ω. The voltage on the meter is now

$$e = e_R + e_M = j\omega M \left(\frac{E}{Z_0} \pm I \right) \tag{2.3}$$

At any point on the transmission line the voltage E is equal to the sum of the forward and reflected voltages $E_r + E_f$ and the current is equal to the difference of the forward and reverse current

$$I = \frac{E_f}{Z_0} - \frac{E_r}{Z_0} \tag{2.4}$$

When the element is pointing towards the load, the output voltage is

$$e = \frac{2j\omega M E_f}{Z_0} \tag{2.5}$$

and on turning the element to face the power supply the output voltage is

$$e = \frac{-2j\omega M E_r}{Z_0} \tag{2.6}$$

The output voltage is rectified and normally displayed on a meter calibrated in RF watts [40], but in some experiments described in this thesis the output voltage is disconnected from its moving-coil meter and instead, is displayed on a digital oscilloscope

2.2.2 The Matching Network

The matching unit used throughout the experimental program is a RFPP AM20 automatic matching unit. The network is the standard 'L' configuration comprising of a fixed coil and a series capacitor to handle the tuning and a shunt

capacitor to handle the loading Both capacitors are controlled by servo motors which operate simultaneously In these experiments, the fixed coil is removed and the antenna coil is put in its place The matching unit is also modified to house the antenna current-voltage probe The matching is located as close to the plasma chamber as possible At normal operating pressures and powers the matching unit has a range of approximately 4 MHz *i e* (13 56 ± 2) MHz The frequency range of the matching unit can be changed by adding or removing a number of fixed capacitors in parallel with the load capacitor

2.2.3 The Delay Generator

Time resolved Langmuir probe measurements shown in section 5 are made with the aid of a Stanford Research *SR 535* delay generator This instrument is capable of producing a TTL pulse of any duration up to 100 seconds The pulse is emitted after a pre-set time delay following a triggering signal being received by the generator The emitted pulse can be used to trigger the Langmuir probe in boxcar averaging mode Picosecond time resolution and precise trigger level setting is possible which allows for the investigation of the dynamics of seemingly discontinuous and transient phenomena such as those encountered in the investigation of the E to H mode transition

2 2.4 The Oscilloscope

The oscilloscope used throughout this project is a Hewlett Packard HP-54510A digital oscilloscope This two channel scope has a sampling rate of 2 GSs^{-1} and is capable of averaging up to 256 repetitions of a signal The scope has a

GPIB interface which allows the user to control the setup and acquisition of data directly from a computer A LabVIEW© driver for the HP-54510A obtained from National Instruments was modified and incorporated into a LabVIEW© program which enabled synchronous time-resolved data acquisition from many instruments

2.3 Diagnostics

In this section the principal plasma diagnostics used to determine the plasma parameters and its electrical characteristics are described They include the RF current and voltage probe, the Langmuir probe and the magnetic field (B) probe The theory and analysis used for parameter evaluation are also described

2.4 The Langmuir Probe

In this section the operation and construction the Langmuir probe are described Firstly in the general case of a steady state plasma where the fundamentals of probe operation are presented along with the underlying principles of probe trace analysis Secondly in the specific case of low-pressure, non-thermal RF pulsed and steady state plasmas where general probe theory is modified to account for the collisional regime, electrical noise and high frequency electric fields which are present in these types of plasmas Thirdly the Langmuir probe system used throughout this project is described and critically assessed in terms of its reliability and precision

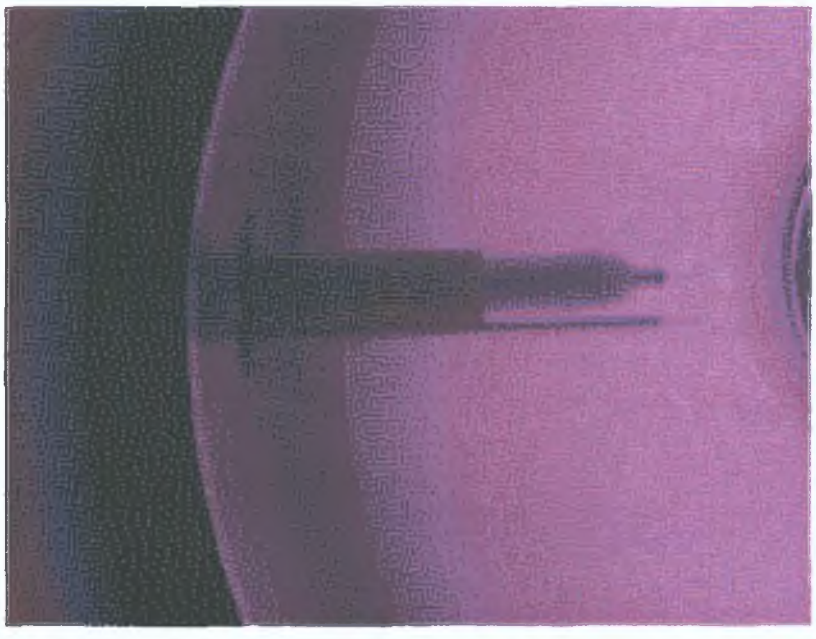

Figure 2.5: *Photograph of a Langmuir probe (top) and reference probe (bottom) in an argon plasma*

Introduction

Electrostatic probes are a widely used plasma diagnostic tool which rely on the direct sensing of the plasma particle fluxes to an electrode which is immersed in the plasma. This method was one of the earliest used for determining plasma parameters. These probes are often referred to as Langmuir probes following the pioneering work of Irving Langmuir in the operation of the electrostatic probe [41].

The Langmuir probe is one of the most versatile diagnostics available for measuring the main plasma parameters in low-temperature, low-pressure, weakly ionised discharges. The probe is capable of determining, locally within the discharge, such parameters as electron temperature, electron density, ion density,

the plasma potential, the floating potential and the electron energy distribution function (EEDF) One of the main advantages of the Langmuir probe as a diagnostic is that it can be used to obtain spatially resolved measurements of the plasma parameters as opposed to volume averaged measurements obtained from other diagnostics such as microwave interferometry and emission spectroscopy Langmuir probes can be designed to yield spatially resolved measurements of the above mentioned parameters in steady state plasmas or probe systems can be designed to yield time resolved details of the parameters in pulsed discharges

The Langmuir probe, in its simplest form consists of a thin cylindrical wire which is immersed in the plasma When the probe is biased with reference to the plasma chamber it draws a current from the plasma As the bias voltage on the probe is changed the current that is drawn from the plasma also changes The relationship between the probe bias voltage and the current drawn is the key to the Langmuir probe as a diagnostic tool Usually Langmuir probe measurements are made by setting a variable bias on the probe and recording the current drawn as a function of bias voltage This data provides a characteristic Langmuir probe trace such as the one shown in figure 2 6 is determined

2 4 1 The Langmuir Probe Trace

A typical Langmuir probe trace such as the one shown in figure 2 6 is characterised by three distinct regions

The positive ion saturation region, this is where the probe potential V_{po} is negative with respect to the chamber walls At negative values of V_{po} (when

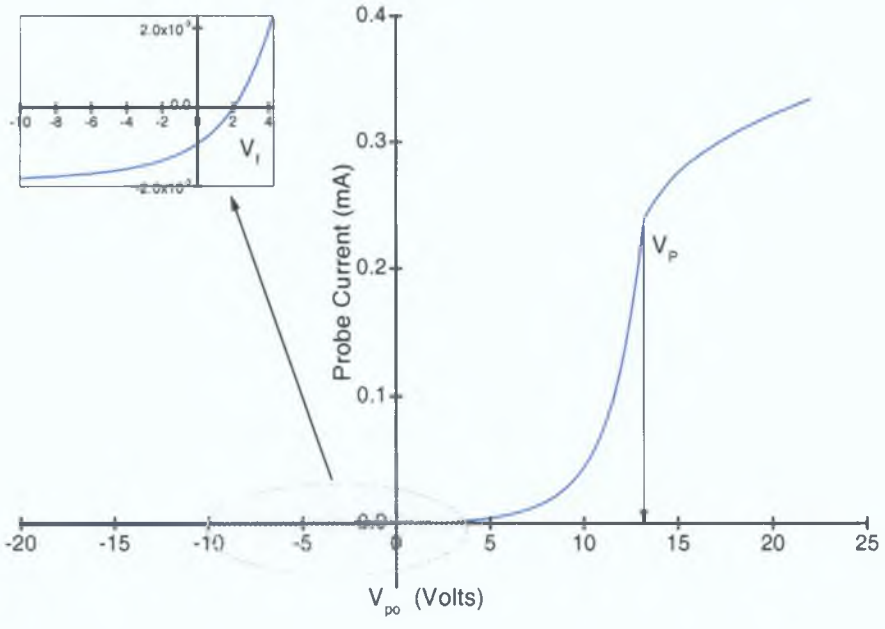

Figure 2.6: *Typical Langmuir probe trace*

$-V_{\rm po}$ is few times the electron temperature) a positive ion sheath forms around the probe and electrons (and negative ions) are repelled. The probe current collected in this region can be assumed to be purely ionic and can be analysed as described in section 2.4.1 to determine the local ion density n_i.

When the probe potential is highly positive with respect to the plasma chamber the region of the characteristic trace is referred to as the electron saturation region, in this region the current collected (in the absence of negative ions) by the probe consists entirely of electrons. In non-thermal plasmas the electron saturation current is always much greater than the ion saturation current due to the higher mobility of the electrons.

The third region in the characteristic probe trace is the transition region which lies between the ion saturation and electron saturation region. Generally this region is characterised by a rapidly changing gradient in the probe trace.

It is the analysis of this region which yields the floating potential the plasma potential, the electron temperature and under favourable conditions the electron energy distribution function (EEDF)

Langmuir Probe Theory

In this section a simplified Langmuir probe theory is presented which is based on several assumptions

- Both the probe radius and the Debye length are less than the electron collisional mean free path
- Electrons and ions have Maxwellian velocity distributions with temperatures T_e and T_i respectively
- The plasma is assumed to be infinite, homogenous and quasi-neutral in the absence of the probe
- All charged particles arriving at the probe are collected by the probe
- No dc magnetic fields are present

In the ion saturation region of the Langmuir probe characteristic the probe has a large negative bias and will thus collect only positive ions The current collected by the probe in this region is given by

$$I_{+sat} = n_0 e S v_B, \tag{2 7}$$

where n_0 is the ion density, e is the electronic charge, S is the sheath area and v_B is the Bohm velocity *i e* the minimum velocity which the ions must have at

the sheath edge [5] and is given by

$$v_B = \left(\frac{kT_e}{m_+}\right)^{\frac{1}{2}} \tag{2 8}$$

where k is the Boltzmann constant and m_+ is the ion mass

As the probe bias is made less negative with respect to the plasma potential, energetic electrons begin to make a contribution to the collected current, eventually a point is reached when the positive ion current is precisely balanced by the electron current and thus the probe draws no net current, the probe potential at this point is referred to as the floating potential V_f This is the potential at which any isolated conductor placed in the plasma will remain The floating potential is always negative with respect to the plasma potential As the probe bias is raised above this point the current starts to increase rapidly as more and more electrons are energetic enough to overcome the retarding potential along with this the ion sheath thickness decreases according to the Child-Langmuir law $s \propto \lambda_D \left(\frac{2(|V_{po}-V_p|)}{T_e}\right)^{\frac{3}{4}}$ [41] The electron density within the sheath, for a Maxwellian electron distribution, is governed by the Boltzmann relation

$$n_e = n_\infty \exp\left(\frac{e(V_{po}-V_p)}{kT_e}\right) \tag{2 9}$$

where V_{po} is the probe potential with respect to the grounded chamber, V_p is the plasma potential with respect to the grounded chamber and n_∞ is the electron density far away from the probe The electron current at the sheath edge is given by

$$I_{e0} = \frac{1}{4} n_0 e \overline{v}_e S \tag{2 10}$$

where S is the sheath area and $\overline{v}_e$ is the average electron velocity which in a Maxwell-Boltzmann velocity distribution is given by

$$\overline{v}_e = \sqrt{\frac{8kT_e}{\pi m_e}} \tag{2 11}$$

The total current to the probe in this region is the sum of the ion saturation current and the electron current which is governed by the number of electrons at the sheath edge with sufficient energy to overcome the retarding potential across the sheath

$$I_{po} = I_{+sat} + I_{e0} \exp\left(\frac{e(V_{po} - V_p)}{kT_e}\right) \tag{2 12}$$

When the probe potential is set equal to the plasma potential then the ion sheath disappears leaving no potential gradients between the plasma and the probe, therefore the current collected by the probe is as a consequence of the random thermal motion of the ions and electrons and as the electrons have far greater mobility this current is electron dominated and given as

$$I_{probe} \approx \frac{n_e e \overline{v}_e S}{4} \tag{2 13}$$

As the probe potential is raised above the plasma potential it is the ions which are repelled and thus the ion current falls off, this occurs within a fraction of a volt as the ion energy is much less than the electron energy When the probe is sufficiently positive with respect to the plasma only an electron current can reach the probe and this is referred to as the electron saturation current

$$I_{sat} = \frac{n_e e \overline{v}_e S}{4} \tag{2 14}$$

2.4.2 Probe Trace Analysis

In section 2 4 1 the relationship between probe voltage and probe current was presented Figure 2 5 shows the Langmuir probe used on all the experiments presented in this thesis is a *Scientific Systems SmartProbe*© the probe is fully automated and the probe trace analysis is performed by the Windows© based *Scientific Systems Smartsoft*© computer program In this section the analysis method used by the program, to determine the plasma parameters from the IV characteristic of a small cylindrical probe is presented A small cylindrical probe offer the advantage over the alternative planar geometry or spherical geometry in that smaller area probes reduce plasma depletion of low energy electrons thus minimising the disturbance of the plasma [42]

From the theory of Laframboise expressions for either the ion or electron current to the probe can be described as a function of applied voltage

$$\frac{I_+(V)}{I_{e0}} = f_1\left(\frac{r_p}{\lambda_d}, \chi\right), \quad \chi < 0 \tag{2 15}$$

$$\frac{I_e(V)}{I_{+0}} = f_2\left(\frac{r_p}{\lambda_d}, \chi\right), \quad \chi > 0 \tag{2 16}$$

where χ the non-dimensional probe voltage is given as

$$\chi = \frac{e(V - V_p)}{kT_e} \tag{2 17}$$

The function f is derived from numerical fits to the Laframboise curves, r_p is the probe radius, l is the probe tip length and I_{+0} and I_{e0} are the following scaling factors,

$$I_{+0} = n_+ r_p e \left(\frac{2\pi k T_e}{m_+}\right)^{\frac{1}{2}} \tag{2 18}$$

and

$$I_{e0} = -n_e r_p e \left(\frac{2\pi k T_e}{m_e}\right)^{\frac{1}{2}} \tag{2 19}$$

The above equations can be used to calculate the plasma parameters provided we have a knowledge of the plasma potential Vp the Debye length λ_d and the electron temperature kT_e To obtain this knowledge a simple analysis based on Langmuir theory is performed on the IV curve An initial estimate of the plasma potential which corresponds the potential at which the characteristic 'knee' in the IV trace is observed is obtained from the potential which yields the maximum value of the first derivative of the IV trace The initial estimate of kT_e is obtained from the slope of a log plot of the electron retardation region of the IV trace Since in a retarding field the electron current to the probe is

$$I_e = I_{max} \exp\left(\frac{e(V - V_p)}{kT_e}\right) \tag{2 20}$$

$$\Rightarrow \ln I_e - \ln I_{max} = \frac{eV}{kT_e} - \frac{eV_p}{kT_e} \tag{2 21}$$

$$\Rightarrow \frac{d}{dV}(\ln I_e) = \frac{e}{kT} \tag{2 22}$$

therefore a plot of lnI_e versus V has a slope of e/kT_e the reciprocal of which gives T_e in electron volts After the initial estimate of the parameters of $\chi(V)$ is obtained, the most suitable value of r_p/λ_d is determined by fitting the experimentally measured probe current $I(\chi)$ to the theoretically predicted probe current

$I_e(\frac{r_p}{\lambda_d}, \chi)$ from Laframboise [42] For this fitting process $\chi(V)$ is taken at a large negative value so that there is no contribution from fast electrons to the current Calculation of the other plasma parameters are made following this first approximation of kT_e, V_p and r_p/λ_d [43] Equations 2 16 and 2 19 are used to find the electron density

$$n_e = \frac{I_e(\chi)}{er_p l \left(\frac{2\pi kT_e}{m_e}\right)^{\frac{1}{2}} f\left(\frac{r_p}{\lambda_d}, \chi\right)}, \quad \chi > 0 \tag{2 23}$$

where $I_e(\chi)$ is the current at some positive value of χ i e at some $V > V_p$ Similarly the ion density n_i is calculated using equations 2 18 and 2 15 which can be combined to give

$$n_i = \frac{I_+(\chi)}{er_p l \left(\frac{2\pi kT_e}{m_+}\right)^{\frac{1}{2}} f\left(\frac{r_p}{\lambda_d}, \chi\right)}, \quad \chi < 0 \tag{2 24}$$

with $I_+(\chi)$ measured at a sufficiently negative value to remove any contribution to the current from fast electrons Since the value of V_p as determined from the maximum of the first derivative is always found to be lower than the saturation point the alternative method of intersecting slopes can be employed, in this method the plasma potential is determined to be the point of intersection of the extrapolated exponential region and the saturation region and is evaluated as follows

$$V_p = V_{max\ deriv} + kT_e \ln\left(\frac{I_{sat}}{I_{max\ deriv}}\right) \tag{2 25}$$

where $V_{max\ deriv}$ and $I_{max\ deriv}$ are the voltage and current at the maximum of the first derivative and I_{sat} is the electron saturation current The value of V_p is corrected from its initial value using the value of I_{e0} from equation 2 19 using the new value of n_e from equation 2 23

2.5 The Magnetic Field Probe

In an inductively coupled plasma source RF power is coupled to the plasma by electron interaction with the induced electric field This induced electric field is non propagating and penetrates over a characteristic distance δ known as the *plasma skin depth* In order to understand the precise nature of this interaction, under various operating conditions, it is necessary to measure the spatially resolved electric field strength and induced current density Since the current flowing in the induction coil generates the time varying magnetic field which induces the electric field then the most straight forward way of determining the electric field is to measure the strength of the magnetic field components and their spatial derivatives from which the electric field and current density can be determined by Maxwell's equations This can be done by magnetic field or B-dot probes, the B-dot (B) actually measures the time derivative of the magnetic field strength which is directly proportional to the actual field strength when generated by a sinusoidal RF current

The voltage induced on a conducting loop placed in a time varying magnetic field is given by $V = -d\Phi/dt$ where Φ is the magnetic flux through the loop, from this the amplitude of the time derivative of the magnetic field can be calculated from $B= -VA$, where A is the area of the conducting loop The time dependent magnetic field has the form $B_\theta \exp \jmath(\omega t + \phi)$ so $B = \frac{B}{\jmath\omega}$

The electric field is calculated from Faraday's law,

$$\oint_c E\, dl = -\int_s B\ dS \tag{2 26}$$

where dl is the element of the loop and dS that of a closed surface By

assuming cylindrical symmetry and choosing the path C to be that of a circular loop bounding a circular area S at fixed axial positions, the electric field amplitude E_θ is given by

$$E_\theta(r) = -\frac{1}{r}\int_0^r r' \, B_z\,(r')dr' \tag{2 27}$$

where r and r' are radial positions as measured from the axis of the antenna From Ampere's Law

$$\nabla \times \mathbf{B} = \mu_0 J + \mu_0 \varepsilon_0 \frac{\partial \mathbf{E}}{\partial t} \tag{2 28}$$

Therefore if the spatial profiles of the amplitude and phase of B are measured then the spatial profiles of E_θ, J_θ and the absorbed power given by

$$P(r) = E_\theta(r) J_\theta(r) cos\phi_{EJ} \tag{2 29}$$

where ϕ_{EJ} is the phase difference between E_θ and J_θ, can be determined Furthermore the local permittivity ε can be calculated form

$$\varepsilon = \varepsilon_0 \left(1 - \frac{\omega_p^2}{\omega(\omega - j\nu)}\right) \tag{2 30}$$

This information coupled with precise spatially resolved Langmuir probe measurements of the electron density n_e allow the existence and extent of collisionless heating to be determined Also using this information the presence of warm plasma effects can be investigated Alternatively, the technique can be used to build a database of effective collision frequencies, which would allow B-dot probe measurements to determine the electron density directly

2.5.1 Design of the B-dot probe

Conventional B-dot probes take the from of a wire loop enclosed in a glass tube

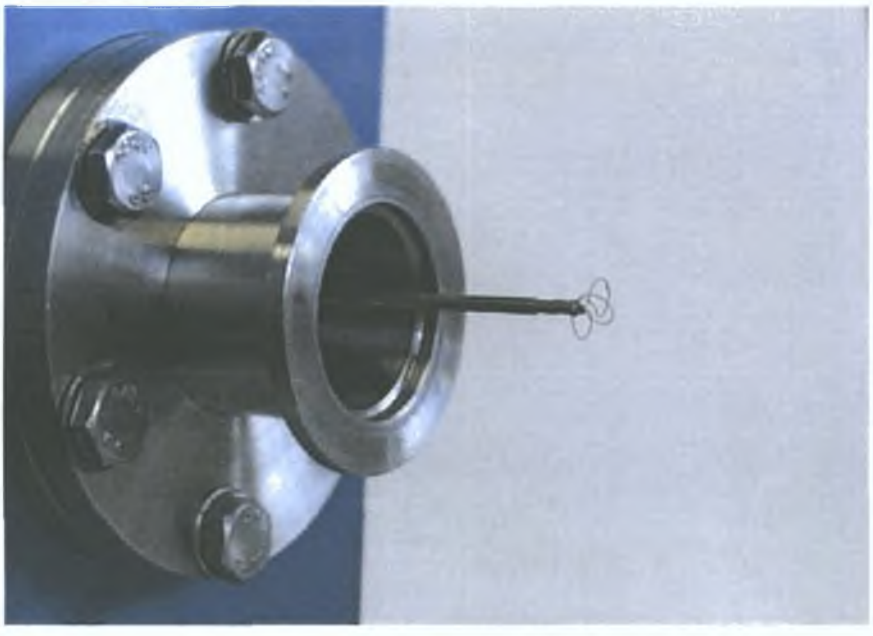

Figure 2.7: *Photograph of B-dot probe*

or other dielectric envelope. While this method may simplify construction and prolong the life of the probe the validity of the measurements has been called into question due to perturbations of current flow and symmetry near the probe [44]. An alternative to the enclosed probe is a design based on using a thin wire probe without an insulating shell, with such a probe the perturbation is negligible, but this design gives rise to a number of potential problems which must be overcome before reliable $\dot{B}$ probe data can be obtained.

The most significant problem is due to the large RF plasma potential relative to ground caused by capacitive coupling between the induction coil and the plasma. This results in stray capacitive coupling between the probe and the plasma which causes common mode RF interference on the $\dot{\mathrm{B}}$ probe. It is essential that this common mode noise is reduced to a minimum. This is achieved in two ways, firstly by encasing the probe shaft in a grounded copper tube which

acts as an electrostatic shield and secondly the probe wires are terminated to a centre-tapped balun (balanced-unbalance) transformer The balun transformer is constructed using a small binocular ferrite core around which the ends of the probe wire are wound to make the primary winding Around this primary winding is placed a strip of copper foil This copper foil shields the primary from the secondary winding The secondary winding consists of 5 or 6 turns of copper magnet wire which is grounded in the centre The ends of the secondary are fed to the scope The number of turns to use in the secondary was determined by trial and error to give the largest possible signal at the scope

This transformer acts to both reduce common mode noise and also to amplify the B signal The signal from the loops is fed to a fast oscilloscope (HP6000) The current flowing in the probe is minimised by terminating the probe to an impedance much larger than the probe resistance This has the effect of limiting any disturbance of the plasma which may be caused by a current flowing in the probe With this arrangement a large dynamic range (60 dB) is achieved

The probe constructed for the experiment follows closely the design of Piejak et al [45] This two dimensional probe, shown in figure 2 7, consists of two molybdenum wire loops co-located at the end of a copper shielded ceramic tube The single turn loop determines the $B_z(r)$ component of the magnetic field while the double loop in the shape of a figure of eight is such that the voltage induced in each half of the loop subtract resulting in a signal proportional to the spatial derivative in the z direction (dB_r/dz) The loop diameters are 3 mm and the wire diameter is 2 mm It is important in B probe design that the loop be as small as possible in order to minimise convolution effects and optimise the spatial

resolution of the measurements [44] The probe is mounted on a two dimensional, computer controlled, scanning bellows This system allows spatial resolution to a precession of 2 mm

2.5.2 Calibration of the B probe

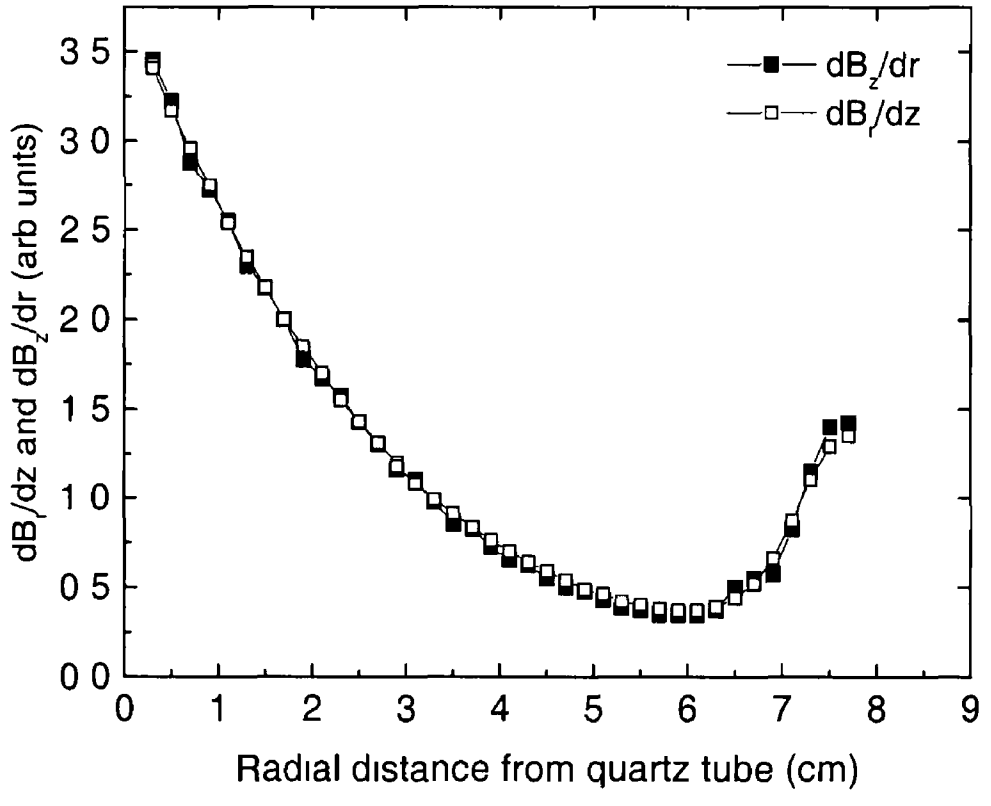

Figure 2 8 *B-dot probe measurement in vacuum The open squares curve is the dBr/dz(r) signal provided directly by the differential probe while the solid squares curve is the spatial derivative of the single loop signal (Bz(r))*

The B_z probe is calibrated in a solenoid with a known RF current, and by using a Poisson code to calculate the central field of this solenoid In vacuum $\nabla \times \mathbf{B} = 0$ and in this cylindrical geometry $\nabla \times \mathbf{B} = dB_z/dr - dB_r/dz$ Hence the

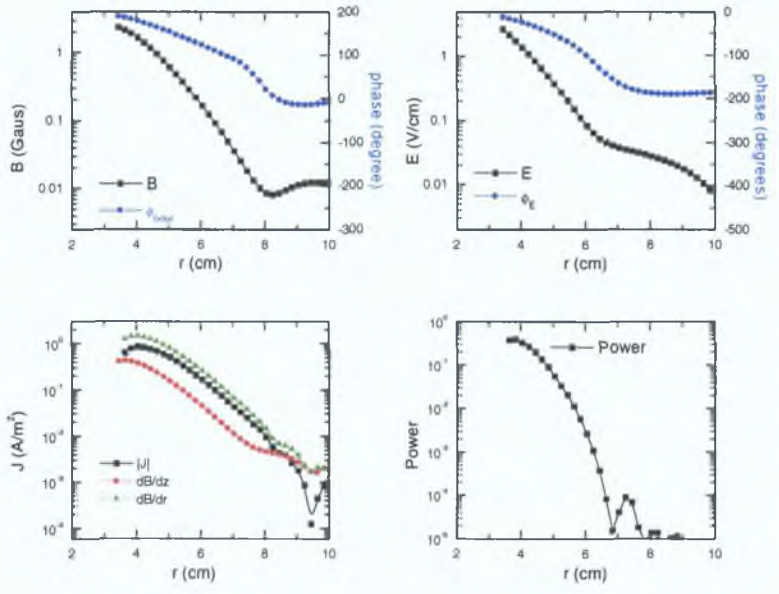

Figure 2.9: B *probe measurement in argon.*

differential probe is calibrated by equating the components dB_r/dz and dB_z/dr when measured in vacuum. The signal is captured on the fast oscilloscope and downloaded to a PC using an IEEE interface. It is assumed that the signal is composed only of the fundamental harmonic. The Levenberg-Marquardt non-linear fitting routine was used in a computer program to determine the amplitude and phase of the components. The integration and differentiation required to determine the E_θ and J_θ is performed by another program in terms of the real and imaginary parts of the magnetic field. The phase in all cases is measured with respect to the phase of the electric field in vacuum. The probe is checked for capacitive coupling and common mode signal interference by rotating the probe through 360^{O} and observing the ratio of the maximum to the minimum signals. Probe test measurements in vacuum are shown in figure 2.8 where the open squares curve is the $dB_r/dz(r)$ signal which is provided directly by the

differential probe and the solid squares curve is the spatial derivative of the single loop signal ($B_z(r)$) It is shown here that both components are equal to within 10% which indicates a zero current in vacuum, this method was used to calibrate the differential probe on an absolute scale A typical set of the B probe results are shown in figure 2 9 the results are shown for input power of 100 W and the pressure is 100 mTorr

Chapter 3

Heating Mechanisms

3.0.3 Introduction

Power coupling in an inductively coupled plasma is achieved via electron interaction with evanescent electromagnetic waves at the surface of the plasma The electromagnetic wave is non-propagating if its frequency ω is less than the plasma electron frequency ω_{pe} This condition is fulfilled in low temperature, inductively coupled plasmas operating at 13 56 MHz for densities greater than 10^6 cm^{-3} Such a wave is damped as it penetrates the plasma The phenomenon of wave damping at the surface of conductors is called the skin effect and it has an associated characteristic wave penetration depth called the skin depth (δ) The skin depth is determined differently depending on whether the plasma is collisional ($\nu \ll \omega$), collisionless ($\nu \gg \omega$) or anomalous ($v_{\rm th}/\delta \gg \omega, \nu$) [46] While the skin effect is well known in relation to conduction in metals [47] plasmas are ideal for studying the phenomenon since, unlike in a metal, probes can perform spatially resolved measurements in a plasma

3.0 4 Theory

In an ICP the amplitude of the electromagnetic wave decreases rapidly (by an order of magnitude in the first few centimetres) as it penetrates the plasma volume, then it follows that electron interaction with the wave which can result in the electron heating, necessary to sustain a steady state plasma, takes place within the skin layer Knowledge of the heating mechanisms in ICPs is important in the design of ICP sources and there are several mechanisms to be considered Depending on the operating pressure the plasma can be described as either collisionless (if the mean free path of an electron λ is greater than the plasma size L) or collisional if $\lambda < L$ In a *cold (i e where the electron thermal motion is negligible)* collisionless plasma, the electron samples the electromagnetic field at a single location in space, and since the field has a harmonic time variation, the time-averaged value of the electric field is zero In such circumstances the phase difference between the rf current J and the electric field is 90^0 and no energy can be transferred form the field to the electron since any energy gained by the electron during one half of the rf cycle is returned back to the field in the other half of the cycle

For power absorption to occur there must be some randomisation mechanisms that break the regularity of the electron motion and alters the 90^0 phase difference between the rf induced electric field E and the rf current density J At high enough pressure, the required phase randomisation mechanism is due to collisions with the neutral background gas, which leads to Ohmic heating When Ohmic heating dominates over other possible power absorption mechanisms, the thermal motion of electrons can be neglected, and in this collisional plasma the coupling between

the RF current density J and the RF induced electric field E is local and given at any position by

$$j = \sigma E, \tag{3 1}$$

where σ is the complex conductivity of the *cold* plasma given by,

$$\sigma_{\text{cold}} = \frac{n_e e^2}{m_e(\nu_e + j\omega)} \tag{3 2}$$

where n_e is the electron density, ν_e is the electron collision frequency, m_e is the electron mass and ω is the driving frequency

It was shown by Lister *et al* [48] that collisions plays an important role both in the real and imaginary parts of σ In real plasmas where the Electron Energy Distribution Functions (EEDF's) are generally non-Maxwellian and where the electron collision frequency ν depends on the electron energy ε (particularly in rare gases with a marked Ramsauer minimum), collisions must be taken into account when calculating the real and imaginary part of the plasma impedance It is convenient to express the conductivity σ in a way analogous to the classical expression for conductivity in a high frequency plasma, [48],

$$\sigma = \frac{e^2 n_e}{m_e\left(\nu_{rf} + j\omega_{eff}\right)}, \tag{3 3}$$

where n_e is the electron density, ω_{eff} is an effective RF frequency that takes into account the effect of collisions on the plasma reactance ($\omega_{eff} \approx \omega_{rf}$ at low pressure) and ν_{rf} the electron neutral collision frequency in the RF field Both ω_{eff} and ν_{rf} depend on the differential collision frequency for electron momentum transfer $\nu_c(\varepsilon)$ and on ω

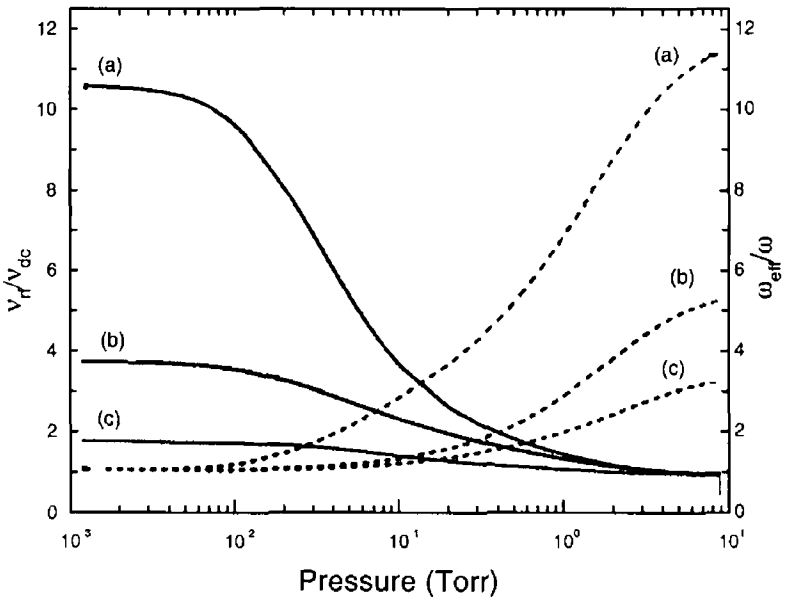

Figure 3 1 *Data from* [48] *showing comparison of* ν_{rf}/ν_{dc} *(solid lines) and* ω_{eff}/ω *(dashed lines) for three different forms of the EEDF (a)bi-Maxwellian (b) Maxwellian and (c) Druyvesteyn*

The dependence of the real and imaginary parts of the electrical conductivity on collisions and the form of the electron energy distribution function is illustrated in figure 3 1 [48] which shows computed values of the parameters ν_{rf}/ν_{dc} and ω_{eff}/ω as a function of pressure for three different forms of the electron energy distribution function It is convenient to use the normalised quantity ν_{rf}/ν_{dc} where ν_{dc} is the dc limit of the electron collision frequency The results are determined for an argon plasma at a driving frequency of 13 56 MHz with an effective electron temperature of T_{eff}=1 eV The data is presented for (a) a bi-Maxwellian, (b) a Maxwellian and (c) a Druyvesteyn EEDF The forms of these EEDF's are shown in figure 3 2 In figure 3 1 the effect of the Ramsauer

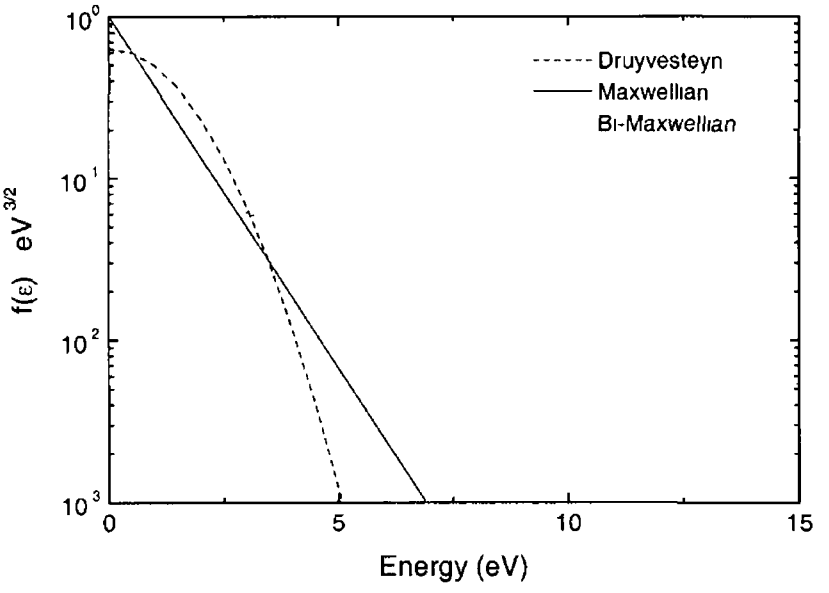

Figure 3 2 *Examples of 3 different forms of the EEDF for* $T_{eff} = 1$ eV

minimum is evident when one compares the bi-Maxwellian distribution with its' enhanced high energy tail to the Druyvesteyn distribution with its' depleted high energy tail, at low pressure these features lead to a difference of the order of 5 in their respective values of ν_{rf}

The collisional electrical conductivity σ of equation 3 3 will be used in the following to determine the Joule heating component in the power balance and is valid in the *cold* plasma approximation In this situation, the skin effect is said to be normal and is characterised by a monotonic decay of the electromagnetic wave inside the plasma volume

However, for the range of pressures that are of interest for practical applications, the mean free path λ of the electrons is often larger than the plasma chamber, in this case ohmic heating becomes negligible, and most of the power must be absorbed by a collisionless heating mechanism It is well known that

collisionless stochastic heating plays a major role in sustaining rf capacitive discharges In capacitive discharges stochastic heating occurs when electrons interact with the modulated rf sheath at the plasma-wall boundary [49, 50] In inductive discharges there is always some power deposited in the plasma by capacitive coupling but at pressures where the plasma is considered collisionless $<$ 10 mTorr the contribution of capacitively coupled power to the total power deposition has been found to be less than 1 % [51] therefore there must exist another collisionless power coupling mechanism which is effective in low pressure ICPs The precise details of this mechanism are not fully understood However, it is believed that the randomisation mechanism is due to the finite value of the electron thermal velocity If electron-neutral collisions are rare then the cold plasma approximation ceases to hold The electrons in thermal motion sample the field along some trajectory, hence net heating can occur [22] since, in general, the spatially inhomogeneous field does not average to zero along a trajectory In particular, since the electric field is confined to a skin depth, if an electron has a thermal velocity v_{th} that is high enough to traverse the skin depth in a time that is short ($\approx 10^{-8}$ s in this system) compared to the period of the field and the collision frequency ($v_{\rm th}/\delta \gg \omega, \nu_{en}$), then it may gain net energy from the field

Furthermore, Rauf et al [8] using the results of a self-consistent analytical model proposed that the collisionless heating process relies on a resonant interaction of the electrons with the electromagnetic wave There is always some resonant interaction between electrons travelling with a velocity approximately equal to the wave phase velocity (Cherenkov resonance), since in a Maxwellian distribution there is always some electrons with that velocity However the effect

is most pronounced if the average electron thermal velocity is comparable to the wave phase velocity since in this case the number of electrons which strongly interact with the electromagnetic field is at a maximum Experimentally we can determine if this condition is fulfilled by calculating $\omega(d\phi/dr)^{-1}$ and comparing this to v_{th} as calculated from measurements of T_e

Also, the finite size of the plasma chamber has some important consequences on collisionless electron heating [23] for several reasons Indeed, at low pressure, the electron mean free path λ can become longer than the plasma characteristic lengths δ and L where L is the plasma size In the collisionless limit where $\lambda \gg L$ the electrons interact repetitively with the skin layer (after specular reflection at the plasma sheath boundary at the outer wall) with a bounce frequency $\Omega = \pi v_\perp/2L$ where $v_\perp$ is the electron velocity perpendicular to the plasma boundaries (and thus to the E field) In this case the finite size and shape of the plasma is crucial for the electron dynamics and stochastic heating and leads to transit time resonance (phase correlation between subsequent interactions with the field) when the bounce frequency Ω of the electrons becomes proportional to integer numbers k of the rf driving frequency [23, 52, 53, 54] $\Omega \approx 2\pi k\omega$ Kaganovich *et al* [23] classified different heating regimes depending on the relative value of Ω, λ and δ, including a hybrid heating regime when $L > \lambda > \delta$ where the successive interactions with the field within the skin layer are due to collisions with neutrals in the region $\delta < x < L$ rather than with a reflection from the sheath potential at the walls

Finally, recent progress in the theory of collisionless heating includes non-linear effects and indicates a difference, which is at present unclear, from the

linear theory previously used for calculating the collisionless power dissipation [25] The non linear effects occur because the rf magnetic field transforms the parallel (to plasma boundary) velocity kicks of the E field into a perpendicular velocity kick [55] In this case Ω depends on the electron velocity perpendicular to the boundary and Ω changes after each interaction with the skin layer, moving the electrons out of the resonance region

Whatever the exact mechanism is, collisionless power absorption is a *warm plasma effect* [22, 8], and a direct consequence of the electron thermal motion is that an electric field applied to one part of the plasma can affect the current elsewhere in the plasma, so that the classical expression for the plasma conductivity $J = \sigma E$ must be replaced by [56]

$$j = \int_r \sum(r) E(r) dr, \tag{3 4}$$

where $\Sigma(r)$ is a distributed conductivity This phenomenon of RF current diffusion due to spatial dispersion of the conductivity that results from the electron thermal motion is responsible for the so-called anomalous skin effect

The RF field penetration in the anomalous skin effect regime was first calculated by Pippard [47] for metals at low temperatures and by Weibel [57] for a homogeneous plasma The main characteristics of the spatial distribution of the electromagnetic field in the plasma volume in the anomalous skin effect regime are a non-monotonic decay and the appearance of local maxima and minima in the fields, as observed by Demirkhanov [58], Joye and Schneider[59] and Piejak *et al* [30]

3 0.5 Motivation

The recent technological applications of ICPs for microelectronic device fabrication and lighting applications has triggered a considerable amount of work on the anomalous skin effect and collisionless power absorption in ICPs in the last 10 years, especially with theoretical and modeling approaches [22, 23, 24, 25, 10, 26, 24, 27, 28, 29] Liebermann and Godyak [14] and Kolobov and Economou [24] give a complete historical review of those papers Consequently, collisionless electron heating is now widely accepted However, experimental evidence for this phenomenon is particularly difficult to obtain In fact, most workers have focussed on the anomalous skin effect (first observed more than 30 years ago and attributed to electron thermal motion [58]) that underlies collisionless heating of electrons It seems that the only real quantitative evidence of such heating mechanism in an ICP was reported recently by Godyak *et al* [9] By developing a two-dimensional immersed B-dot probe [30], they were able to deduce the spatial distributions of the rf electric field E and current density J , and thus the distribution of the power density absorbed by the plasma electrons along the discharge axis, z

$$P_{exp}(z) = J(z)E(z)\cos(\Psi(z)), \tag{3 5}$$

where Ψ is the phase difference between E and J The collisional and collisionless parts of the total absorbed power, $P_{\rm exp}$, were then separated by calculating the collisional power density absorbed in the discharge $P_{\rm col}$, by using the measured distributions of E and J , but assuming a constant collisional power absorption

corresponding to the cold plasma approximation

$$P_{col}(z) = J(z)E(z)cos\Psi_{col}, \tag{3 6}$$

where Ψ_{col} is the phase shift between E and J deduced from the conductivity of a cold plasma

$$\cos\Psi_{col} = \left(1 + \omega_{eff}^2/\nu_{en}^2\right)^{-\frac{1}{2}} \tag{3 7}$$

However, ν_{en} depends both on ω and on the shape of the EEDF hence ω_{eff} and ν_{en} must be deduced by comparing the conductivity of the cold plasma (equation 3 2 with the general form given by kinetic theory[48]

$$\sigma = -\frac{2e^2 n_e}{3m}\int_0^\infty \frac{\varepsilon^{3/2}}{\nu_c(\varepsilon) + j\omega}\frac{df(\varepsilon)}{d\varepsilon}d\varepsilon, \tag{3 8}$$

where n_e is the electron density, $f(\varepsilon)$ is the EEDF, $\nu_c(\varepsilon) = Nv\sigma_c(\varepsilon)$ is the differential collision frequency for electron momentum transfer at energy ε, N the neutral gas density, $v = \sqrt{2\varepsilon/m}$ the electron most probable velocity and σ_c the effective collision cross section for momentum transfer

It is thus necessary to know precisely $\sigma_c(\varepsilon)$ and to measure the EEDF accurately in order to calculate the collisional power absorption $P_{col}(r)$ and to compare this result with the total power absorption $P_{exp}(r)$ measured in the experiment By carefully performing those measurements, Godyak *et al* [9] demonstrated for the first time that collisionless stochastic heating dominates Ohmic heating for pressures below 10 mTorr, in good agreement with the prediction of Turner [22]

In this thesis the same approach as Godyak *et al* has been used to investigate the electron dynamics and electrodynamics in an inductive discharge operating with a re-entrant geometry As a consequence of this geometry, the electromagnetic field components were measured as a function of the discharge radius, so

that the spatial position z must be replaced by r in equations 3 5 and 3 6 This geometry is different from that used by Godyak et al (a planar coil) and is of interest for lighting applications [14] and negative ion sources [60] The results have been systematically compared with those from reference [9], showing good agreement despite the different geometry and diagnostics (Langmuir and B probes) used to measure the spatial distributions of the plasma internal parameters

In section 3 2, the anomalous skin effect observed in the experiment will be discussed in detail A quantitative comparison of the collisional and collisionless parts of the power absorption is made by comparing the effective electron neutral collision frequency measured in the experiment with the electron neutral collision frequency deduced from the Langmuir probe measurements

3.1 Experiments

To investigate the discharge heating mechanisms, a number of diagnostics have been used They include a I/V probe (Scientific Systems) located at the output of the matching unit and providing a measurement of the rms values of the antenna voltage V and current i In principle the I/V probe is capable of measuring the current voltage and phase difference between them form these quantities, the power absorbed in the plasma can be determined Unfortunately, for these experiments only a test version of the instrument was available, in this version, while the current and voltage was measured precisely the error on the phase was relatively large For this reason the power dissipated in the plasma was directly measured with a directional RF power meter which is described in section 2 2 1

which monitors the forward and reflected power going through the antenna, P_{in} and P_{ref}, respectively The power dissipated in the antenna coil was estimated by measuring the antenna resistance in vacuum $R_a=(P_{in}-P_{ref})/i^2=0$ 36 Ω, and the real power absorbed by the plasma electrons and ions was then deduced as

$$P_{abs} = (P_{in} - P_{ref}) - R_a i^2 \quad (3\ 9)$$

The typical power used in the following experiments are 100, 200 and 300 Watts (indicated in the front panel of the generator), corresponding respectively to 42, 140 and 230 watts of real power absorbed by the plasma electrons and ions, the difference being dissipated in heating the antenna

The Langmuir probe system (Scientific Systems Smartprobe) which is described in detail in section 2 4 was used to measure the EEDF and the corresponding plasma density and electron temperature, the probe being housed in a linear bellows in order to record radial profiles (in the middle of the antenna) of those quantities with a spatial resolution of 2 mm Due to the low operating pressure in these experiments and to systematic cleaning of the probe tip (a dc voltage of 100 V is automatically applied to the probe tip for 0 5 s before each measurement), the electron density deduced from the EEDF and the ion density obtained from the ion saturation region of the probe characteristic never differ by more than 30 % in the experiments described below

The axial and radial components of the magnetic flux, dB_z/dt and dB_r/dt respectively are measured using the B probe described in section 2 5

Using these measurements, it is possible to determine the penetration of the azimuthal electric field $E_\theta(r)$ and that of the current density $J(r)$ through the

plasma from Maxwell's equations in a cylindrical geometry

$$E_\theta(r) = -10^{-8}\frac{i\omega}{r}\int_0^r r' B_z(r')dr', \tag{3 10}$$

$$J_\theta(r) = \frac{10}{4\pi}\left(\frac{dB_r}{dz} - \frac{dB_z}{dr}\right), \tag{3 11}$$

where r, z are in cm, B in Gauss, E in $V\,\mathrm{cm}^{-1}$ and J in A cm^{-2} in order to apply equation 3 10, it is necessary to perform an integral between $r = 0$ and $r < R_2$ (outer wall), although the B data are only known between $r = R_1$ (quartz tube) and $r = R_2$ For this reason, the assumption than the emf is negligible at the outer conducting wall was made, so that the boundary condition $E = 0$ holds at $r = R_2$ Measurements performed in the system show that this assumption is reasonable The spatial distribution of $E_\theta(r)$ was then deduced from the raw data as

$$E_\theta(r) = -10^{-8}\frac{j\omega}{r}\left[\int_{R_1}^r r' B_z(r')dr' - \int_{R_1}^{R_2} r' B_z(r')dr'\right] \tag{3 12}$$

Since B probe data are in polar form (amplitude and phase relative to electric field in vacuum) [61], and it is necessary to transform them into real and imaginary parts to perform the spatial integration and differentiation leading to E and J In the following, the data were then transformed back in polar co-ordinates for display

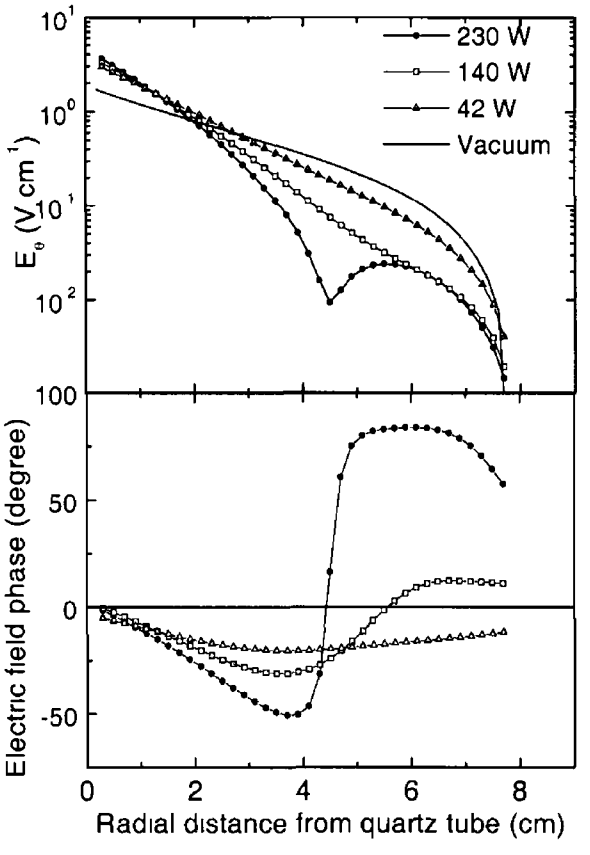

Figure 3 3 *The induced electric field amplitude (upper curves) and phase (relative to the electric field phase in vacuum) at 5 mTorr for 3 different rf powers as a function of the distance from the quartz tube surrounding the antenna The solid line curve is a measurement in vacuum and shows the influence of the reactor geometry on the electric field distribution The non-monotonic decrease in the field amplitude and the phase reversal observed at high power are typical of the anomalous skin effect*

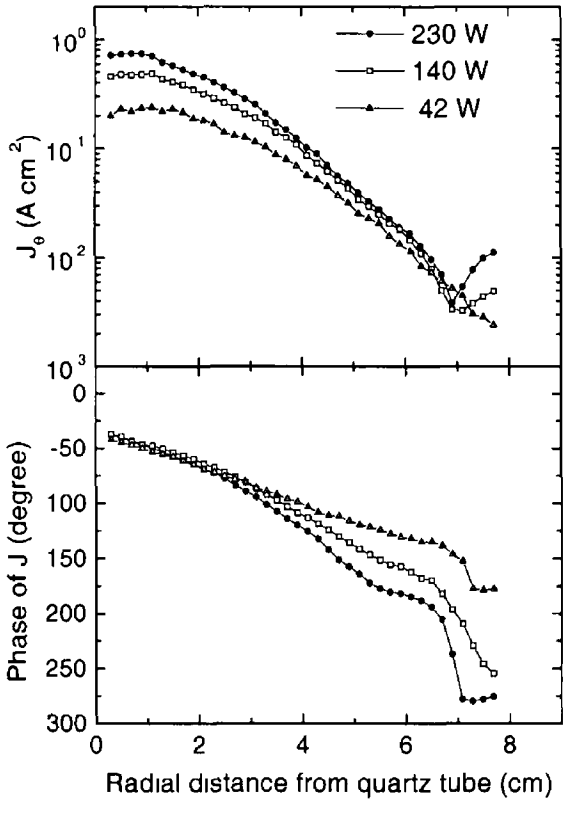

Figure 3 4 *The rf current density amplitude and phase distribution for the same conditions as in figure 3 3 It shows the appearance of a second layer of rf current circulating near the walls (in the opposite direction with the current circulating in the skin layer) which amplitude increases with rf power*

3.2 Results

3.2 1 The anomalous skin effect

The radial distribution of the induced azimuthal electric field E_θ and current density J_θ deduced from equations 3 10 and 3 11, together with the corresponding phase distributions are shown in figure 3 3 and figure 3 4 The data presented here is for three different power settings at a pressure of 5 mTorr, the electric field measured in vacuum is also shown in figure 3 3

The measurements in vacuum show the rf electric field decays approximately exponentially as a function of distance from the quartz tube for most of the chamber radius with a with a characteristic decay length of 2 4 cm, before dropping sharply near the conducting chamber walls The magnetic field measurements in vacuum were found to be in good agreement with the results obtained from a computer program used to model the magnetic fields of solenoids The sharp drop in the profile at r=7 cm is due to rf current flowing in the conducting chamber walls The field distribution in the chamber is thus greatly affected by the coil and chamber geometry as in most ICPs of practical interest

When a discharge is present, the electric field decays faster due to the exchange of energy with the plasma electrons The field amplitude decay is first exponential and the field is confined to a plasma skin depth $\delta \approx 1\ 15$ cm, while the electric field phase decreases linearly as expected from classical theory of the normal skin effect However, beyond the skin layer the non-monotonic distributions observed at 230 W in figure 3 4 exhibit some typical features of the anomalous skin effect Here, the field decays faster than a single exponential, and after reaching a local

minimum at $r = 4.3$ cm it start to increase again before dropping near the metal walls. Where the electric field is at its first minimum, the phase reverses and begins to increase after passing through the minimum. This behaviour is typical of the anomalous skin effect and the results of figure 3.4 are very similar to those of reference [30] and in qualitative agreement with the analytical results of Kolobov and Economou [24]. The latter proposed that the field structure is generated by two components of the plasma currents, one due to a group of effective electrons that spend a long time in the skin layer (and which are responsible for the fast field damping in δ) and another group of ineffective electrons that leave the skin layer too quickly to be strongly affected by E (and these electrons damp the electric field as r^{-2}). This kind of distribution is also similar to the magnetic field distribution measured by Dermirkhanov *et al* [58]. They interpreted the field distribution as a result of the electron thermal motion that transfers ballistically some rf current from the skin layer deeper into the plasma. As pointed out by Godyak *et al* [62], the appearance of local maxima and minima in the rf induced field distribution can be explained as the superposition of the field induced by the coil with that induced by the plasma current inside the skin layer and those transferred outside from the skin layer by the electron thermal motion. Indeed, when one compares the current density profile in figure 3.4 with the electric field profile in figure 3.3, one can see that the current decays more slowly than the electric field (far outside the skin depth, at $r = 4.5$ *cm*, J is only 1/10 of its maximum value whereas the value of E decreases to much less than 1/100 of its maximum value) and that a second layer of rf current circulates near the wall, explaining the local maxima of the fields (induced by those currents). The amplitude of this second layer

increases dramatically with the rf power (at $r = 7\,cm$) and the local maximum in the rf electric field appears Finally, the current circulating near the walls is in the opposite direction to the current circulating inside the skin depth, here the the electric field is slowing the current rather than driving it

The appearance of the second current layer is a direct consequence of the spatial dispersion of the conductivity due to non-local electrodynamics at low pressure the rf current currents circulating near the walls are not induced by the electric field there, but diffuse from the skin layer, i e are generated by electrons that carry away (due to their thermal motion) some momentum gained in the skin layer, generating a rf current on their way Indeed, as mentioned previously, another essential feature of the anomalous skin effect is that the penetration length of the electric field and that of the current density are different This can be seen more clearly in figure 3 5 and figure 3 6 where the amplitude and phase distribution of E and J are plotted on the same graph for 5 mTorr 300 W and 10 mTorr 300 W plasmas, respectively The less rapid decay of current density (and magnetic field) is explained by the transport of RF current from the skin layer due to thermal electron motion, as expected from the warm plasma theory Indeed, it obvious from figure 3 5 and 3 6 that there is significant dispersion of the plasma conductivity under these conditions

Finally, these different mechanisms for the propagation of the electromagnetic field and rf current density lead to a significantly different phase distribution of E and J the current phase is linked to the electron mean velocity, whereas the electric field phase is defined by the wave phase velocity that depends on the plasma density This leads to a variety of patterns in the phase distribution

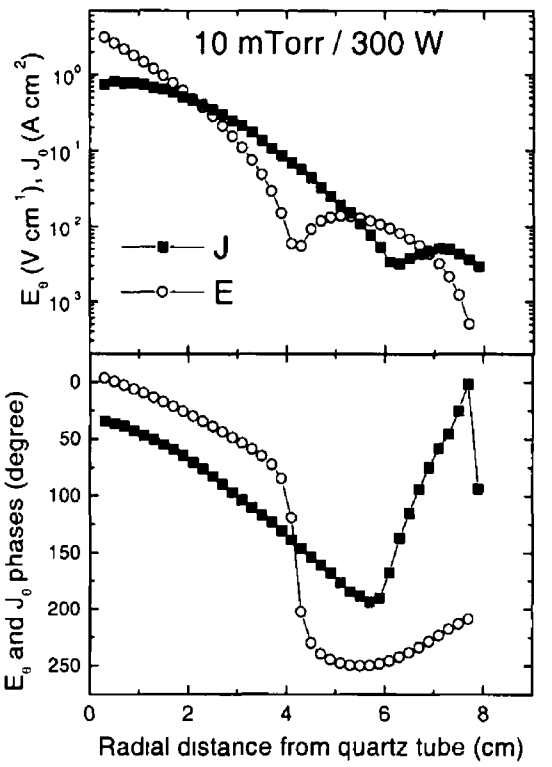

Figure 3 5 *The amplitude and phase of E and J are plotted together for a 10 mTorr 230 W plasma The spatial dispersion of the conductivity is characterised by a less rapid decay of J the rf current density is translated from the skin layer by the electron thermal motion The E and J field phases exhibit a phase bifurcation by comparison with the 5 mTorr result (see figure 3 6)*

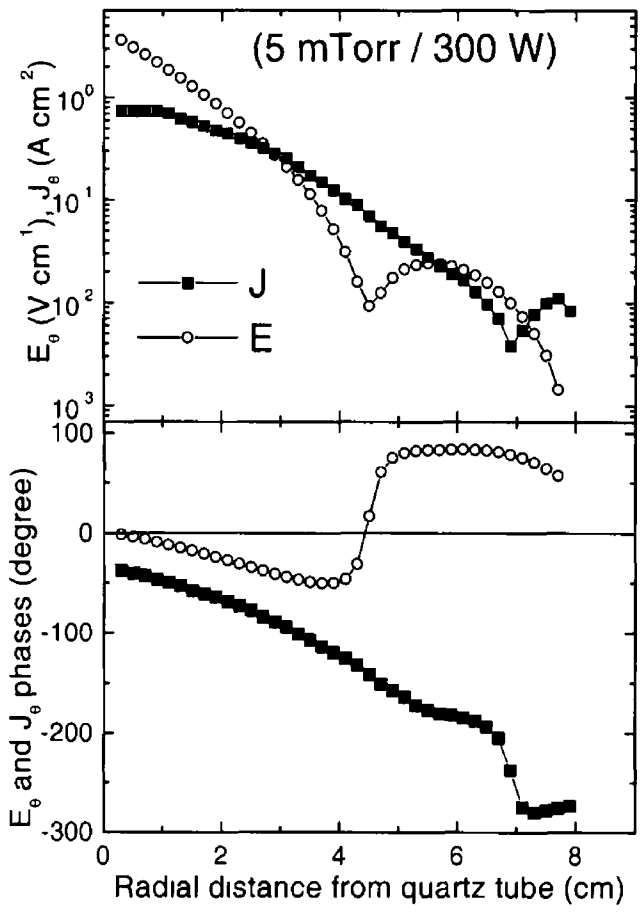

Figure 3 6 *The amplitude and phase of E and J (extracted from figures 3 4 and 3 3) are plotted together for a 5 mTorr 230 W plasma for comparison with figure 3 5 at 10 mTorr*

of E and J For example, by comparing figure 3 5 and figure 3 6 one can see that, although the field and current density amplitude distribution exhibit a similar shape at 5 and 10 mTorr, the corresponding phase distributions are on the contrary different and show a phase bifurcation The E field phase that is seen to reverse (increasing again) at $r \approx 4\ 5$ cm at 5 mTorr is, in contrast, dropping sharply by 190° at 10 mTorr This phenomenon occurs because the electron density rises from $1\ 3 \times 10^{11}$ cm^{-3} to 2×10^{11} cm^{-3} when the pressure is increased from 5 to 10 mTorr, thereby decreasing the wave phase velocity v_ϕ at 5 mTorr the relation $v_{\text{th}} < v_{phi}$ holds at any position, but at 10 mTorr, v_ϕ becomes equal to v_{th} at $r = 3\ 7$ cm At this point of resonant density, the electrons undergo a strong interaction with the field [8, 63] and collisionless effects due to the electron thermal motion result in the phase bifurcation

As described above, and in contrast to a cold plasma where the phase distribution of E and J should vary almost linearly, several kinds of patterns appear in the phase distribution of a warm plasma leading to some unusual phenomena such as negative power absorption [63] For a cold plasma, the phase difference between E and J would be almost constant and given by $\Delta\Psi = \Psi_E - \Psi_J = \arctan(\omega_{eff}/\nu_{rf})$, $\Delta\Psi$ should always be less than 90, such that the power absorbed $P = EJcos(\Delta\Psi)$ is always positive However, in this experiment, $\Delta\Psi$ is clearly more than 90 at some radial positions indicating the presence of negative power absorption Figure 3 7 shows the distribution of the RF power density absorbed along the radial direction for a 42 W and 230 W, 5 mTorr plasma As expected, most of the power is absorbed in the skin layer near the quartz tube surrounding the antenna However, outside the skin layer, the power absorbed oscillates and becomes negative

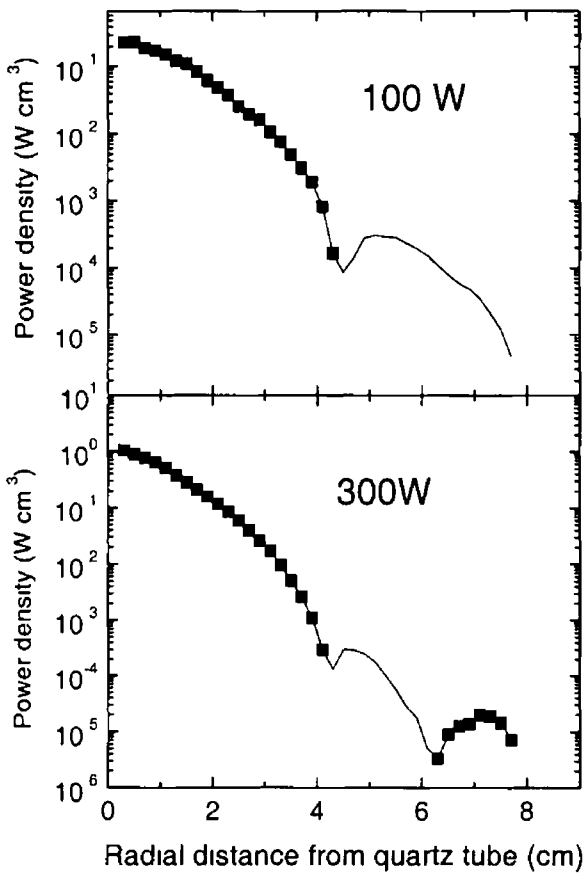

Figure 3 7 *The power density P_{exp} absorbed by the plasma as a function of radial position for a 5 mTorr 100 W and 300 W plasma (corresponding to figure 3 4 and 3 3 The square symbols indicate the real data (i e positive power absorption on a log scale), although the line curve is the absolute value of P_{exp} and indicates some regions of negative power absorption where the electrons return some energy to the electromagnetic field Depending on the plasma conditions the power can oscillate and present several positive region separated by negative power absorption regions*

for radial distances between 4 and 6 7 cm before becoming positive again The power absorbed becomes negative when the current transferred from the skin layer by the electron thermal motion flows against the local electric field At this point, the electrons begin to return a part of the energy they acquired in the skin layer back to the RF field (deceleration) This is characteristic of the anomalous skin effect where E and J become independent to some extent, as a consequence of the spatial dispersion of the conductivity It is particularly interesting to see the similarity of these results from figures 3 4-3 7 to that of the experimental work of Piejak *et al* [30] and Godyak *et al* [64], and with the analytical calculation of RF power absorption of Kolobov [65] This is somewhat surprising, since the chamber geometry is completely different, leading to a different electric field distribution, but this demonstrates that similar effects due to collisionless heating occur in different types of ICP

3.2 2 Collisionless heating mechanism

In this section a quantitative treatment of the collisional and collisionless contribution of the plasma electrons to this conductivity is presented This is done by comparing the total power measured in the experiment with the collisional power dissipated in Ohmic heating This is a complicated procedure, since the collisional power dissipation is characterised by the conductivity of a cold plasma (3 3) that is to say by the electron-neutral transport collision frequency in the rf field, ν_{en}, a parameter that is particularly difficult to measure in rf discharges operating in rare gases Not only must the EEDF be known to deduce ν_{en} (equation 3 3 and 3 8) but also the neutral gas temperature must be measured to properly

evaluate the neutral atom density [9] at a given pressure (needed to calculate ν_c in equation 3 8) Unfortunately, measuring precisely the neutral gas temperature requires sophisticated laser absorption (or Laser Induced Fluorescence) experiments that were not available here For this reason, the gas temperature was assumed to be 300 K in the following This means that the values of ν_{en} given below are slightly overestimated (by $\approx 35\%$) Typical data from ICPs where charge exchange processes lead to a bath gas temperature typically around 450K at low pressure) The electron cross section required to calculate ν_{en} were taken from Hayashi [66] (elastic), Tachibana [39] (two effective excited states of argon) and Rapp and Englander-Golden [38] (ionisation)

Table I gives a summary of the main plasma parameters deduced from Langmuir and B probe measurements under various plasma conditions The data deduced from Langmuir probe measurements were performed at a radial position of 1 cm from the quartz tube surrounding the antenna, i e inside the skin layer

The parameter Λ is a fundamental measure of the non-locality of electrodynamics in the plasma [57]

$$\text{where} \quad \Lambda = \frac{\lambda_{eff}}{\delta_E}, \tag{3 13}$$

$$\text{where} \quad \lambda_{eff} = v\left(\nu_{en}^2 + \omega_{eff}^2\right)^{-\frac{1}{2}} \tag{3 14}$$

is an effective mean free path for change in electron momentum (including collisions with the electromagnetic field) and $v = (8T_e/\pi m)^{\frac{1}{2}}$ is the average electron velocity As a consequence, the value $\Lambda = 1$ defines the boundary between local ($\Lambda \ll 1$) and non local ($\Lambda \geq 1$) electron interactions with the field Table I indicates that non-local, collisionless effects are expected to be significant under

Table I

The discharge internal parameters measured inside the skin layer at 1 cm from the glass tube

Pressure (mTorr)	Power (W)	n_e $10^{10}\mathrm{cm}^{-3}$	T_e (eV)	δ_E cm	Λ	v_{th}/δ $(10^7\mathrm{s}^{-1})$	ω_{eff}/ω	ν_{en} $(10^7\mathrm{s}^{-1})$	ν_{eff} $(10^7\mathrm{s}^{-1})$
0 4	200	1 5	9 1	1 9	1 55	10 6	0 994	0 356	7 3
0 4	300	2 4	9 8	1 74	1 97	12	1 004	0 361	9 1
1	200	4 85	6	1 5	1 46	10 9	1 053	0 976	5 74
1	300	6 8	6 4	1 45	1 91	11 7	0 996	0 862	7 0
5	200	8 35	4 7	1 33	1 21	10 9	1 057	4 05	5 68
5	300	13 3	5 1	1 15	1 73	13 1	1 070	4 02	6 66
10	200	12 7	3 73	1 25	0 68	10 3	1 186	7 31	7 43
10	300	20 2	3 64	1 1	0 84	11 6	1 201	7 48	7 82

these experimental conditions for pressures below 10 mTorr, as expected from the strong anomalous skin effects that has been observed under these conditions

The condition for transit time collisionless heating to occur (the electrons can traverse the skin layer in a fraction of ω_{rf}) is also fulfilled under the conditions in this experiment since $v/\delta > \omega_{rf}$, and it is thus expected that collisionless heating will be important under those conditions

In order to quantify the ratio of collisionless to collisional power dissipation in the plasma, it is convenient [53, 9, 13, 51] to compare the value of ν_{en} which account only for collisions with that of an effective frequency ν_{eff} deduced from the experiments and that accounts for all kinds of heating mechanisms (ν_{eff} is found by replacing ν_{rf} by ν_{eff} in 3 3) When$E$ and J are known, ν_{eff} can be deduced from

$$\nu_{eff}(r) = \frac{e^2 E_\theta(r) n_e(r) cos\Psi(r)}{m J_\theta(r)} \qquad (3\ 15)$$

The quantitative result in table I indicates unambiguously that at very low pressure (0 4 and 1 mTorr) collisionless heating is the dominant heating mechanism since $\nu_{en} \ll \nu_{eff}$ The ratio ν_{eff}/ν_{en} is plotted in figure 3 8 and shows that starting around 20 at low pressure, it converges toward 1 at 10 mTorr, suggesting that this pressure is the boundary between Ohmic and collisionless dominated heating in this system This is in excellent agreement with the values of Λ found in the experiment, since they indicate that non local phenomena dominate only below 5 mTorr, and this result provides direct quantitative evidence of collisionless heating in ICP

However, it must be pointed out that this method of estimating the importance of collisionless heating is prone to quite high degree of uncertainty for

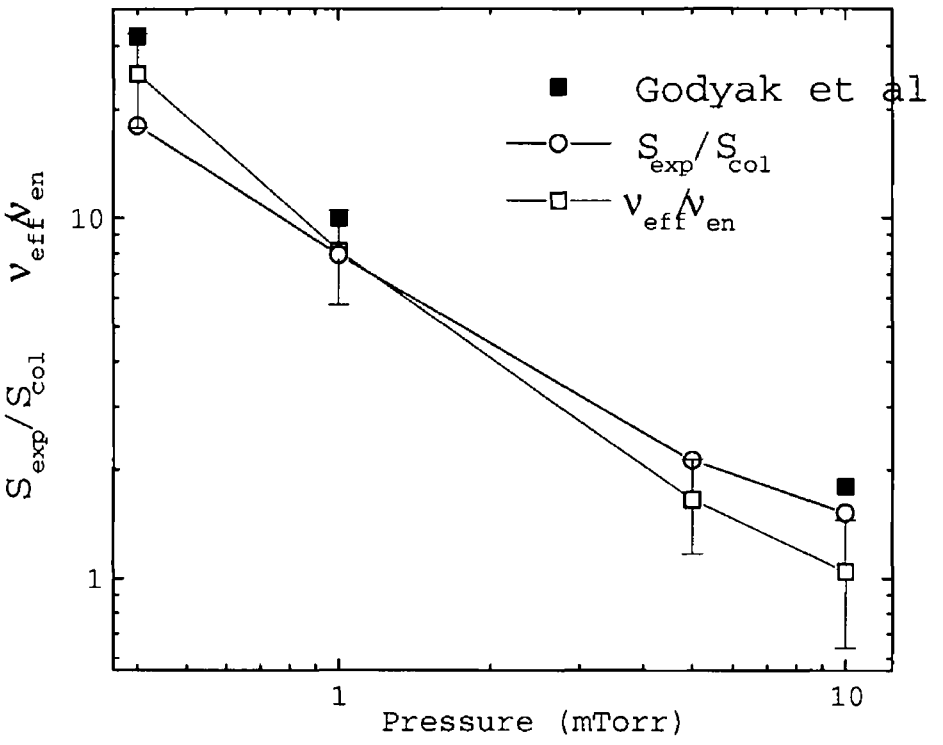

Figure 3 8 *Quantitative comparison of the total and collisional power absorption mechanism The open squares are the ratio of effective collision frequency (including collisions with the rf field) to the purely collisional collision frequency The open circles are the ratio of total to collisional absorbed power flux The black squares show the same ratio published by Godyak et al This demonstrates that collisionless heating is the main mechanism that sustains the plasma at low pressure*

several reasons First and as mentioned previously, ν_{en} is overestimated and thus tends to decrease the importance of collisionless heating Furthermore, ν_{eff} is calculated by assuming that the conductivity can be put in a form similar to that of a cold plasma, although the conductivity is strongly dispersed under those conditions As a result, the value of ν_{eff} deduced from the probe measurement is strongly position dependent (it may even take some negative values at certain positions outside δ) For this reason the value of ν_{eff} was calculated in the middle of the skin layer where the skin effect is the less anomalous (exponential decay of amplitudes and linear decay of the phase), but the uncertainty in ν_{eff} is estimated to be 40% as deduced from the variations of the value of this quantity inside the skin depth

Nevertheless, as discussed in the introduction there is another way to compare the stochastic and collisional contribution by comparing directly the power density $P_{\rm exp}$ with $P_{\rm col}$ By comparison with the preceding calculation, this approach has the advantage of depending neither on ν_{eff} nor n_e and thus is less uncertain However, the value of ν_{en} used to calculate Ψ_{col} is also position dependent (because the EEDF is position dependent), although much less so than ν_{eff}

In order to present the results in a clear fashion it is preferable to compare the line integrated power density i e the power flux $S_{\rm col}$ and $S_{\rm exp}$ rather than directly comparing the power density $P_{\rm exp}$ and $P_{\rm col}$, where S is defined as

$$S(r) = \int_0^r P(y)dy \qquad (3\ 16)$$

$S_{\rm exp}$ and $S_{\rm col}$ were thus calculated as the integrals of equation 3 5 and equation 3 6 over the chamber radius, respectively This has the visual advantage of comparing

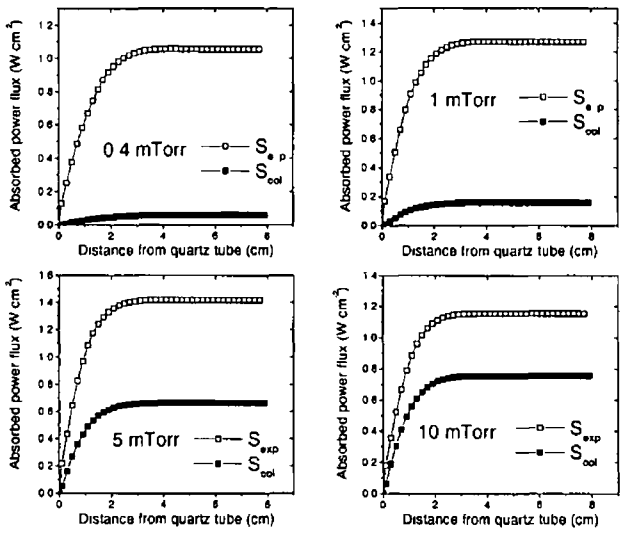

Figure 3 9 *Comparison of the total power flux (S_{exp}) to collisional power (S_{col})flux for 4 different pressures at 230 Watts*

similarly shaped curves ($P_{\rm exp}$ oscillates and becomes negative at some positions, whereas $P_{\rm col}$ does not), and $S(r)$ has also a clear physical meaning since it is equal to the loss of the Poynting flux [9] The power fluxes deduced from these experimental data are presented in figure 3 9 for four different pressures 0 4, 1, 5 and 10 mTorr and a constant power of 230 W It is clear from figure 3 9 that collisionless power absorption does take place at low pressure, since $S_{\rm exp} > S_{\rm col}$ under all conditions, and that it completely dominates collisional heating below 1 mTorr Indeed, the ratio of $S_{\rm exp}/S_{\rm col}$ becomes as high as 18 at 0 4 mTorr, as one can see in figure 3 8 where this ratio is plotted, together with the ratio ν_{eff}/ν_{en} The agreement between these two measurements is better than 30% which is acceptable Furthermore, also plotted in figure 3 8 is the ratio $S_{\rm exp}/S_{\rm col}$ published in reference [9], and this shows an agreement better than a factor of

two with the result presented here (a difference that would become even smaller if a background gas temperature of 450 K instead of 300 K was considered)

Chapter 4

E-H Mode Transition

In chapter 3 the electron heating mechanisms which sustain low pressure inductive discharges in the power range 100 – 300W were discussed In an inductive discharge, the RF power is coupled to the plasma by means of electron interaction with an electromagnetic field induced by the RF current flowing in a coil As was stated, the inductive electric field is non-propagating and penetrates the plasma surface over a distance of the order of the plasma skin depth δ In inductive discharges the voltage across the exciting coil can be as high as several kilovolts, so that a capacitive current can also be driven in the discharge through the dielectric window, this capacitive current provides the basis for a second power coupling mechanism While both power coupling mechanisms normally coexist in an inductive discharge, it is now widely recognised that they represent two distinct modes of the discharge As the excitation RF power (or antenna current) is increased from zero in electrodeless plasmas, the gas first breaks down into a capacitively coupled plasma or E-mode plasma This is characterised by

a low electron density (10^8-10^{10} cm^{-3}) and a glow localised near the coil. Above a certain threshold current, the discharge switches abruptly to a H-mode plasma where inductive power deposition dominates. In this mode, the plasma density is high (10^{10}-10^{12} cm^{-3}) resulting in a much brighter glow (see figure. 4.1). By observing the light output, it is thus in general possible to determine whether the plasma is operating in the E or H mode.

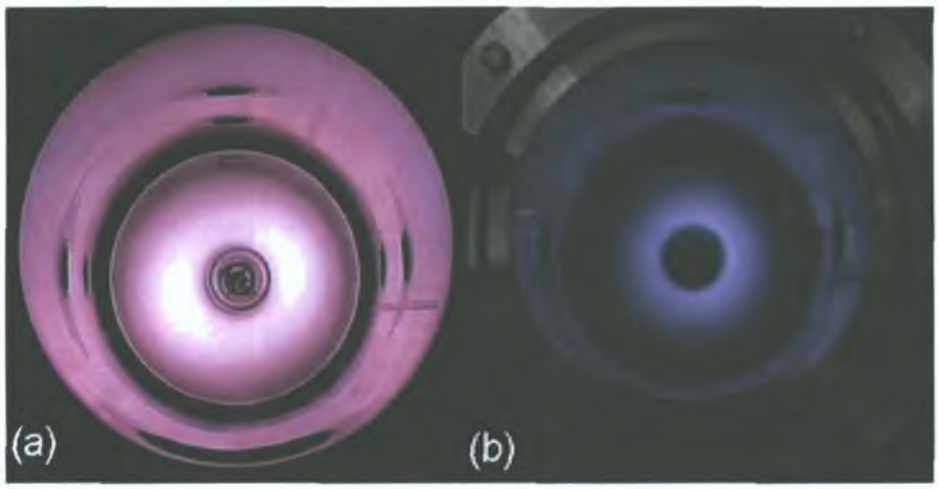

Figure 4.1: *Photograph of inductive argon discharge in (a) H-mode and (b) E-mode*

E to H mode transitions have been frequently described in the literature and shown to exhibit hysteresis in respect of the coil current [17, 18, 67]. In the following experiments light output was measured using a 50 cm spectrometer focused onto a photomultiplier tube. The 750 nm argon line was used since it gave the largest signal. The E to H transition (observed by increasing the RF power) occurs at an antenna current i_1 which is different from the current i_2 at which the reverse H to E transition (observed when decreasing the power) occurs.

It is also possible to say that the discharge is bi-stable, i.e. that there is a range of coil currents that can support both modes [21].

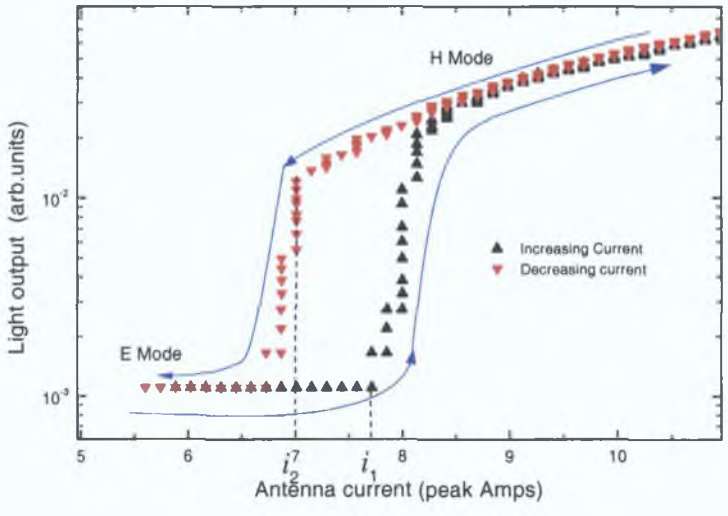

Figure 4.2: *Light output plotted as a function of antenna current in an argon plasma at a pressure of 5 mTorr, the plot clearly illustrates the hysteresis in transition current.*

Referring to figure 4.2, as the current is increased following the arrow the E-H transition occurs at $i_1 = 7.7$ amps, here an order of magnitude increase in the light output occurs. As the current is further increased the light output continues to increase, at 12 amps the current is decreased and the light output decreases along the same path as the increasing curve but in this case the discharge remains in H-mode until the current reaches $i_2 = 7$ amps before undergoing the H-E transition. In this case it can be said that bi-stability is exhibited in the range of currents between 7 and 7.7 amps. While in figure 4.2 the light appears constant in the E-mode this is due to the limited dynamic range of the light detector, other observations show that the light increases with current.

It has been suggested recently that the existence of a threshold current for the H mode and of the hysteresis originates in the electron energy balance in the discharge [18, 67, 21] This idea follows from the elementary consideration that for a stable E or H mode discharge to exist, the power absorbed by the electrons, P_{abs}, must identically balance the power dissipated P_{dis} The starting point for analysis is that the electron temperature in a discharge is determined predominantly by particle balance, and thus does not depend on the electron density [5] Consequently, the energy lost per ionisation is fixed and the power dissipated by the plasma electrons varies linearly with the electron density n_e A simple linear relation between P_{dis} and n_e should in principle hold both for an E and H mode discharge

The power absorbed by the plasma electrons is estimated by using a circuit analysis derived from the so-called *transformer formalism* in which the inductive plasma is considered to be a one turn secondary of an air-core transformer [13, 19] The circuit analysis allows one to deduce the density dependence of the power absorbed by the discharge electrons $P_{abs} = \frac{1}{2}R_e i^2$ where R_e is an effective resistance added in series with the coil inductance and represents the electron contribution for power dissipation and i is the antenna current Considering only the inductive coupling, at small enough n_e, the induced field is essentially the vacuum field (determined by the chamber and antenna geometry) and the power absorbed inductively scales as $R_e \propto n_e$ (see figure 4 3(a)) On the other hand, when n_e is high enough the skin effect confines the electromagnetic field in a region near the dielectric window and power absorbed is reduced according to the scaling [5]

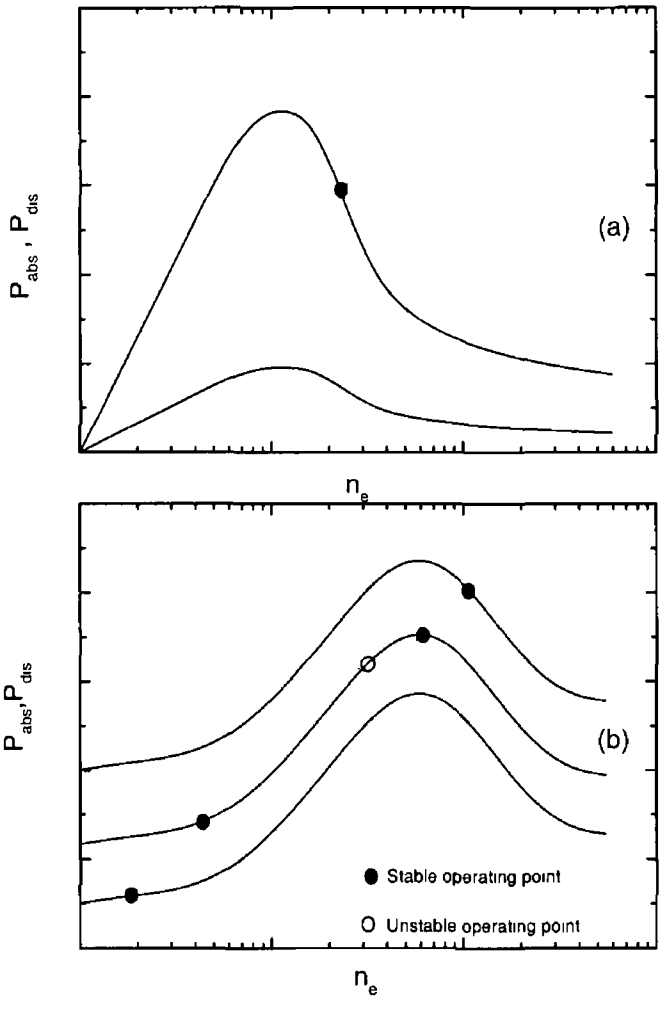

Figure 4 3 *Power balance in an inductive discharge illustrating a number of possible operating points (a) without hysteresis, showing* P_{abs} *(solid lines) and* P_{dis} *(dotted line) for two different coil currents below the threshold current and above the threshold current (b) Shows a power balance diagram which includes the possibility of hysteresis,* P_{abs} *(solid lines) and* P_{dis} *(dotted line), for three different coil currents*

$$R_e \propto n_e^{-\frac{1}{2}} \tag{4 1}$$

The stable operating points in density n_e for the E and H modes of the plasma can then be found by equating absorbed and dissipated power

$$P_{abs}(n_e) = P_{dis}(n_e) \tag{4 2}$$

and the graphical solution [figure 4 3(a)] shows that this equation has either one or two solutions If there is only one solution, it is at $n_e = 0$ which means that the current is too low to support an H-mode plasma When there are two solutions, one is at $n_e = 0$ and the other is at a finite density corresponding to a stable H mode Thus a pure inductive discharge can only exist above a certain threshold current for which equation 4 2 has two solutions There is no hysteresis in this simple approach

To obtain hysteresis and electron density jumps typical of a discontinuous transition, it is necessary to introduce a nonlinearity either in P_{dis} or in P_{abs} (or both) at low n_e [21] A nonlmearity in the absorbed power was introduced by El-Fayoumi et al [67], Suzuki et al [18], Lieberman et al [68] by including the capacitive coupling between the coil and the plasma Capacitive coupling is responsible for the E mode and can be included in the transformer circuit as a separate branch [67, 21, 68] It can also be treated separately [18] The capacitive branch does introduce a non-linearity in P_{abs} at low density, and as a result the graphical solution of equation 4 2 now shows that for a given antenna current, either 1 (E or H mode) or 3 solutions can be obtained for n_e The three solutions correspond to the stable E and H modes and an unstable intermediate mode

[figure 4 3(b)] the intermediate mode is unstable since if operating at this point then any small perturbation in density will be amplified resulting in the operating point shifting to a position near either of the other two operating points The hysteresis can now be explained in a simple manner when two stable points (E and H) are possible for a given current, the plasma will remain in the E or in the H mode depending on its previous history When the coil current is increased, the electron density 'jumps' from the last accessible value in the E mode (low density) to the new accessible H mode of high density, in good agreement with measurements El Fayoumi et al [67] have pointed out that the major effect is probably reduction in the power transfer efficiency for the H mode due to the large capacitive sheath which reduces n_e near the coil, the capacitive and inductive branches of the transformer circuit do not respond independently to the applied voltage

Turner and Lieberman [21] have reconsidered the problem in detail and surveyed several other possibilities that can produce hysteresis Relevant mechanisms divide into two categories affecting either the absorbed or dissipated power Nonlinearity in absorbed power results from various circuit effects, including power loss in the matching unit Nonlinearity in dissipated power (first mentioned by Kortshagen et al [17]) can arise from changes in the efficiency of plasma production when, for example, multi-step ionisation is included A transition from a Druyvesten to a Maxwellian shape of the electron energy distribution function (EEDF) due to Coulomb collisions in the dense H mode can also produce nonlinearity The qualitative explanation for the hysteresis remains the same (two stable and one unstable point), but the graphical solutions are differ-

ent, leading to a bigger hysteresis loop [figure 4 3(b)] and to different behaviour as a function of pressure

An interesting aspect of the mode transition that occurs in an ICP is the evolution of the plasma during the transition The dynamics of the E to H transition has been described qualitatively by Kortshagen et al [17] as follows starting with an E mode plasma and increasing the antenna current, a value is reached where the induced electric field can produce ionisation At this point the ionisation rate suddenly becomes higher than the loss rate, power balance no longer holds and n_e starts to increase Since the effectiveness of inductive power deposition increases linearly with n_e (at low n_e), a higher amount of power is absorbed with increasing n_e, and the electron density will continue to rise At high enough n_e the skin effect becomes significant and as discussed previously (figure 4 3) the dependence of R_e with n_e becomes sub-linear the inductively absorbed power grows more slowly than n_e and a new steady state H-mode discharge satisfying power balance is finally reached Thus a stable H-mode discharge forms when the skin depth becomes smaller than the typical dimension of the vacuum chamber

The experimental results found in the literature have generally been obtained by increasing the RF power step by step, and by measuring plasma parameters at those points Such an approach has the advantage of being straightforward, but because of the discontinuous character of the E to H transition, the dynamics of the transition cannot be studied in this manner The plasma parameters are measured only before or after the transition The steps by which the power is increased are finite, and this also leads to imprecision in the measured transition

currents and thus to the size of the hysteresis loop Another technique used by El-Fayoumi et al [67, 20] consists of varying the value of the tuning capacitor in the matching network in order to change the antenna current and thus obtain the desired E to H (or H to E) transition This has the disadvantage of changing the matching condition during the measurement

In this chapter the plasma parameters in steady state E and H mode discharges, are determine at different pressures in argon Spatial profiles of the electron density n_e, temperature T_e, plasma potential V_p and the EEDF between the quartz tube surrounding the coil and the grounded walls are measured The non-linearity in dissipated power is discussed on the basis of these results In addition, a novel experimental approach to investigate the E-H transition and the hysteresis was undertaken A particular type of pulsed discharge is used in which the RF power is slowly ramped up and down during each pulse In this way, the whole range of power is applied allowing the dynamics of the transitions to be investigated A similar approach was used by Ellingboe and Boswell [69] in a helicon source in order to investigate the E to H to W (wave sustained discharge) transitions

To investigate the pulsed discharge, a number of time-resolved diagnostics have been used, these include a rf current and voltage sensor, a directional power meter, a Langmuir probe, B probes and optical emission spectroscopy The results are given for 2 gas pressures, 5 and 150 mTorr, and the system behaviour during the transition is discussed

4.1 Experiment

A Marconi 2022D signal generator is used to provide a 13 56 MHz signal which is amplified by an ENI wideband power amplifier with an output power of up to 1 5 kW The rf power is fed to the antenna through a RFPP AM20 automatic matching network consisting only of two capacitors The antenna has a high enough inductance to replace the inductor of a conventional L-type matching unit Several matching conditions were set up in the experiments as described below, but the matching unit was always used in manual mode with values of the tuning and load capacitors held fixed for a set of measurements The rf signal generator output can be modulated by applying an external signal, an additional function generator was used to ramp the rf voltage up and down The resulting pulse shape is in principle a simple triangle but under certain conditions (high repetition rates), the signal generator can saturate, giving a pulse with a constant middle section However, the important point is that the E to H and H to E both occur during the ramping periods

A number of time resolved diagnostics is used to investigate the pulsed discharge A Scientific Systems current/voltage sensor is located at the output of the matching unit and provides a measurement of the time evolution of the rms values of the antenna voltage V and current i The signals are displayed and recorded on a HP 54510A digital oscilloscope with a 2 GSs^{-1}sampling rate The absorbed power was not deduced from the data since it was not feasible to correctly measure the phase on a time scale of 9 ms with the oscilloscope and to

deduce the power factor

$$\cos\Phi = \frac{P_{abs}}{iV} \tag{4 3}$$

The absorbed power is measured directly with a Bird directional rf power meter modified to improve the time response and hence obtain the time evolution of the forward and reflected power through the antenna, P_{in} and P_{ref} respectively The power dissipated in the antenna coil was estimated by measuring the antenna resistance in vacuum $R_a = (P_{in} - P_{ref})/i2 = 0\ 36\ \Omega$ and the real power absorbed by the plasma electrons and ions is then deduced from

$$P_{abs} = (P_{in} - P_{ref}) - R_a i^2 \tag{4 4}$$

The Scientific Systems Smartprobe Langmuir probe system, which is described fully in chapter 2, is used to measure the plasma parameters The probe is operated in a boxcar averaging mode, giving time-resolved measurements of the plasma parameters with a resolution of 5 μs Measurements can be made at any time in the pulsed discharge by triggering the Langmuir probe system by a Stanford Research SR 535 delay generator which provides TTL output that can be delayed with respect to the beginning of the ramp The 750 4 nm argon line emission is also monitored by a 50 cm spectrometer, and comparison with the Langmuir probe results allow the relative variations of the electron temperature to be deduced

The B_z component (parallel to the antenna axis) of the electromagnetic field is measured with the immersed B-dot probe described in section 2 5 The linear motion assembly used for the Langmuir probe is also used for the B-dot probe, allowing the measurement the space and time evolution of B_z

Two different kinds of experiments are described in the following Each of these requires a specific procedure for matching the plasma In a first set of experiments the E and H mode of a steady state discharge are characterised For these experiments the plasma was matched for a stable E-mode discharge, and the input power was increased without changing the matching conditions The reason for this choice is that the power absorbed by the plasma before and after the transition differs only by a few tens of watts with this matching, while it can change by more than 100 W if the plasma is matched for an H mode For the experiments in a pulsed discharge the initial matching conditions must be considered In all cases the discharge was matched in a steady state E or H mode plasma prior to pulsing, and kept unchanged during the pulse This will be referred to as E-mode or H-mode matching in the following

Finally, another important point must be made about the pulsed experiments The length of the pulse is chosen to be long enough (typically 9 ms) to limit the effects of ambipolar diffusion, i e the period of ramp down is not an afterglow period The repetition rates of the pulses are set so that the afterglow period following one ramp is long enough to allow the plasma density to decrease to nearly zero, and for a gas breakdown to occur during the following pulse This power off time is typically 0 1-1 ms depending on the pressure The long decay time of the charged species is due to the fact that the power is modulated to only 99 5% This means that $\approx 1-2$ W of power is absorbed in the early afterglow where the ambipolar diffusion is very slow because the electron temperature has dropped to a low value

4.2 Results

4.2.1 Hysteresis in the system

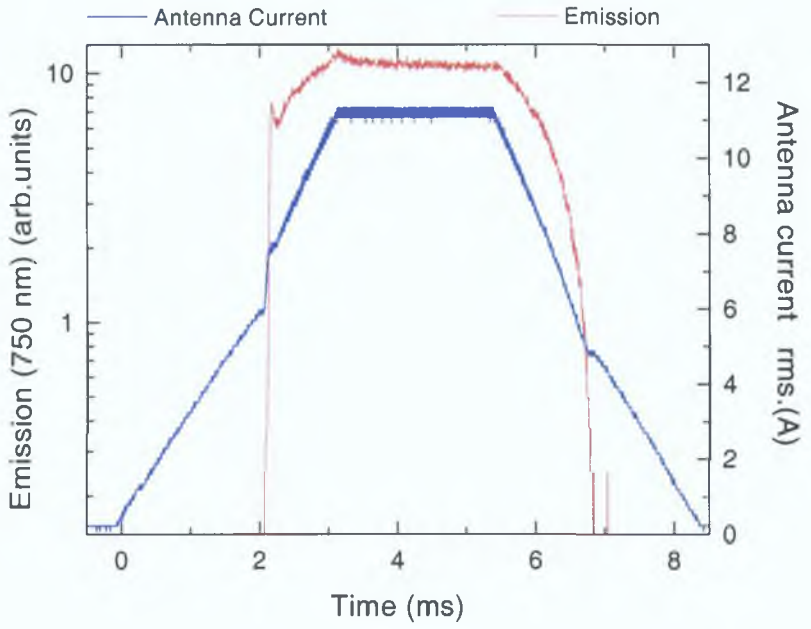

Figure 4.4: *The time evolution of the antenna current and the plasma emission during the ramped power pulse in a 5 mTorr discharge with H-mode matching.*

The pulsed mode of operation is used to quantify the size of the hysteresis loop in the system. The time evolution of the antenna current and the plasma emission during the ramped power pulse in a 5 mTorr discharge with H-mode matching is shown in figure 4.4. Figure 4.5 shows the time evolution of the plasma density and absorbed power along with the ramp used to provide the pulse. The power ramp begins at time $t = 0$ and the gas breaks down to form an E-mode discharge at time $t = 330$ μs. The breakdown can be seen as a small 'glitch' on the current due to new resistive load caused by the presence of the plasma [70, 71]. The E to H transition can be clearly seen here as a large increase

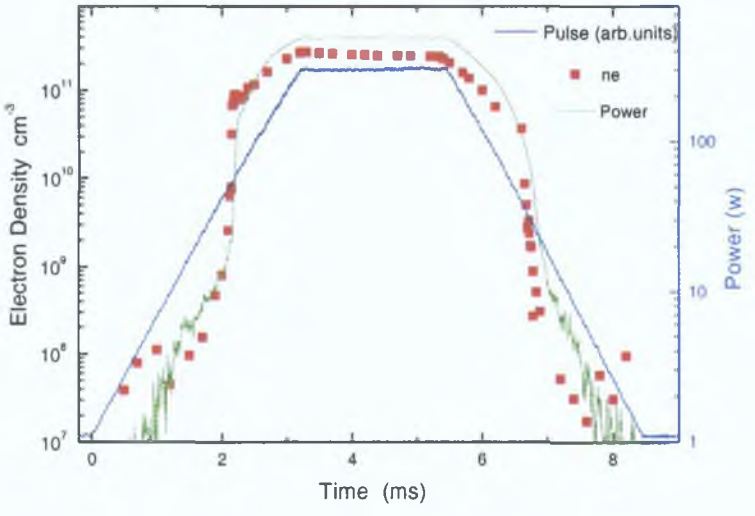

Figure 4.5: *The time evolution of the plasma density (red squares), the absorbed power (green line) and the driving pulse (blue line) for the same conditions as in figure 4.4.*

in the current accompanied by an increase of 2 orders of magnitude in the plasma emission at $t = 2.16$ ms for a current of 6.3 A. This transition current at which the plasma emission starts to increase will be referred to as the threshold current in the following. The subsequent evolution is imposed by the power modulation and the reversed H to E transition occurs when the decreasing current reaches 4.9 A (this will be called the maintenance current). In this low pressure case the hysteresis is considered to be small since the threshold and maintenance currents differ only by 22%.

The pulsed technique thus allows for the precise determination of the critical values of the maintenance and threshold currents, and hence the exact size of the

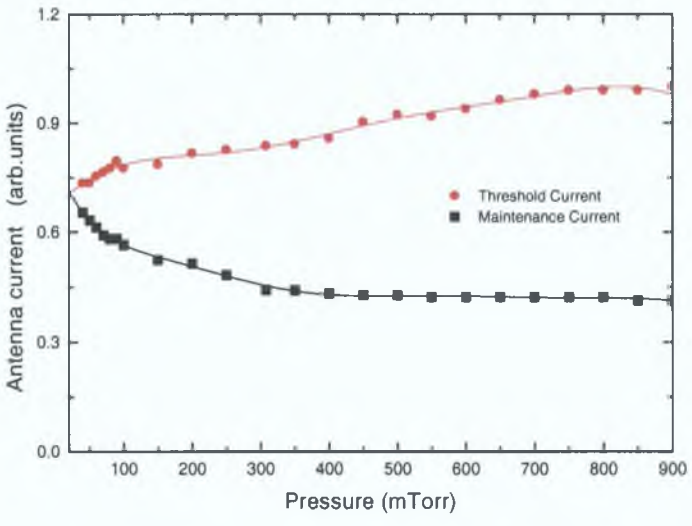

Figure 4.6: *Maintenance current (squares) and threshold current (circles) plotted as a function of pressure.*

hysteresis loop. However, as discussed later, the H to E transition appears to be very smooth (continuous) at higher pressure, this makes the determination of the maintenance current difficult. In this case the plasma emission rather than the antenna current is used to find the time of the transition. Measuring the two current values at different pressures enables the determination of the hysteresis loop size dependence with pressure. These results, shown in figure 4.6 that the very small loop ($\approx 20\%$) observed at low pressure can become considerable ($> 200\%$) at higher pressures. Clearly, the mechanism producing hysteresis has a strong pressure dependence which is investigated by concentrating on the existence, at different pressures, of the non linearity in dissipated power suggested by Turner and Lieberman.

4.2.2 Measurements in steady state discharges

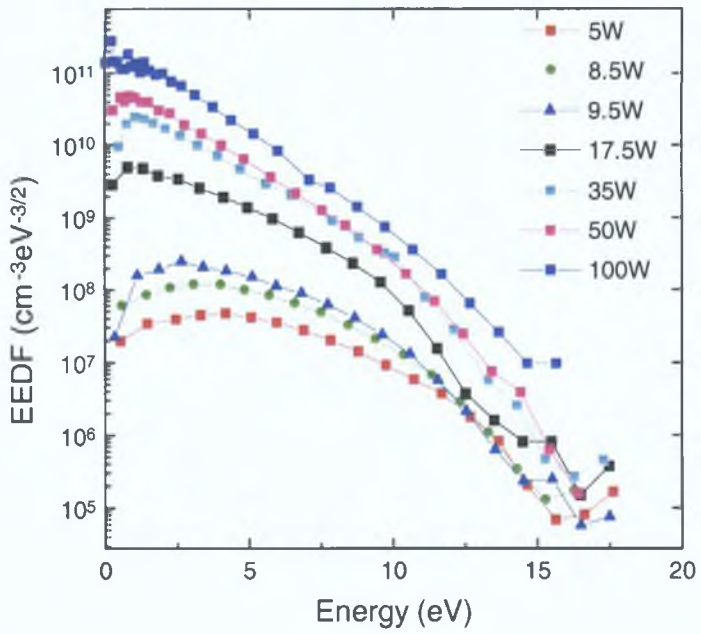

Figure 4.7: *Electron energy distribution functions measured by the Langmuir probe in a 150 mTorr plasma at different powers.*

One possible explanation of the pressure dependence of the size of the hysteresis loop is that the form of the EEDF changes with pressure. This is because the energy required per electron-ion pair created depends on the form of the EEDF. In particular if the EEDF is Maxwellian then less energy will be required to sustain a plasma of a given density than if the form of the EEDF is Druyvesteyn. Hence, if at a particular pressure, both the E and H modes of an ICP had a Druyvesteyn EEDF then the plasma production efficiency would be the same in both modes (in the absence of any other non-linearities in P_{dis}). In this case one would expect the E to H mode transition to occur at the same power and coil current as the H to E transition. However if the form of the EEDF is Maxwellian in the H mode and Druyvesteyn in the E mode then the H mode plasma would

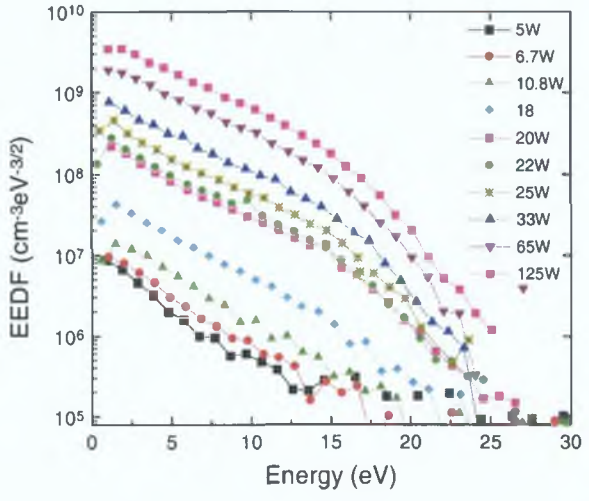

Figure 4.8: *Electron energy distribution functions measured by the Langmuir probe in a 5 mTorr plasma at different powers.*

be more efficient in terms of electron-ion pairs created per unit energy. In this case it is expected that the H mode plasma could be sustained at a lower power than that required to cause the transition from the initial E mode plasma. Measurements at different pressures in steady state plasmas operating either in the E or the H mode were performed in order to check whether changes in the efficiency of plasma production change significantly with pressure. To begin with, the EEDFs measured by the Langmuir probe in a 150 mTorr plasma at different powers are shown in figure 4.7. The distributions were measured at a radial position of 60 mm from the centre of the system, corresponding to the peak electron density. Below 9.5 W the discharge remains in an E mode and glows locally near the quartz tube. As the power is increased by a small amount above 9.5 W the plasma undergoes a sharp E to H transition leaving the plasma in the much more

dense H mode absorbing a power of 35 W It is obvious here that during the transition, the shape of the EEDF changes, with a switch from a Druyvesteyn-like distribution in the E mode to a Maxwellian-like distribution in the H mode, in good agreement with the argument developed previously Since the energy that must be supplied to support an electron-ion pair over its lifetime depends on the EEDF shape, this change in the EEDF will lead to a nonlinearity in P_{dis} and so contribute to hysteresis in the transition

In order to investigate the pressure dependence of this phenomenon, the same experiment was performed at the lower pressure of 5 mTorr, where the hysteresis is weak and the results are presented in figure 4 8 It appears that the transition from Druyvesteyn to Maxwellian type distributions that exists at high pressure has disappeared, and that the EEDF shape is approximately Maxwellian in both the E-mode and H-mode discharge This observation is in good agreement with the much smaller hysteresis loop observed at low pressure It can be concluded that at least part of the large hysteresis that is observed at high pressure is due to the rearrangement of the EEDF caused by electron-electron interactions at high densities

The second possible source of plasma non-linearity suggested by Turner and Lieberman, namely multi-step ionisation, is more complicated to detect experimentally However two sets of experiments have been carried out in order to give credence to the hypothesis Firstly, the radial distributions of the electron densities were measured at different pressures and compared with the results obtained by a fluid model [72] The experimental density profiles are presented in figure 4 9 (a) and (b) for a 5 mTorr discharge These profiles were found to be

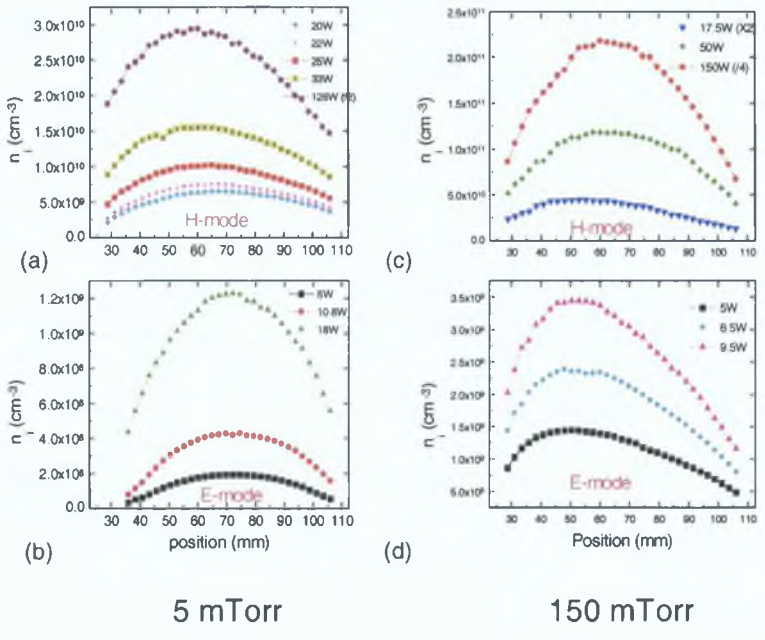

Figure 4.9: *Evolution of density profiles during the E to H transition (a) 5 mTorr, H-mode (b) 5 mTorr E-mode (c) 150 mTorr, H-mode (d) 150 mTorr, E-mode*

in very good agreement (both in the form and the absolute value of peak density) with a 'simple' fluid model which does not include metastable states and multi-step ionisation. It is concluded that this phenomenon is not significant at low pressure and this agrees with simple considerations of the metastable loss processes. At low pressure the electron density is low and the loss of metastable excited atoms is dominated by radial diffusion to the chamber walls, so multi-step ionisation is not important.

Figure 4.9 (c) and (d) shows the density profiles at 150 mTorr. It is apparent here that the spatial profile of the electron density changes during the transition, peaking near the quartz tube in the E mode and becoming symmetric in the H-mode. This behaviour is quite different from the results obtained with the fluid

code which gives a lower overall density with a peak near the quartz tube The disagreement suggests that an extra source of ionisation is missing in the fluid code, the most important probably being multi-step ionisation Furthermore, Turner and Lieberman [21] have also performed computer simulations of the density profile in a system similar to the one used here (re-entrant geometry), and obtain density profiles that are very similar to these experimental results when multi-step ionisation is included into the model The comparison with the simulations tends to indicate that multi-step ionisation is an important phenomenon in this system at high pressure, and that this can also be a source of increasing hysteresis at higher pressure

In a second set of experiments, the contribution of multi-step ionisation to the overall ionisation source term as function of pressure was investigated by determining radial the distribution of the ionisation source term and the radial distribution of the power deposition The source term was determined by a computer model developed by Turner [73] This model involved inverting the plasma transport equation that is assumed to be the ambipolar transport equation,

$$S(r,z) = \nabla(D_a \nabla n(r,z)) \tag{4 5}$$

where n is the plasma number density $D_a(r,z)$ is the ambipolar diffusion coefficient and $S(r,z)$ is the ionisation source term The number density, $n(r,z)$ is determined directly from Langmuir probe measurements which are spatially resolved in the r and z directions The inversion is attained using an itererative process in which an initial estimate of the source term $S(r,z)$ is made from which equation 4 5 is solved for $n(r,z)$ in the forward direction using a rapid elliptic

solver The source term is then refined using Gold's ratio method

$$S^{(i+1)} = \frac{n_{exp}}{n^i} S^i, \tag{4 6}$$

where i denotes the iteration number While there is no proof that this method uniquely converges it has been successfully tested on model problems [50, 73] A full discription of the method and the computer program used for the calculation is given in reference [50] The power deposition was measured directly by the B probe as described in section 2 5 Measurements were made over a range of pressures under two conditions firstly, in a pure argon discharge where it is predicted that two step ionisation is an important process [36] at high pressure and secondly in a mixture of 99% argon and 1% oxygen where it is predicted that the oxygen will de-exite the metastable argon atoms through the process of resonant excitation transfer [74] and hence stop the two step ionisation process

Figure 4 10 shows an example of the results of the experiments and inversion procedure The data was taken in a pure argon discharge at a pressure of 100 mTorr and input power of 100 W from profiles such as these data was extracted to build radial profiles (figures 4 11 to figure 4 13) of $n(r)$ and $S(r)$ along the antenna mid-plane

Figure 4 11 shows the radial profiles of ionisation source terms (blue squares) and electron density (red squares) for (a)pure argon at 20 mTorr, (b) 99% Ar &1% O_2 at 20 mTorr, (c) pure argon at 100 mTorr and (d)99% Ar & 1% O_2 at 100 mTorr Comparing figure 4 11 (a) and 4 11 (b) it is clear that the addition of a small amount of oxygen does not effect the shape of the electron density profile at

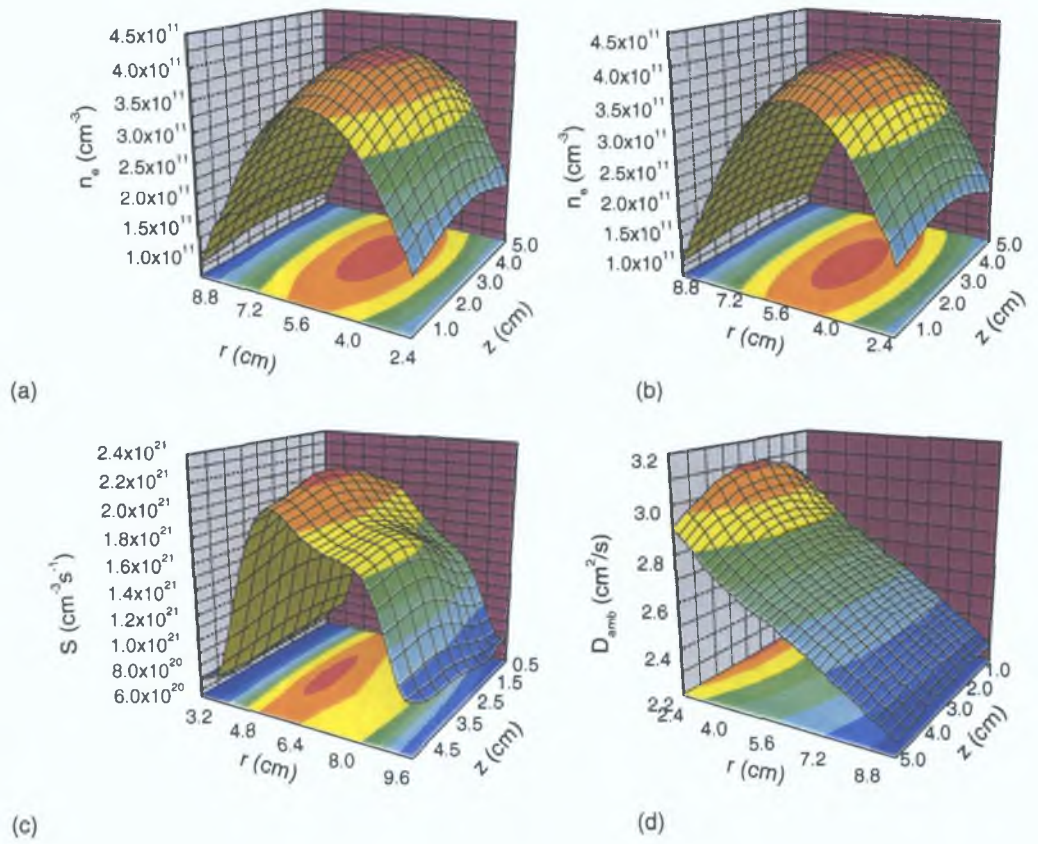

Figure 4.10: *Three dimensional profiles of (a) The experimentally measured electron density ($n(r,z)$). (b) The electron density obtained from the source term. (c) The Source term $S(r,z)$. (d) The diffusion coefficient. The operating conditions here are 100 W pure argon discharge at 100 mTorr*

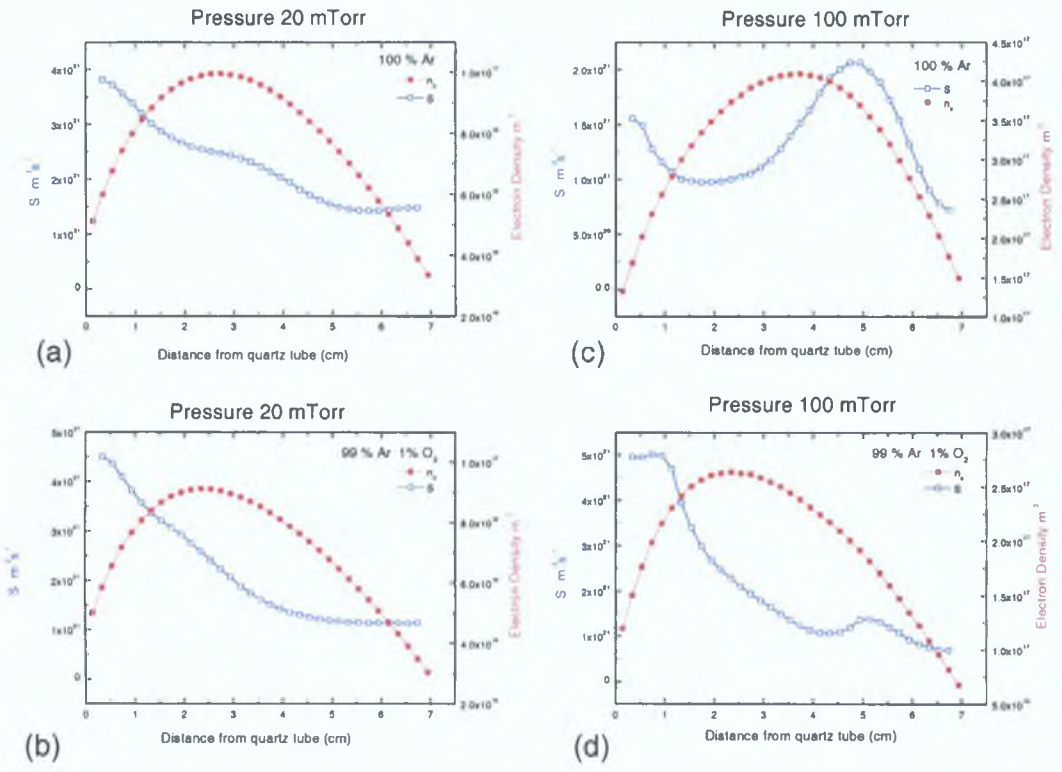

Figure 4.11: *Radial profiles of ionisation source terms (blue squares) and electron density (red squares) for (a)pure argon at 20 mTorr, (b) 99% Ar &1% O_2 at 20 mTorr, (c) pure argon at 100 mTorr and (d)99% Ar & 1% O_2 at 100 mTorr. The power is 100 W in all cases*

low pressure but the average value of the electron density decreases by $\approx 10\%$ In both the low pressure argon plasma and the argon-oxygen mixture the ionisation source profiles are similar, with most of the ionisation taking place in the high azimuthal electric field region close to the quartz tube where most of the power is absorbed by the electrons At high pressure (100 mTorr) comparing figure 4 11 (c) and 4 11 (d) it is found that in pure argon the density profile changes substantially becoming much more symmetric around the centre of the discharge than in the low pressure case, but adding a small amount of oxygen dramatically reduces the average density (by $\approx 40\%$) and also restores the density profile to the same shape as the low pressure case in both argon and the argon-oxygen mixture While at low pressure the ionisation source profiles was found to be only slightly effected by the addition of oxygen, at high pressure the ionisation source profile was completely changed in pure argon the profile is found to have a maximum close to the walls of the chamber (at r=5 cm) and not within the skin depth where the power is deposited, but the addition of oxygen changes the profile to one similar to ionisation profile at low pressure

Figure 4 12 shows radial profiles of the ionisation source terms (triangles) and absorbed power (circles) for pure argon (black curves) and 99% Ar & 1% O_2 (red curves) at 20 mTorr It is clear from the graph that the power deposition profile is almost the same regardless of the composition of the gas The skin depth is slightly longer in the argon-oxygen mixture than in the pure argon plasma The ionisation source term profiles are also quite similar for both cases apart from a slight increase in the profile, which occurs in the pure argon near the centre of the discharge Figure 4 13 shows radial profiles of the ionisation source terms

(triangles) and absorbed power (circles) for pure argon (black curves) and 99% Ar & 1% O_2 (red curves) at 100 mTorr, again it is clear from the graph that the power deposition profiles are similar regardless of the composition of the gas. It is also clear from 4.13 more ionisation takes place outside the skin depth

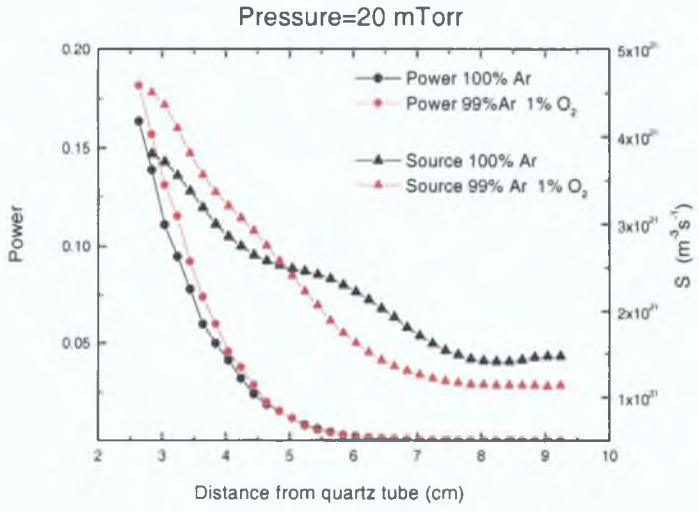

Figure 4.12: *Radial profiles of the ionisation source terms (triangles) and absorbed power (circles) for pure argon (black curves) and 99% Ar &1% O_2 (red curves) at 20 mTorr*

In conclusion, it appears that the two sources of non-linearity in dissipated power discussed above both play a significant role in this discharge, and that the pressure dependence of the mechanisms is in good agreement with an increasing hysteresis loop with pressure. In considering whether these sources of hysteresis are dominant, it should be noted that it was not possible to shield the antenna during the experiments and thus to separate the sources of non-linearity in P_{abs} and P_{dis} by removing capacitive coupling. However, it can be seen in figure 4.9 (b) that there

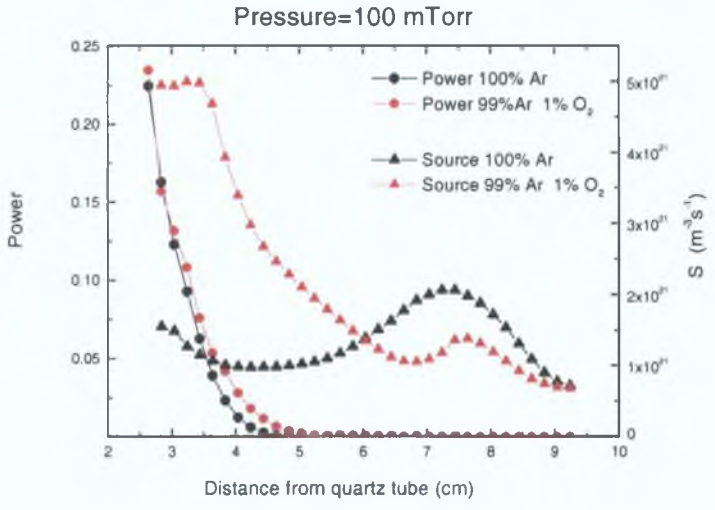

Figure 4.13: *Radial profiles of the ionisation source terms (triangles) and absorbed power (circles) for pure argon (black curves) and 99% Ar & 1% O_2 (red curves) at 100 mTorr*

is a large capacitive sheath (at least 9 mm wide) near the quartz tube in the E mode at low pressure (the missing data points near the quartz tube correspond to the limit where the probe tip was entering the sheath). The screening mechanism suggested by El-Fayoumi et al. is therefore also present in this system, but based on their estimates, can only make a contribution of less than 20% to the hysteresis here. The sheath size rapidly decreases with increasing pressure, and consequently the screening becomes less important with increasing pressure. For this reason, at high pressure in this system, non-linearity in P_{dis} offers a better explanation of the experimental observations. The hysteresis remaining at low pressure comes from a non linearity in the power P_{abs} in the inductive branch of the transformer circuit. In order to proceed further, the effect of matching on the hysteresis loop is investigated.

4.2.3 Effect of matching

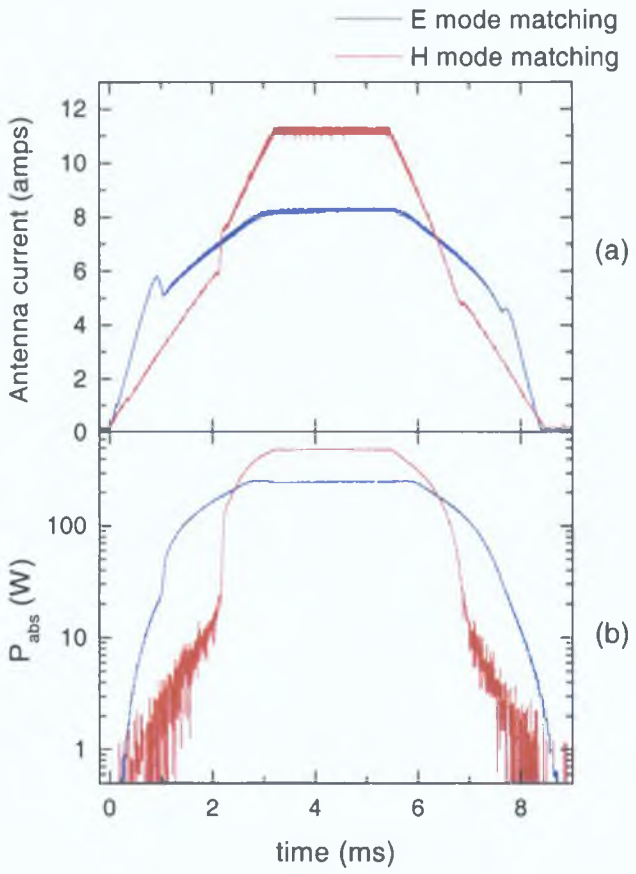

Figure 4.14: *The time evolution of the rms value of (a) the antenna coil current and of (b) P_{abs} for a 5 mTorr discharge with different initial matching.*

The effect of matching was investigated by comparing the results obtained by running the pulsed discharge with two different initial values of the tuning capacitor in the matching unit, specifically with E and H mode matching conditions set up as described Section 4.1. The time evolution of the rms value of the coil current and of P_{abs} are plotted together in figure 4.14 for a 5 mTorr discharge with different initial matching. In the figure, P_{abs} is the total power absorbed by the

discharge, and the power ramp begins at time $t = 0$. As mentioned previously, the gas breakdown and the E to H and H to E transitions can be seen without ambiguity on the current waveform. Figure 4.14 also shows that P_{abs} increases dramatically during the transition for both matching conditions.

It can be seen in figure 4.14 that there are significant differences in the current and power waveforms with the two matching conditions. When matched in E mode, gas breakdown and the E to H transition occur at an earlier time simply because the reflected power is lower in the E mode and as a consequence the absorbed power increases faster than when the discharge is initially matched for an H mode. This also explains why the power deduced from Equation 4.4 is more noisy when the discharge is matched in the H mode, since the small power measured in the E mode is obtained from the difference of two large numbers $P_{in} - P_{ref}$. However, it appears from figure 4.14 that the transition threshold

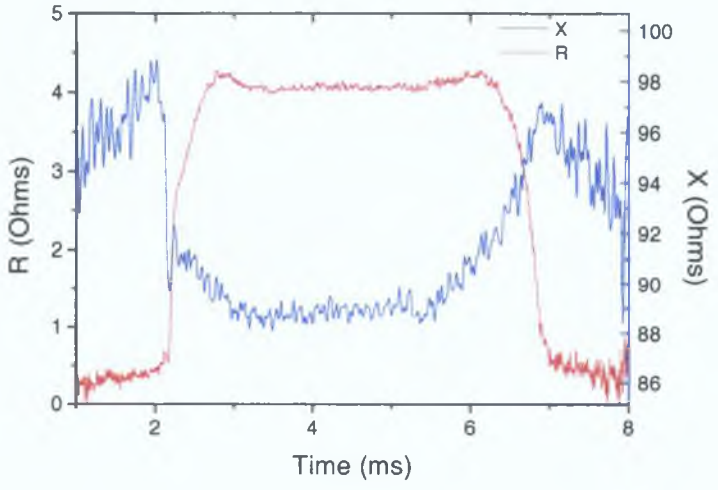

Figure 4.15: *The time evolution of the plasma resistance and reactance as seen from the primary coil*

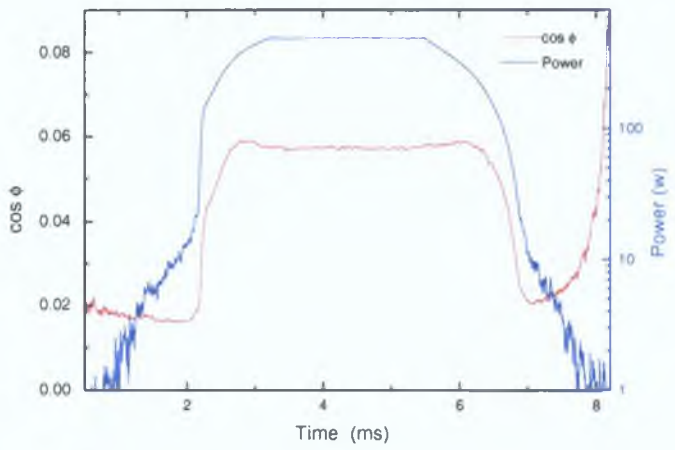

Figure 4.16: *The time evolution of the power factor cosϕ*

current is the same in both cases. In contrast, the H to E transition occurs at a slightly lower current, implying that the hysteresis loop is $\approx 5\%$ greater when the matching is done in the E mode. The transition currents were measured as the maximum and minimum value of i for the E to H and H to E transitions respectively. A striking feature of figure 4.14 is that depending on the matching conditions, the current can either increase or decrease during the transition. This may seem to indicate that the real part of the plasma impedance can either increase or decrease during the transition depending on the matching. However it is important to bear in mind that the power of the discharge is modulated, and that under such conditions an increase or a decrease of the coil current are both compatible with an increase of the plasma resistance. This increase in resistance can be seen in figure 4.15 and 4.16 where the time resolved measurements of i, V and P_{abs} have been used to find the power factor ($cos\phi$) and the time evolution

of the plasma resistance and reactance as seen from the primary coil [13, 20]

$$R_p = \frac{V \cos \Phi}{\imath} - R_a \tag{4 7}$$

$$X_p = \frac{V \sin \Phi}{\imath} \tag{4 8}$$

The real part of the plasma impedance originates from electron collisions with other particles and in a collisional plasma, R_p, the resistive load which is added to the antenna resistance due to the presence of the plasma, increases with n_e The imaginary part of the plasma impedance decreases with n_e since the presence of the inductive plasma current counteracts the coil current and screens out the rf field leading to a decrease in the inductance of the coil

The same experiment at higher pressure leads to the same conclusion, except that at 150 mTorr the maintenance current for the E to H transition depends slightly on the matching, rising from 4 25 Amps for H mode matching to 4 66 Amps for E mode matching as is seen in figure 4 20, in this case, the E to H transition is obvious on the current waveform, but the H to E transition is smooth rendering impossible the location of the reverse H to E transition from the time evolution of the coil current The position of the transition is estimated from the plasma emission where it is assumed that the H to E transition occurs when the light intensity reaches the same level that was observed in the E mode at the beginning of the E to H transition In this way it is found that the H to E transition occurs around 1 78 amps and 1 92 amps for H and E mode matching respectively This implies that the size of the hysteresis loop is this time again 10% bigger when the system is matched for supporting an E mode plasma

In conclusion it can be stated that while the time evolution of the plasma

characteristics such as P_{abs} and the electron density are greatly affected by the matching unit, the size of the hysteresis loop and the maintenance currents are only slightly modified

4.2.4 Transition dynamics

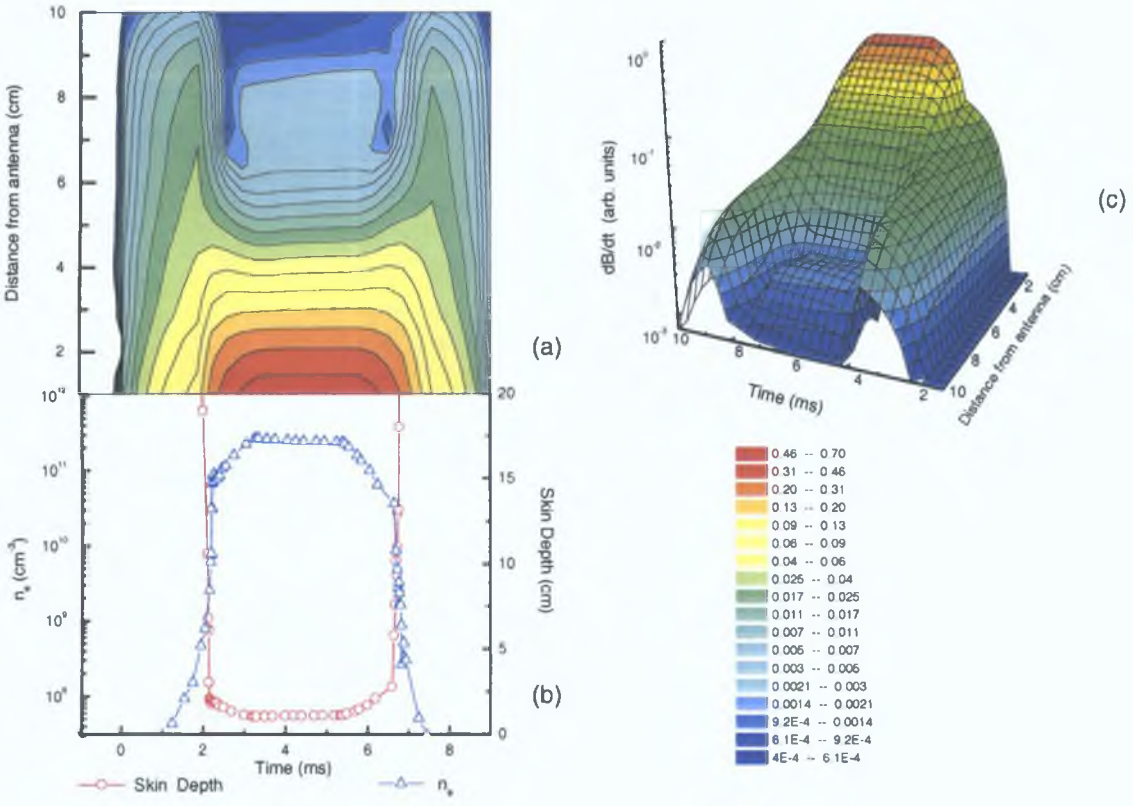

Figure 4.17: *(a) A three dimensional map (temporal and spatial evolution) of the magnetic field in the discharge, plotted on a logarithmic scale, for the 5 mTorr discharge matched in the H mode. (b) Shows the time evolution of the plasma density together with the corresponding calculated collisionless skin depth* $\delta = c/\omega_{pe}$.

The pulsed method has the advantage of covering the whole range of current and power during the transition so its dynamics can be investigated easily. As discussed in the Introduction, Kortshagen et al. [17] proposed that a stable H mode plasma can only be achieved when the skin effect becomes significant. In order to verify this hypothesis and their qualitative model for the dynamics of the

transition the Langmuir probe and the B-dot probe have been used to determine the time dependence of the electron density and the plasma skin depth A three dimensional map (time and space evolution) of the magnetic field in the discharge was obtained by measuring the time modulation of the amplitude of the B-dot signal during the pulse at different radial positions The results are plotted on a logarithmic scale in figure 4 17(a) for the 5 mTorr discharge matched in the H mode Figure 4 17(b) shows the time evolution of the plasma density together with the corresponding calculated collisionless skin depth $\delta = c/\omega_{pe}$, where ω_{pe} is the electron plasma frequency The graph shows that the electron density increases by two orders of magnitude during the transition and the skin depth decreases dramatically during that time It is clear in figure 4 17(a) that the electromagnetic field penetrates deeply into the plasma in the E mode, while it is confined within the skin depth as soon as a stable H mode is established, in good agreement with the previous discussion The behaviour of the field can be seen in greater detail in figure 4 19 where the radial profiles of B are plotted for different times during the 100 μs duration of the transition It is obvious here that the skin depth approaches the system size during the E to H transition allowing a stable H mode to be established

The dynamic of the transition can be described with the aid of the power balance diagram shown in figure 4 18 The stable operating points of the discharge is the set of intersection points of the P_{dis} (black curve) and the P_{abs} family of curves (coloured curves) where each colour represents the absorbed power at a particular antenna current as a function of electron density, with $i_1 < i_2 < i_3 < i_4 < i_5 < i_6$ In the pulsed discharge initially there is an E mode plasma

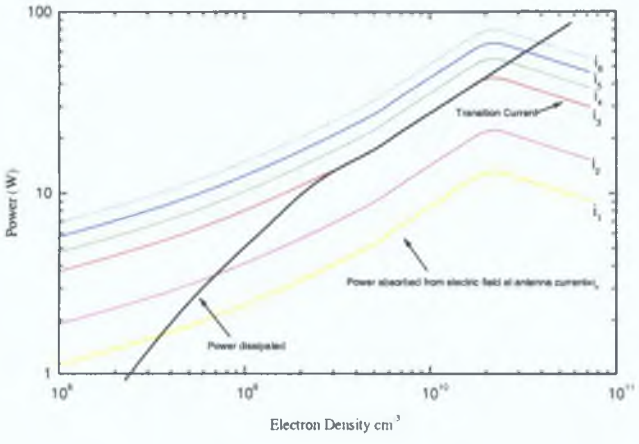

Figure 4.18: *P_{dis} (black curve) and the P_{abs} family of curves (coloured curves) where each colour represents the absorbed power at a particular antenna current as a function of electron density, where $i_1 < i_2 < i_3 < i_4 < i_5 < i_6$.*

where the induced azimuthal electric field produces negligible electron heating and ionisation. Ramping the antenna current, a value is reached (i_3) where the induced electric field that can produce significant ionisation. This critical value is the threshold current for the E to H transition and it can be seen from figure 4.18 that i_3 can in principle support a plasma which spans a range of densities. At the point where i_3 is reached the ionisation rate becomes suddenly higher than the loss rate which is still determined by the E mode ion density profile. The skin depth δ is still very large and the RF azimuthal electric field E_θ is hardly damped along the discharge radius. The transition proceeds as an avalanche (n_e increases dramatically). For a steady state to be reached, δ must be short enough to lower the spatially averaged inductive ionisation rate so that it precisely balances the

loss rate The transition will last until the condition

$$\frac{dP_{abs}}{dn_e} < \frac{dP_{dis}}{dn_e}, \tag{4 9}$$

is satisfied Described in this way, the transition is discontinuous and the plasma is out of equilibrium during the whole transition process since particle and power balance do not hold during this time

This lack of equilibrium can be seen experimentally as structure in the field which is apparent in figure 4 19 (particularly in the data between 2 14 and 2 20 ms) The spatial structure in B is reproducible and not due to common mode noise, but rather to an instability or movement within the discharge This distortion of the field during the transition may be a different phenomenon from the 'hump' in the magnetic field that can be seen in figure 4 17(a) during the H mode portion of the pulse (around $t = 4$ ms and $r = 7$) This 'hump' is a consequence of the anomalous skin effect which is fully discussed in chapter 3 Another experimental observation supporting the discontinuity of the E to H transition is the presence of noise on the ion and electron currents on the Langmuir probe I-V traces taken during that time

Further consideration of the results brings another interesting observation One can see from figures 4 4,4 14,4 15, and 4 17 that although the pulse of applied power is symmetric in time, the power absorbed, antenna current, light emission and magnetic field are not In particular, it appears that if the E to H transition occurs on the time scale of 100 μs which can be estimated from any of the previously mentioned graphs, the H to E transition is smoother and lasts longer This is particularly clear in figure 4 17(a) In fact, as can be seen in the magnetic

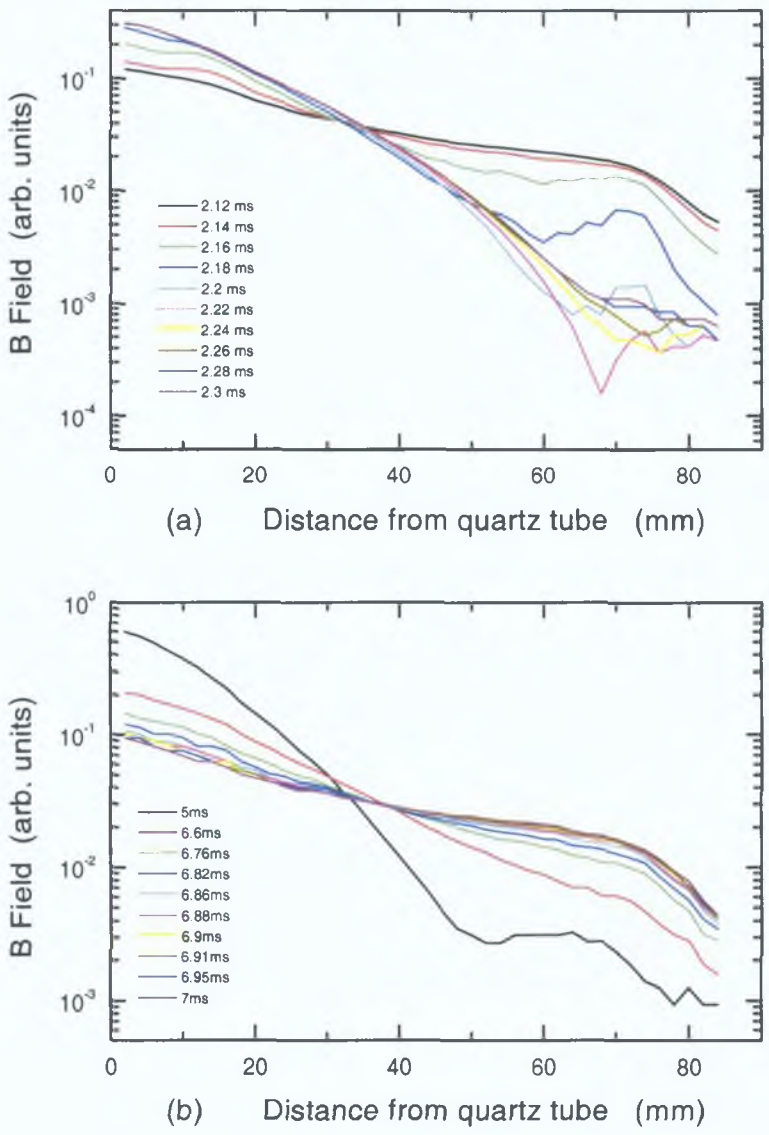

Figure 4.19: *Radial profiles of the magnetic field strength (B) plotted for different times during the 100 μs duration of the transition (a) E-H and (b) H-E transition.*

field measurements, the H to E transition is so smooth that its duration and location in time are difficult to estimate from just these data. Furthermore, the indications of non-equilibrium observed during the E to H transition are not present here, and both the B-dot and Langmuir probe data are smooth at any time during the H to E transition. This suggests that although the E to H transition is discontinuous, in agreement with the model of reference [17], the H to E transition in this pulsed discharge seems to satisfy power and particle balance at all times, or goes through a very small jump that is not detected here.

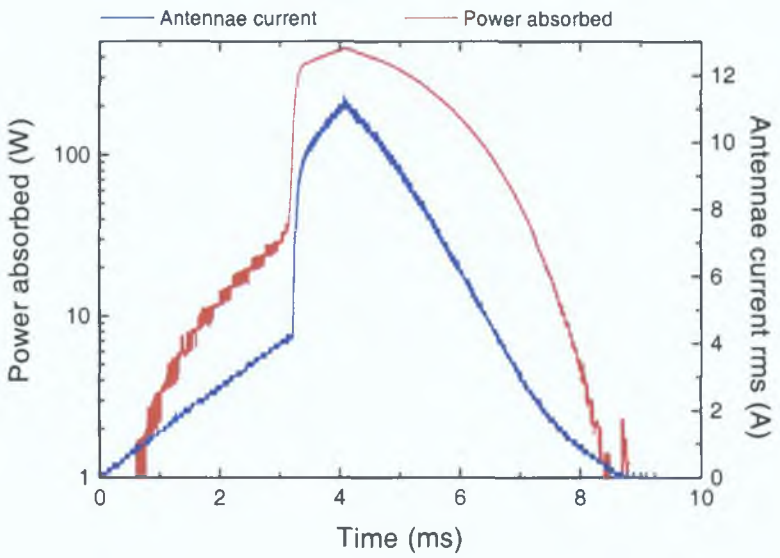

Figure 4.20: *The antenna current and absorbed power for a 150 mTorr discharge (H mode matching).*

This asymmetry becomes even more obvious at higher pressures. In figure 4.20, measurements of the antenna current and absorbed power for a 150 mTorr discharge (H mode matching) are presented, with figure 4.21 showing the corresponding evolution of the plasma density and light emission, and figure 4.22

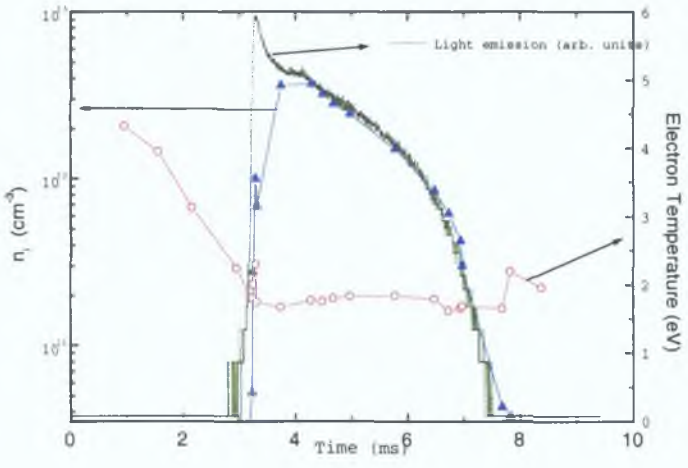

Figure 4.21: *Shows the time evolution of the plasma density (triangles), electron temperature (circles) and light emission (solid line) for a 150 mTorr discharge (H mode matching).*

giving the space and time evolution of the magnetic field inside the plasma. Here the asymmetry of the internal plasma parameter during the E to H and H to E transition is obvious. The E to H transition proceeds quickly (in 100 μs) and it is an extremely sharp transition since during this time the plasma density increases by almost 3 orders of magnitude (P_{abs} increases by one order). During the transition the plasma is strongly out of equilibrium and the electron temperature is higher than in the steady state. This can be seen in figure 4.21. The density evolves quite differently from the plasma emission during several hundreds of microseconds following the transition (the light emission intensity decreases although n_e is increasing). The initial burst of light is linked to the changes that occur both in the electron density profiles and in the shape of the EEDF as shown

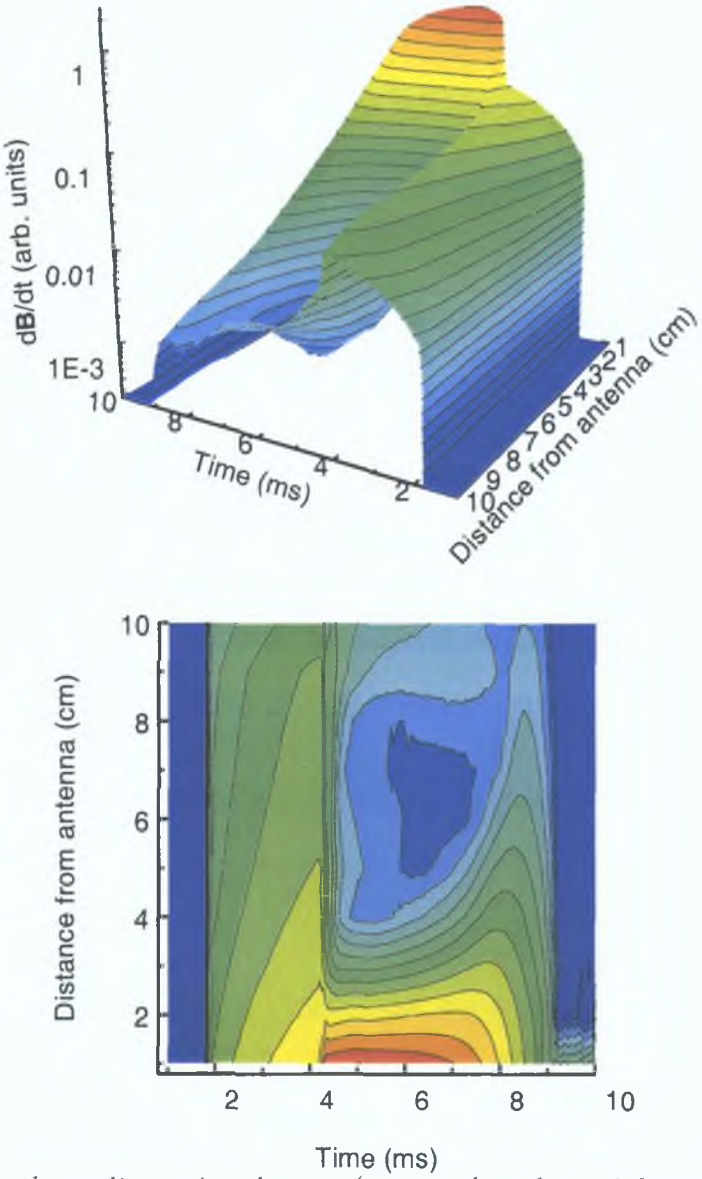

Figure 4.22: *A three dimensional map (temporal and spatial evolution) of the magnetic field in the discharge, plotted on a logarithmic scale, for the 150 mTorr discharge matched in the H mode.*

in section 4 2 2 The rapid changes in the plasma parameters are responsible for distortion of both the Langmuir probe traces and the B probe measurements during the E to H transition The distortion of the Langmuir probe trace calls into question the validity of the data taken during the transition, but a more detailed investigation of the transition yielded similar results This investigation involved the time consuming process of increasing the number of points acquired for a Langmuir probe trace by a factor of 10 to minimise the distortion

The reverse H to E transition is so smooth at this higher pressure that it becomes difficult to say if (and when) it occurs In fact a more detailed analysis of figure 4 22 shows that the skin depth never becomes much bigger than the plasma dimensions during the H to E transition because the density remains high even at low currents

Several ideas are relevant for an explanation of this asymmetry between the E to H and the H to E transitions Firstly, it is not surprising to find different time scales for these transitions, since the rise time of the density occurs as an 'avalanche' when the ionisation rate becomes bigger than the loss rate This phenomenon is not reversible because as the power (and coil current) decrease, the rate of decrease of n_e is diffusion limited so n_e cannot drop on a very short time-scale Furthermore, because of the strong hysteresis at high pressures, any expected density jump has to be much smaller in the H to E transition In addition is possible to imagine conditions for which the P_{abs} curve and the P_{dis} curve follow a co-linear path are for a range of n_e, allowing an almost continuous H to E transition, but a sharp discontinuous E to H transition to occur

A consideration of the diffusion process is helpful in determining whether the

continuity of the H to E transition in this system is linked to the pulsing of the discharge or not At high pressure, ambipolar diffusion is slower and there are two possibilities either the power modulation is slow enough so that the equality $P_{abs} = P_{dis}$ holds true during the downward ramp, and the diffusion does not affect the results In this case this experiment is the same as decreasing the power step by step with a small step If this is not the case, i e if the power absorbed decreases much faster than the electron density, ambipolar diffusion can lead to an apparent continuity in the H to E transition since the decrease of n_e is no longer proportional to the decrease of P_{abs} In that case, it would be expected that the electron temperature will drop during the ramping down, as is the case in an afterglow plasma However, these data show (see figure 4 21) that the light emission remains proportional to n_e and to P_{abs} during whole the ramping down time

The extent to which diffusion is important in this experiment can be also determined by considering the time scale for the decay of the plasma density in the ambipolar diffusion regime For 3 eV electrons at a few hundred mTorr, the characteristic diffusion time in this system is given by [34]

$$\tau = \frac{\Lambda^2}{D_a} \tag{4 10}$$

where Λ is the characteristic length of the fundamental diffusion mode (taken to be around 3 cm in the system) and D_a is the ambipolar diffusion coefficient Taking the value of D_a=63 cm^2 Torr s^{-1} from reference [75] for an afterglow plasma and correcting for the electron temperature of 3 eV, the characteristic diffusion time is found to be 180 μs at 150 mTorr, a number that is rather small

when compared to typical duration of the decreasing power ramp ($\approx$ 5 ms) This estimate suggests that ion diffusion is sufficiently fast in the system for the equality P_{abs}=P_{dis} to hold during the ramping down period The results therefore indicate that the H to E transition is not necessarily discontinuous in inductive discharges

Finally, it should be mentioned that the study of the H to E transition is somewhat complicated in this system by the presence of additional non-uniform but stable plasma states just above the maintenance current For well-defined values of the external parameters, the plasma around the antenna tube breaks up into several bright lobes or 'plasmoids' [76] The formation of these structures does not directly affect the measurements presented here and are the subject of a detailed experimental investigation which is presented in chapter 5

4.3 Concluding Remarks

In this chapter, the results of an experimental study of the E to H transition that occurs in inductively coupled discharges was presented The focus of attention has been on two different aspects of the transition, namely the hysteresis that is associated with this transition and the dynamics of the transition

In a detailed set of experiments in steady state E and H mode discharges, it has been shown that changes in the efficiency of plasma generation occur in this discharge furthermore the changes become more pronounced as pressure is increased The principal reasons for this are

- A change in the form of the EEDF from Druyvesten distributions (in the

E-mode) to Maxwellian distributions (in the H-mode) This change is found to occur at high pressure but not at low pressure

- Two-step ionisation is found to be an important plasma production process at higher pressures

- The small hysteresis loop at low pressure is caused by a non-linearity in P_{abs} resulting from changes in the efficiency of capacitive coupling between E-mode and H-mode

These results are relevant to the recent work of Turner and Lieberman [21] and allows the hysteresis phenomenon to be understood as resulting from a non-linearity in $P_{abs}(n_e)$ that leads to multiple solutions for the power balance of the discharge electrons

The effect of matching and the dynamics of the transition were investigated with an approach consisting of using a pulsed discharge The main results obtained from employing time-resolved diagnostics during the pulse are

- The characteristic time scales of the E to H transition has been described

- It was shown that the skin depth becomes smaller than the size of the chamber during the transition thus allowing a stable H mode to be established, as suggested by Kortshagen et al [17]

- Another interesting feature of the results is that although a discontinuous E to H transition was observed the reverse H to E transition appears to be smooth at high pressure

Chapter 5

Low Pressure Instabilities

5.1 Introduction

A key criterion for the utilisation of inductively coupled plasmas in microelectronics processing or material surface modification is that the plasma be both temporally and spatially uniform Temporal uniformity is readily achievable in rf inductive discharges by operating the discharge in a regime which yields a stable solution to the power balance equation [77] On the other hand spatial uniformity is more difficult to achieve since the electron or ion density profile in a discharge is determined by a number of factors which are difficult to control independently However, with the appropriate choice of chamber geometry, antenna design and operational parameters, spatial uniformity, to within acceptable tolerances, is achievable [2] In general cylindrical ICPs whether they be planer coil, or extended coil configurations, have a non-uniform density profile in the r and z directions but are generally assumed to have a uniform profile in the azimuthal direction However, such an assumption has frequently been shown

to be incorrect While recent reports in the literature of azimuthal stratification in ICPs are rare [31, 32, 33] there have been numerous informal reports of the phenomenon most of which seem to be qualitatively similar to the phenomenon reported by Lamont in 1969 [78] and by Wood in 1930 [79] in which he coined the term 'plasmoids' to describe bright lobes of regular spatial frequency which rotated like spokes around the discharge Notwithstanding the aesthetic qualities of discharges which exhibit such instabilities, these instabilities can pose some serious problems in processing systems These problems may be overcome with knowledge of the behaviour of the instabilities and a clear understanding of the mechanisms involved in the instabilities It was with this objective in mind that the following investigation was undertaken In section 5 2 a brief description of the instabilities in this system is given, in section 5 3 Langmuir probe measurements which are spatially resolved in the azimuthal direction are presented, in section 5 4 results of electrical diagnostics are presented with the aim of characterising the instabilities in power-pressure space In section 5 5 some possible mechanisms which may give rise to the phenomena are discussed

5.2 Description of the Instability

The experimental system is fully described in section 2 1 The argon discharge was driven at frequencies of 12 MHz and 13 56 MHz producing H mode plasmas of average density 10^{11} cm^{-3} and effective electron temperature $T_e \sim 1-2$ eV B-probe measurements presented in section 3 2 show that the typical maximum amplitude of the electric field in the discharge $E \geq 3$ Vcm^{-1}

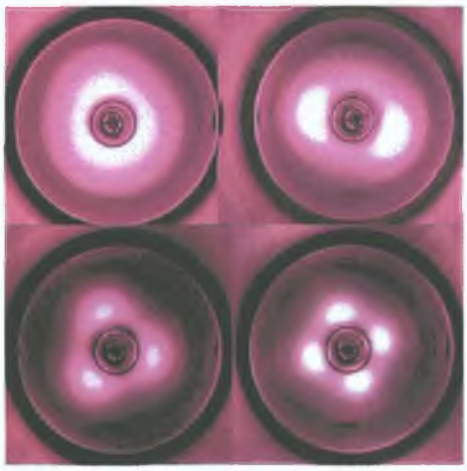

Figure 5.1: *Photographs of the discharge exhibiting instabilities of mode number 1,2,3 and 4 the photographs are taken at a pressure of 513 mTorr where all four modes can be observed by decreasing the rf current.*

At pressures from about 60 mTorr upwards the discharge exhibits instabilities of the kind shown in figure 5.1. The bright regions or 'lobes' can be stationary or they may rotate around the antenna at a rate of a few hertz. The rotation rate of the plasmoids around the antenna tube is dependent on the rf power and pressure . Figure 5.2 shows the rotation frequency of the 3 lobe structures a function of rf power for 3 pressures, at low power the plasmoids rotate in the anti-clockwise direction, as the power is increased the rotation rate slows down at first until it reaches zero and then it begins to rotate in the clockwise direction, reaching a maximum frequency of about 15 Hz at which point the number of lobes decreases by 1 and the rotation rate decreases. The addition of an external dc magnetic field in the z direction was found to increase the maximum rotation rate to about 60Hz. Experiments carried out to observe the effect of the direction of the coil winding on the rotation of the lobes show that the rotation of the lobes

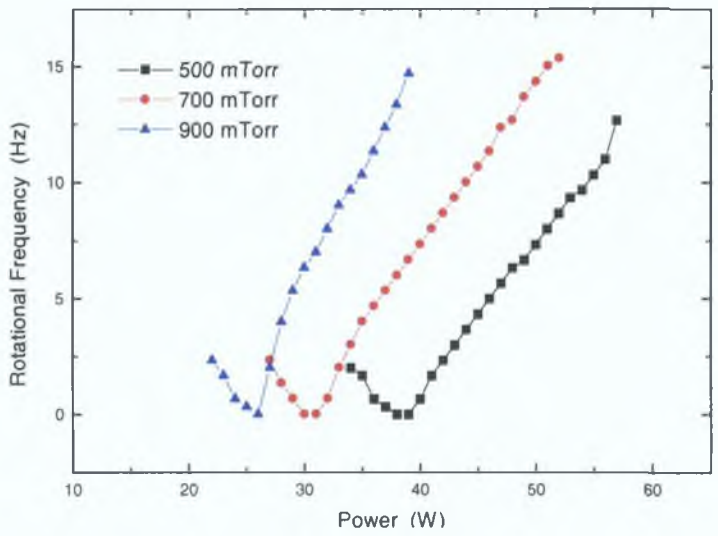

Figure 5.2: *The rotation rate of the structures as a function of power for three different pressures.*

is independent of the direction in which the coil is wound.

The number of lobes herein called the *mode number* again depends on the parameters of power, pressure and the matching conditions. However this dependence is not straightforward and it exhibits bi-stability and complex hysteresis cycles. Mode numbers of 2,3 and 4 are common in the pressure and power range investigated but at higher pressures (several Torr) mode numbers as high as 10 were observed.

5.3 Langmuir Probe Measurements

The lobes exhibit a repulsive tendency to Langmuir probes, which makes the acquisition of spatially resolved measurements extremely difficult, for this reason the Langmuir probe measurements are made by the method of boxcar averaging.

In order to acquire the data, the lobes are forced to rotate by means of an external magnetic field and as the lobes pass through the probe the light emission level triggers the acquisition system to take a point on the *I-V* curve

5.3.1 Experimental Method

The Langmuir probe which is fully described in section 2 1 is set to acquire data in boxcar averaging mode A photodiode detects light from the plasma as the lobes rotate, the photodiode signal triggers a pulse generator to provide a short TTL signal when the plasmoid is at the required position A schematic diagram of the experimental setup is shown in figure 5 3 The TTL signal triggers the Smartprobe to take one point on the *I-V* curve or one point on the EEDF An example of the photodiode signal and TTL trigger signal is shown in figure 5 3 (b) Each point is averaged 30 times and 200 points are taken per curve a typical Langmuir probe trace taken in boxcar mode is shown in figure 5 3 (d)

The azimuthal structure of the plasma was investigated by forcing the lobes through the probe as they rotated around the antenna, the rotation rate was controlled by the external dc magnetic field The photodiode detected the light at the probe that was used to trigger the Langmuir probe system in boxcar mode The data presented here were collected at 200 mTorr in an Argon discharge with 3 lobes present

5.3.2 Results 1. Plasma Parameters

Figure 5 4(a) shows the azimuthal density profile of the plasma, these data were

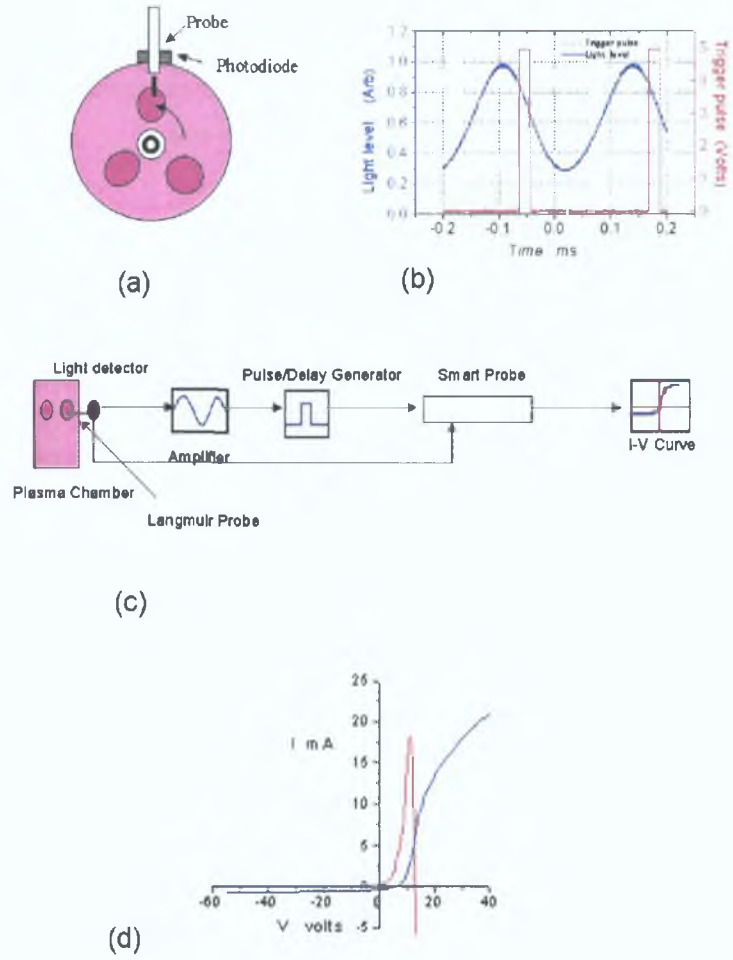

Figure 5.3: *Schematic diagram of experimental setup used to acquire spatially resolved Langmuir probe measurements. (a) Shows how the lobes are set to rotate through the probe. (b) The light output from the photodiode and the TTL trigger signal (c) Schematic of the experiment (d) Typical Langmuir probe trace taken by this method.*

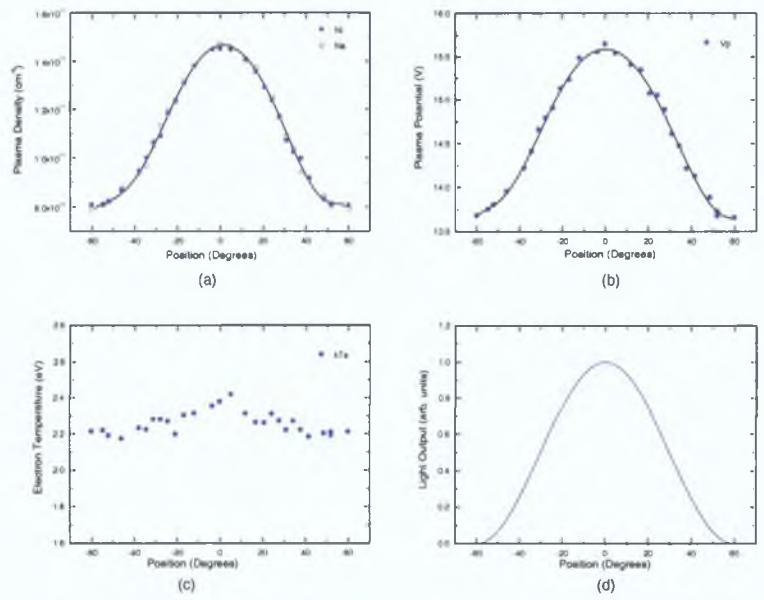

Figure 5.4: *Angular profile of the principal plasma parameters in a 200 mTorr argon discharge with 3 lobes present.*

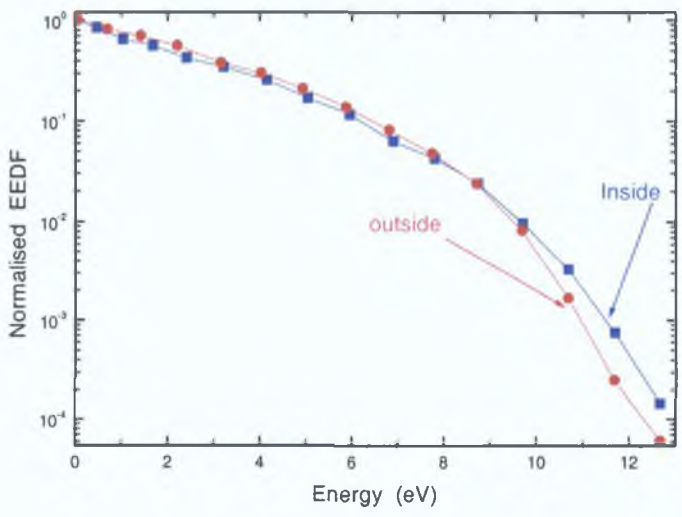

Figure 5.5: *Normalised EEDF taken in boxcar averaging mode*

taken in a H mode plasma at a pressure of 215 mTorr and at a power of 50 W there were three lobes clearly visible in the plasma at the time The profile of the plasma potential is shown in figure 5 4(b) and the electron temperature is shown in figure 5 4(c) The ratio of electron densities in the dark and bright regions is 53 Using the mean electron temperature of 2 25 eV and the difference in plasma potential of $\Delta V_p = 1\ 9$ V the Boltzmann factor gives a density ratio of 43 indicating reasonable consistency with electrostatic confinement of electrons While the electron temperature is almost constant across the lobe, EEDF measurements shown in figure 5 5 indicate that the high energy tail of the EEDF is somewhat enhanced inside the bright regions Magnetic field probe measurements indicated that the electric field is higher in the dark regions which is expected if the conduction current continuity condition is to be fulfilled since the conductivity is greater in the bright regions due to the higher electron density

5.4 Electrical Diagnostics

The rf current, voltage and the phase difference between them is measured by a *Scientific Systems*^{TM} current and voltage probe This probe is connected to the rf transmission line between the matching unit and the antenna The probe samples the current and voltage 10 times per second Initial observations of the antenna current showed that there is a sharp jump in the rf current as the instability appears or as the mode number of the instability changes from one mode to another This jump is qualitatively similar to the behaviour of the current during the E-H transition (see figure 4 20), but is generally much smaller In order to characterise the instabilities a convenient parameter to define is the transition

current $I_{n\to n\pm1}$ this is defined as the antenna current at which the mode number of the instability changes form n to $n \pm 1$.

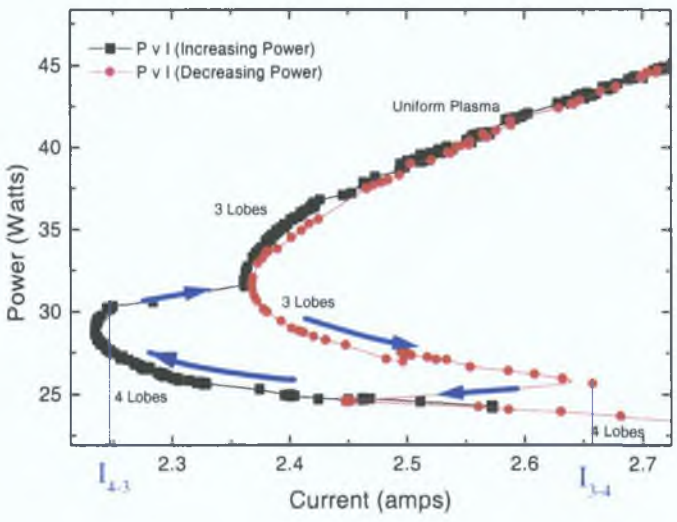

Figure 5.6: *Absorbed power as a function of antenna current the black curve is taken with increasing power and the red curve is taken with decreasing power.*

In order to determine the transition currents precisely, the discharge was pulsed with a long triangular ramp (≈ 20 s) during this ramp the current, voltage and power was recorded. A typical plot of power V current for a pulse is shown in figure 5.6 the transition points can be seen clearly seen as discontinuities in the curves. It is immediately obvious from the curve that the forward and reverse transitions do not take place at the same current or power for example in the figure shown $I_{3\to4} = 2.65$ Amps while $I_{4\to3} = 2.25$ Amps, also there is a range of currents for which two or more modes can exist. These curves are reproducible but the number of accessible modes depends on the matching conditions. Figure 5.7

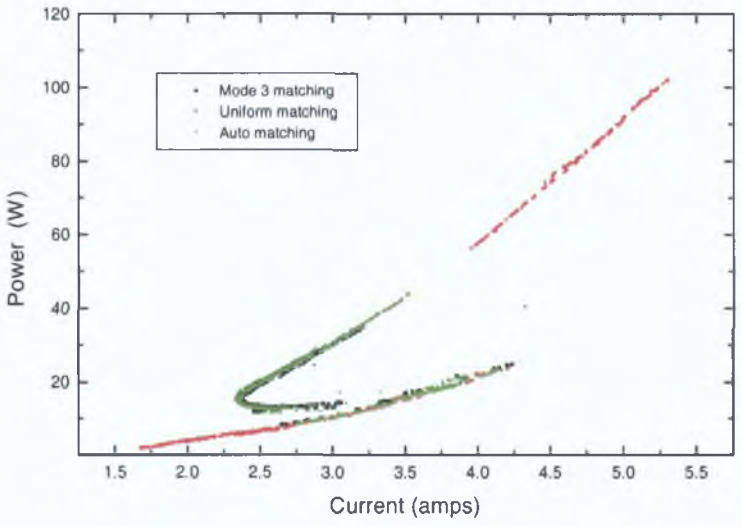

Figure 5.7: *Absorbed power as a function of antenna current for three different matching conditions.*

shows the curves corresponding to three different matching conditions, in this figure it can be seen that if the plasma is matched in a uniform H mode then the instability will not be established by reducing the coil current because the discharge changes to an E mode at a current which is higher than $I_{u\to 2}$. However if the plasma is matched in the highest possible mode number the full range of the instability can be seen during the pulse. Ideally the experiments to determine the transition currents should be done with the matching unit in the automatic setting but this proved difficult since in some cases it was impossible to perfectly match the plasma and in such cases the matching unit goes from one extreme setting to the other during the pulse. Therefore the plasma is matched in the highest possible mode number for the particular pressure under investigation.

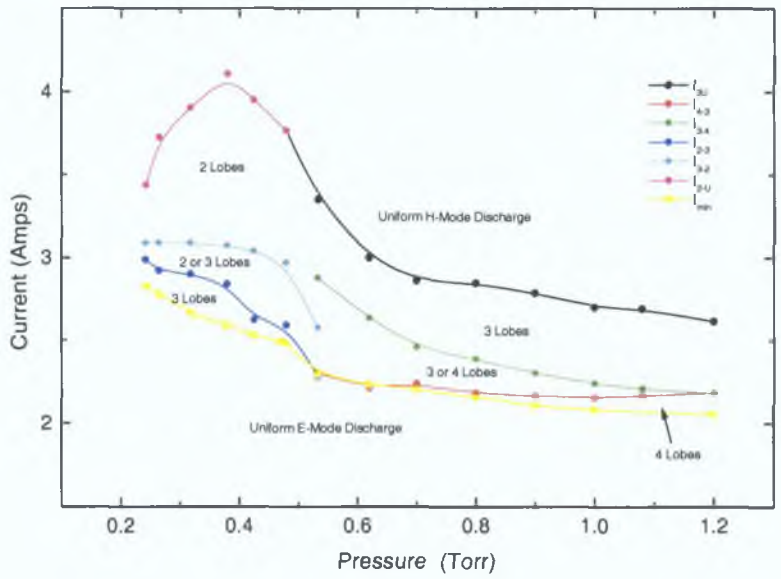

Figure 5.8: *Transition currents for various mode numbers as a function of pressure also indicated is the mode number observed in each region*

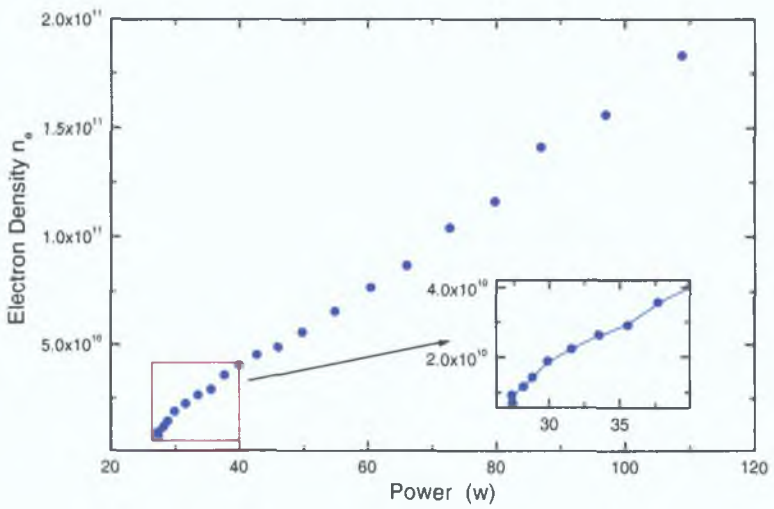

Figure 5.9: *Electron density as a function of absorbed power.*

Figure 5 8 shows the pressure dependence of the threshold currents for the instability these data were taken in a pure argon discharge at a frequency of 11 MHz At pressures below 500 mTorr modes 2 and 3 are the dominant modes and they are bi-stable with respect to each other and exhibit considerable hysteresis loops At above 500 mTorr modes 3 and 4 are the dominant modes they exhibit bi-stability along with a decreasing hysteresis loop up to 1150 mTorr The mode numbers and transition currents are weakly dependent on pressure With the system operating at 11 MHz the onset of the instability occurred at approximately 60 mTorr whereas at 13 56 MHz the onset occurred at 200 mTorr Tests at other operating frequencies showed that the minimum pressure for the onset of the instability and the dominant mode number are strongly dependent on frequency In figure 5 9 the power in the discharge is plotted against the plasma density It can be seen from the figure that the power in the relationship between the power and the density is different in the low power range (where the instability is present) than it is in the high power range (where there is no instability) In the low power range the density increases faster with power than in the high power range

Gas Composition

It was found that the addition of a small quantity of oxygen made the instability appear more readily (i e at lower pressures and over a larger range of power with more modes observed) As was already stated in section 4 2 2 adding oxygen has the effect of lowering the ionisation rate by quenching metastable atoms Figure 5 10 characterises the instabilities in the same manner as figure 5 8 In

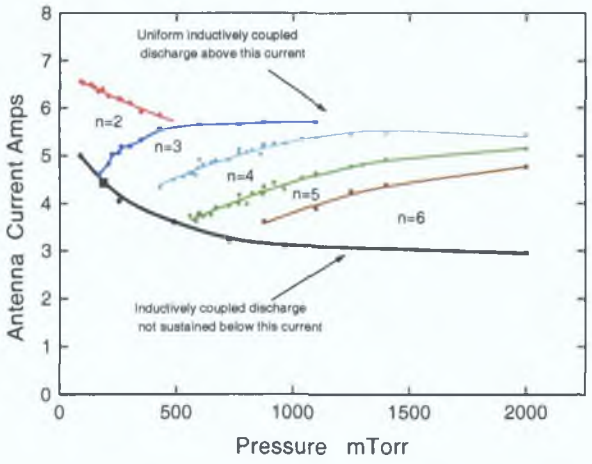

Figure 5.10: *Transition currents for various mode numbers as a function of pressure also indicated is the mode number observed in each region for a 98 % Ar 2 % O_2 discharge*

figure 5.10 the gas composition is $\approx$ 98% argon and 2% oxygen if the oxygen content is increased much more above this value the discharge can no longer be maintained in H-mode since at high pressure two-step ionisation is required to maintain an inductive discharge [77, 36].

5.5 Discussion

While no complete theory has been formulated to fully describe the instability one hypothesis that was proposed by Turner [80, 76] is that instability is the manifestation of Ponderomotive forces. Ponderomotive forces are secular (time averaged) terms that appear when a charged particle is immersed in an oscillating field with gradients in space. An electron responding to such an electric field

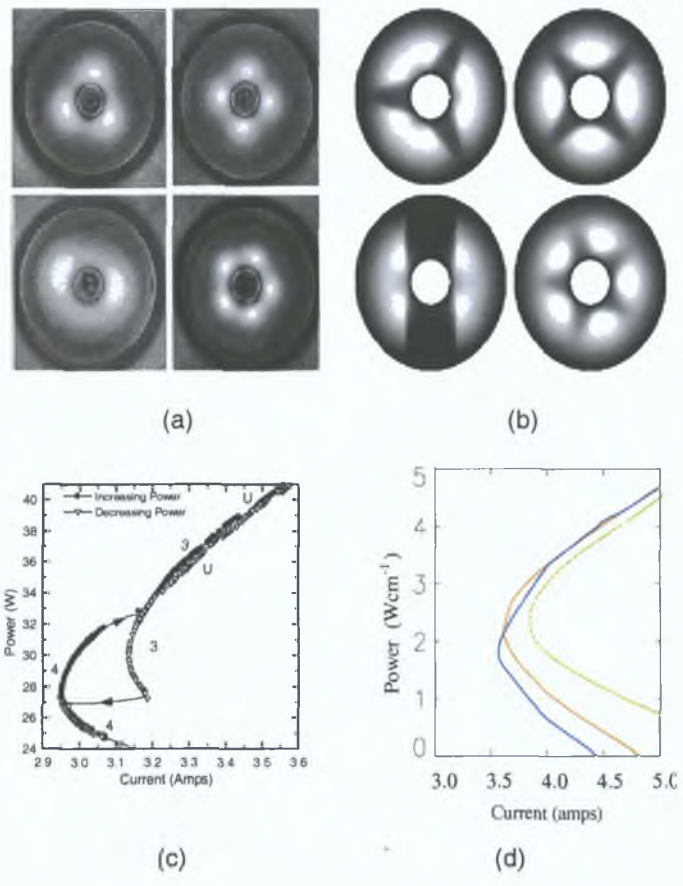

Figure 5.11: *(a) shows photographs of the discharge viewed along the axis of the coil, for modes n=2,3,4 and 5. (b) Shows model solutions corresponding to (a). (c) Shows an experimentally measured hysteresis cycle at a pressure of 1Torr where modes 3,4 and a uniform plasma are observed (d) shows a model calculation corresponding to figure (c) in this figure the blue curve is mode 3 the red curve is mode 4 and the green curve is the uniform discharge state which becomes stable where the curve is continuous.*

experiences an average force given in its simplest form by

$$F_p = -\frac{1}{4}\frac{e^2}{m_e\omega_{rf}^2}\nabla E^2, \tag{5 1}$$

where E is the electric field amplitude ω_{rf} is the frequency An instability can arise from a combination of equation 5 1 and a current continuity condition Typically in inductive discharges the field amplitude is constant along the field lines and $F_p = 0$ However if a density gradient exists parallel to E and conduction current is to be conserved then there must be gradients in E parallel to E, in this case $F_p \neq 0$ and furthermore F_p is directed away from regions of high field intensity and low plasma density so it leads to a depletion of density and possible instability If there is an initial small density perturbation in the azimuthal direction, the Ponderomotive force directs electrons towards the high-density region, which increases the density gradient, which in turn increases the force Calculations show that if ion transport is by ambipolar diffusion, the instability begins to grow when E exceeds a critical value E_c given by

$$E_c^2 = \frac{2m_e k_B T_e(\omega_{rf}^2 + \nu_e^2)}{e^2}, \tag{5 2}$$

where ν_e is the electron collision frequency This critical value is often exceeded during inductive discharge operation The hypothesis was tested and computer model simulations yielded promising results such as the example shown in figure 5 11 [80, 76] however there are problems with some of the fundamental assumptions made in the model, particularly equation 5 1 assumes that the amplitude of electron oscillation is small compared to the wave length of the disturbance in the field This assumption does not hold true in the system and without it a dispersive term is added to the ponderomotive force Furthermore investigations

reveal that mechanism assumed in this model is not the only one which can produce such results [73] There is also the possibility that structures are the result of an ionisation instability involving two step ionisation This may be possible on the basis that the rate for two step ionisation is sensitive to density so again if there is an initial small density perturbation in the azimuthal direction there would be increased ionisation in the high density region that could lead to an instability This is consistent with observations of more occurrences of the instability in $Ar \& O_2$ mixtures since oxygen leads to the de-excitation of metastable atoms which could lead to a more delicate balance between ionisation rates and destruction rates for metastable atoms In such a case, the instability is more likely to grow

Chapter 6

Conclusions

The preceding three chapters of this thesis have presented the results of an experimental investigation of a re-entrant cavity RF inductively coupled plasma operating at a frequency of 13.56 MHz, the operating power range was generally between 5 and 300 W and the operating pressure range was between 0.5 mTorr and 1 Torr . The principal diagnostics used were Langmuir probes, RF current and voltage probe and a specially constructed two dimensional $\dot{B}$ probe. In conclusion to this thesis this chapter contains a summary of the main results presented within and also suggestions for further work which could be carried out in order to enhance or improve our understanding of this type of plasma.

6.1 Magnetic Field ($\dot{B}$) Probe results

In chapter 2 the design, construction and analysis method for the two dimensional $\dot{B}$ probe was presented. The $\dot{B}$ probe has proved to be a very useful diagnostic tool for research into low-pressure ICPs and there is no doubt that it will provide

many more useful results in time In chapter 3, the electron electrodynamics have been investigated in an inductive discharge, with the discharge operating over a wide range of plasma parameters in the stochastic heating regime The rf electric field and current density distributions determined from B probe measurements indicate a strong anomalous skin effect, this is exemplified by

- Non-monotonic decay of the electromagnetic fields
- Phase reversal and bifurcation
- Negative power absorption regions

Most of those features are interpreted in terms of spatial dispersion of the conductivity due to the electron thermal motion at low pressure This non-negligible thermal motion leads to transit time collisionless heating as was demonstrated by comparing the total power absorbed in the experiment with an experimental measurement of the collisional power deduced from a cold plasma theory These results represents a substantial data base for simulation, and have demonstrated, in agreement with Godyak *et al* [63], the importance of stochastic heating in inductively coupled discharges They also demonstrate strong similarities (both qualitative and quantitative) between collisionless effects in a significantly different reactor geometry

Suggestions for further work

- The radial profiles of the amplitude and phase of the RF electric field are remarkable and certainly worthy of further investigation In [24] Kolobov and Economou present qualitatively similar profiles based on an analytical

treatment of a planar coil system, with a uniform density profile and a Maxwellian EEDF It may be instructive to apply the same analysis to the system described in this thesis with a non-uniform density profile and a non-Maxwellian EEDF which could be compared directly with the results presented in chapter 3

- Resonant effects that contribute to electron heating as proposed by Kaganovich et al [81] may be investigated further by means of Langmuir probe and B probe measurements made at different RF driving frequencies This would be possible with the addition of a good wide band RF power amplified and matching unit to the overall system

6.2 The E-H transition

In chapter 4, the results of an experimental study of the E to H transition that occurs in inductively coupled discharges was presented The focus of attention has been on two different aspects of the transition, namely the hysteresis that is associated with this transition and the dynamics of the transition

A detailed set of experiments was carried out, in steady state E and H mode discharges It has been shown that changes in the efficiency of plasma generation through multi-step ionisation and a change in the EEDF from Druyvesten to Maxwellian distributions take place in this discharge This result is relevant to the recent work of Turner and Lieberman [21] and allows the hysteresis phenomenon to be understood as resulting from a non linearity in $P_{abs}(n_e)$ that leads to multiple solutions for the power balance of the discharge electrons

The effect of matching and the dynamics of the transition were investigated with an approach consisting of using a pulsed discharge By using time-resolved diagnostics, the characteristic time scales of the E to H transition has been described, and shown that the skin depth enters the system during the transition allowing a stable H mode to be established, as suggested by Kortshagen et al [17] Another interesting feature of the results is that although discontinuous E to H transition was observed, the reverse H to E transition appears to be smooth at high pressure

Suggestions for further work

- While the thesis presents strong evidence that two step ionisation plays an important role in the overall nature of the E-H transition it would be instructive to strengthen this evidence by direct measurement of metastable atom densities

6.3 Instabilities

In chapter 5 the results of an investigation of discharge instabilities were presented The phenomenon was described in detail and spatially resolved measurements of the plasma parameters were made which show the structures to be regions of higher plasma density The electron temperature was found to vary only slightly, being higher in the bright regions The rotation of the structure was found to be independent of the direction in which the coil is wound The electrical characteristics of the discharge were also measured with a view to comparing the

results with a model The results found that while there was substantial agreement with the proposed model, this model was not the only one which could describe the underlying mechanism causing the instability It was found that gas composition plays an important role in the behaviour of the instabilities In particular the addition of small amounts of oxygen to the argon has a dramatic effect on the parameter space in which the instability is observed

Suggestions for further work

- In order to advance our understanding of the phenomenon it would be worthwhile to develop a computer model based on the hypothesis it is an ionisation instability

- Since the gas composition plays an important role in the behaviour of the instabilities, it would be intrusive to determined experimentally the exact composition of the gas and the ion species mix in the discharge

Bibliography

[1] H U Eckert Proceedings of the second annual conference on plasma chemestry and technology Lancaster Pa, 1986

[2] J Hopwood *Plasma Sources Sci Technol*, 1(2) 109–116, 1992

[3] J H Keller *Plasma Sources Sci Technol*, 5 166–172, 1996

[4] Y Wu and M A Lieberman *Plasma Sources Sci Technol*, 9(2) 210–218, 2000

[5] M A Liberman and A J Lichtenberg *Principles of Plasma Discharges and Material Processing* Wiley, New York, 1994

[6] R B Piejak V A Godyak and B M Alexandrovich *J Appl Phys* , 78 5296, 1995

[7] P L G Ventzek R J Hoekstra and M J Kushner *J Vac Sci Tehhnol B*, 12(1) 461, 1994

[8] S Rauf and N J Kushner *Plasma Sources Sci Technol*, 6 518, 1997

[9] V A Godyak R B Piejak and B M Alexandrovich *Phys Rev Lett* , 80 3264, 1998

[10] V Vahedi M A Lieberman G DiPeso and T D Rognlien *J Appl Phys*, 78 1446, 1995

[11] J A Stittsworth and A E Wendt *Plasma Sources Science and Technology*, 5(3) 429–435, 1996

[12] R A Stewart P Vitello D B Graves E F Jaeger and L A Berry *Plasma Sources Sci Technol*, 4(1) 36–46, 1995

[13] R B Piejak V A Godyak B M Alexandrovich *Plasma Sources Sci Technol*, 1 179, 1992

[14] M A Lieberman and V A Godyak Technical Report UCB/ERL M97/65, UCB, 1997

[15] D Boilson PhD thesis, Dublin City University, 2000

[16] I G Brown *The physics and tehnology of ion sources* Wiley, New York, 1989

[17] U Kortshagen N D Gibson and J E Lawler *J phys D applphys*, 29 1224–36, 1998

[18] H Ohkubo K Suzuki, K Nakamura and H Sugai *Plasma Sources Sci Technol*, 7 13–20, 1998

[19] I M El-Fayoumi and I R Jones *Plasma Sources Sci Technol*, 7 179–185, 1998

[20] I M El-Fayoumi and I R Jones *Plasma Sources Sci Technol*, 6 201–211, 1997

[21] M M Turner and M A Lieberman *Plasma Sources Sci Technol*, 8 313, 1999

[22] M M Turner *Phys Rev Lett*, 71 1844, 1993

[23] I D Kaganovich V I Kolobov and L D Tsendin *Appl Phys Lett*, 69 3818, 1996

[24] V I Kolobov and D J Economou *Plasma Sources Sci Technol*, 6 1, 1997

[25] I D Kaganovich *Phys Rev Lett*, 82 327, 1999

[26] N S Yoon S S Kim C S Chang and D I Choi *Phys Rev E*, 54 757, 1996

[27] M M Turner *Plasma Sources Sci Technol*, 5 159, 1996

[28] V A Godyak and R B Piejak *J Appl Phys*, 82 5944, 1997

[29] S Rauf and N J Kushner *J Appl Phys*, 81 5966, 1997

[30] R Piejak V Godyak and B Alexandrovich *J Appl Phys*, 81 3416, 1997

[31] J A Sittsworth and A E Wendt *IEEE Trans Plasma Sci*, 24 125, 1999

[32] D J Economou R S Wise and A A Kubota *IEEE Trans Plasma Sci*, 27 60, 1999

[33] M Tuszewski *J Appl Phys*, 79 8967, 1996

[34] F F Chen *Introduction to plasma physics* Plenum Press, New York, 1974

[35] W B Kunkel *Plasma physics in theory and application* McGraw-Hill, New York, 1966

[36] M Tadokoro H Hirata N Nakano Z Lj Petrovic T Makabe *Phys Rev E*, 58(6) 7823, 1998

[37] B Chapman *Glow Discharge Processes* Wiley, New York, 1980

[38] D Rapp and P Englander-Golden *J Chem Phys*, 43 1464, 1965

[39] K Tachibana *Phys Rev A*, 34 1007, 1986

[40] Bird Electronics Corporation Catalog gc-92, 1992

[41] I H Hutchinson *Principles of Plasma Diagnostics* Cambridge University Press, 1987

[42] J G Laframbois Technical Report 100, UTIAS, 1966

[43] M B Hopkins and W G Graham *Rev Sci Instrum* , 57(9) 2210, 1986

[44] V A Godyak and R B Piejak *J Phys IV France*, 8 241, 1998

[45] R B Piejak Private Communication, 1999

[46] M M Turner *Phys Rev Lett*, 71 1844, 1993

[47] A B Pippard *Physica*, 15 45, 1949

[48] G G Lister Y M Li and V A Godyak *J Appl Phys* , 79 8993, 1996

[49] M A Lieberman and V A Godyak *j-TPS*, 26 955, 1998

[50] C M Deegan PhD thesis, DCU, Dublin, 1999

[51] V A Godyak R B Piejak B M Alexandrovich *Plasma Sources Sci Technol*, 3 169, 1994

[52] H A Blevin J A Reynolds and P C Thonemann *Phys Fluids*, 13 1259, 1970

[53] R G Storer *Phys Fluids*, 16 949, 1973

[54] V I Kolobov D P Lymberopoulos and D J Economou *Phys Rev E*, 55 3408, 1997

[55] R H Cohen and T D Rognlien *Plasma Sources Sci Techno*, 5 442, 1996

[56] S Ichimaru *Basic Principles of Plasma Physics A Statistical Approach*, volume Vol 41 Academic, Reading, MA, 1973)

[57] E S Weibel *Phys Fluids*, 10 741, 1967

[58] R A Demirkhanov I Y Kadysh and Y S Khodyrev *Sov Phys JETP*, 19 791, 1964

[59] B Joye and H Schneider *Helvetica Physica Acta*, 51 804, 1978

[60] D Boilson N Curran P McNeely M B Hopkins and D Vender E s c a m p i g page 358, Dublin, 1998

[61] H U Eckert *J Appl Phys* , 43 2707, 1972

[62] V A Godyak St Petersburg, 1997 Plenum Press

[63] V A Godyak and V I Kolobov *Phys Rev Lett* , 79 4589, 1997

[64] V A Godyak *in electron kinetics and electroynamicscharacteristic of ICP in stochastic heating regim* Plenum Press, New York, 1998

[65] V I Kolobov *The anomalous skin effect in bounded systems* Plenum Press, New York, 1998

[66] M Hayashi Technical Report IPPJ-AM-19, 1981

[67] I R Jones I M El-Fayoumi and M M Turner *J Phys D Appl Phys* , 31 308, 1998

[68] M A Lieberman and R W Boswell *J Physique IV* , 8 145, 1998

[69] A R Ellingboe and R W Boswell *Phys Plasmas*, 3 2797, 1996

[70] N Sadeghi J P Booth, G Cunge and R W Boswell *J Appl Phys* , 82 552, 1997

[71] C Charles H B Smith and R W Boswell *J Appl Phys* , 82 561, 1997

[72] J P Goss G Cunge B Crowley M M Turner and D Vender Escampig page 196, Dublin, 1998

[73] M M Turner Private Communication, 2000

[74] L G Piper J E Valazoc and D W Setser *J Chem Phys*, 59 3323, 1973

[75] S Brown *Basic Data in Plasma Physics* AIP, New York, 1994

[76] B Crowley G Cunge M M Turner and D Vender Escampig page 196, Dublin, 1998

[77] G Cunge B Crowley D Vender and M M Turner *Plasma Sources Sci Technol* , 8(4) 999–1199, 1999

[78] L T Lamont and J Deleone *J Vac Sci Technol*, 7(1) 155, 1969

[79] R W Wood *Phys Rev*, 35 637, 1930

[80] M M Turner B Crowley G Cunge and D Vender Unpublished, 1999

[81] I D Kaganovich V I Kolobov and L D Tsendin *Appl Phys Lett* , 69 3818, 1996